Dottorato in Fisica e Chimica
Dipartimento di Scienze Fisiche e Chimiche-Emilio Segrè
Settore Scientifico Disciplinare FIS/01

Influence of ionizing radiations and thermal treatments on 4H-SiC defectivity

LA DOTTORESSA
FRANCESCA MIGLIORE

IL COORDINATORE
PROF. MARCO CANNAS

IL TUTOR
PROF. SIMONPIETRO AGNELLO

CO-TUTOR
DR. DANIELE VECCHIO

CICLO XXXVI
ANNO CONSEGUIMENTO TITOLO 2024

Contents

Abstract

The work presented in this thesis is funded by STMicroelectronics, a leader company in the production of semiconductor devices, and is focused on 4H-SiC, a polytype of silicon carbide (a wide bandgap semiconductor) with exceptional properties that make it suitable for the realization of high-power and high-temperature devices and for applications in harsh-environments. Among these properties the most relevant are the indirect bandgap value of 3.27 eV, the high breakdown electric field strength, the thermal conductivity, the chemical inertness, the mechanical strength, the saturation drift velocity and the radiation hardness.

The development of SiC and its utilization as a semiconductor in devices is relatively recent and mainly due to the work of several companies. For these reasons, most of the studies and characterization conducted on SiC have been performed especially using electrical characterization techniques. These ones are known to be invasive or "destructive" because they require fixed metallic contacts. As a consequence, electrical techniques cannot be used in the production line to monitor the quality and the properties of the SiC devices during their growth.

In this thesis, substrates and epitaxial layers of 4H-SiC have been experimentally studied with optical techniques (micro-Raman, steady-state and time resolved photoluminescence, steady-state absorption) to investigate the materials properties. In particular, optical techniques are non-destructive and require minimal or zero sample preparation and for this reason they can be used to check the interested properties, such as the polytype, the doping, the presence of defects, at each step of the growth.

Wafers produced by different companies were studied together with the epitaxial layer of 4H-SiC grown on them by STMicroelectronics. The used techniques enabled to distinguish among the different productions and to highlight the different defect levels by time-resolved photoluminescence, allowing to get important information on the quality of the material before the realization of a complete device.

In view of applications of devices of SiC in harsh environments the effects of electron and X-ray irradiations on 4H-SiC epitaxial layers as well as the effects of the exposure to high temperature on 4H-SiC substrates have been explored. Literature is rich in studies of different ionizing radiation and thermal treatments on several kind of devices made of 4H-SiC (by electrical measurements) but few studies have been carried out on the pristine material. This implies that some effects could be related to the

device production processes and not directly to the materials features. The choice to use optical characterization techniques enabled to deepen this aspect directly on the material without the need to include any device fabrications.

Overall, the work carried out has demonstrated the potentialities of the spectroscopic techniques in highlighting basic features of the SiC and the usefulness of probing the dynamic of the excited states in connection to intrinsic features like the doping and the defectiveness. Furthermore, the potentialities of the used methodologies for a deeper understanding of material modifications or imperfections are perspectively of interest both for basic research and for applications of the SiC.

The thesis is divided in seven chapter, as follows:

- Chapter 1 contains an introduction about Silicon Carbide, focusing on the polytype 4H-SiC. In particular, the structure, the properties that make SiC suitable for high-power and high-temperature devices, the synthesis of both substrates and epitaxial layers, the main extended and point defects are illustrated. Furthermore, the end of the chapter is dedicated to excitons in solids because of the important role of the exciton recombination process in the study carried out.

- Chapter 2 regards the theoretical background of the main characterization techniques used in this thesis, in particular micro-Raman and time-resolved photoluminescence spectroscopy.

- Chapter 3 collects the information about the wafers (substrates and epitaxial layer) and about the process to which they have been subjected, in particular electron and x-rays irradiations and exposure to high temperature. Furthermore, the different set-ups used for the experiments and for the measurements are also described.

- Chapter 4 reports the basic characterization by non-invasive techniques of both substrates and epitaxial layers of 4H-SiC, giving the hints useful for the physical study of the material.

- Chapter 5 is focused on the effects of ionizing radiation, in particular electrons and x-rays, on epitaxial layers of 4H-SiC.

- Chapter 6 reports the study of the effects of thermal treatments in inert atmosphere on substrates of 4H-SiC.

- Chapter 7 contains the main conclusions and some considerations about the thesis work and the perspectives of the research.

Chapter 1

Silicon Carbide

In this chapter an overview of Silicon Carbide (SiC) is given with particular attention to the polytype 4H-SiC. In particular, the physical properties, the synthesis methods of bulk and epitaxial layer, the major defects and application are discussed. Furthermore, a brief part of this chapter is dedicated to excitons in solids. The most relevant physical properties of SiC, as well as that of Si for comparison, are summarized in table 1.1.

1.1 Physical Properties

1.1.1 SiC Crystal Structure

SiC is made up by Silicon (Si) and Carbon (C) in a 1:1 ratio. Both Si and C atoms are tetravalent elements and have four valence electrons in their outermost shells so Si and C atoms are tetrahedrally bonded with covalent bonds (bond energy 4.6 eV) by sharing electron pairs in sp^3-hybrid orbitals to form SiC crystals [1]. Each C atom has exactly four Si atom neighbors, and vice versa, as shown in fig.1.1a. As depicted in fig.1.1a SiC can be considered a layered material, where a single layer is actually a bilayer composed by a chain of tetrahedra with in the center Si atoms and the upper chain of tetrahedra with in the center C atoms. For this reason SiC surface can end with two different faces, Carbon or Silicon face, depending on the last layer [2]. Several aspects as the doping of the material, the growth of epitaxial layers, the formation of defects depend on the SiC face. SiC is actually one of the most polymorphic semiconductors since it has currently more than 250 known polytypes determined by the stacking sequence of Si-C bilayers along c-axes or [0001] axes, as shown in fig.1.1a, each with specific electrical properties. In fig.1.1b, the structure of the three most studied polytypes of SiC, 3C, 4H, 6H, are shown. 3C-SiC is made of three bilayers (ABC stacking) in a cubic lattice, the highest symmetry shape lattice, so 3C-SiC structure is the most difficult to achieve during the growth. On the other hand, 6H-SiC and 4H-SiC are made respectively of six bilayers (ABCACB) and four bilayers (ABCB) both in a hexagonal lattice and due to their lower symmetry are easier to manufacture. A, B and C indicate
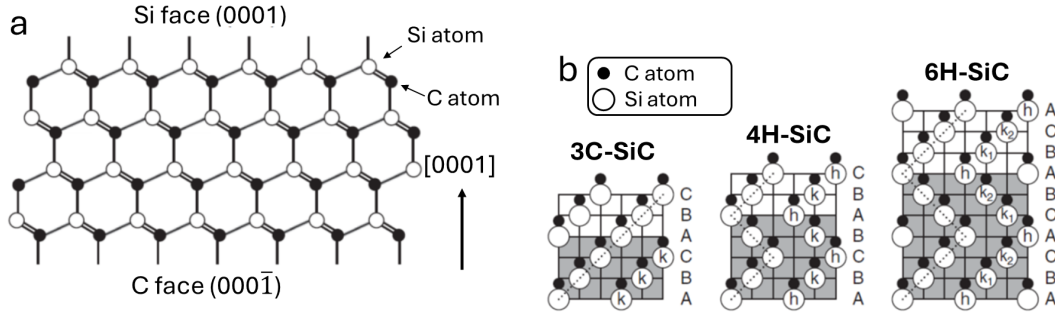
Figure 1.1: *a) Scheme of hexagonal SiC lattice [1]. b) Structure of different SiC polytypes, adapted from [1].*

the potentially occupied sites in a hexagonal close-packed structure. Due to the various stacking sequence of Si-C bilayers, multiple lattice sites characterized by difference of neighboring structures exist within SiC. Sites surrounded by a hexagonal structure are named "hexagonal sites" (indicated by "h" in fig.1.1b) while those surrounded by cubic structure are labeled as "cubic sites" (indicated by "k_n" in fig.1.1b). 3C-SiC contains exclusively cubic sites, 6H-SiC has one hexagonal site and two non-equivalent cubic sites and in 4H-SiC there are the same number of cubic and equivalent hexagonal sites. The presence of different sites give rise to different phenomena known as "site effect" as variation of the crystal field that influences the energy levels of dopants, impurities, and point defects.

1.1.2 Electronic and Optical Properties

All SiC polytypes have similar Si-C bonds so mechanical properties are very similar among the different polytypes [3, 4]. Nonetheless, the different periodic potentials in the SiC polytypes induces very different electronic band structures that influence the electronic and optical properties. This implies that for devices production is fundamental to grow only the desired SiC polytype.

Band Structure

The electronic band structures of 3C-SiC, 4H-SiC and 6H-SiC calculated by density functional theory are reported in fig.1.2 (absolute values of the bandgap are underestimated due to a limitation of the theoretical calculation). These results are confirmed by several studies [4, 5, 6]. In all the SiC polytypes the bandgap has an indirect structure, the maximum of the valence band is at the Γ point of the Brillouin zone and usually the minima are located at the boundary of the Brillouin zone. As shown in fig.1.2, the valence band structure of SiC polytypes is similar due to the Si-C covalent bonds that are common to all polytypes. The only difference is the splitting of the top of valence band due to crystal symmetry, crystal field and spin–orbit interaction. In particular, in 3C-SiC the top of the valence band is doubly degenerate and the next
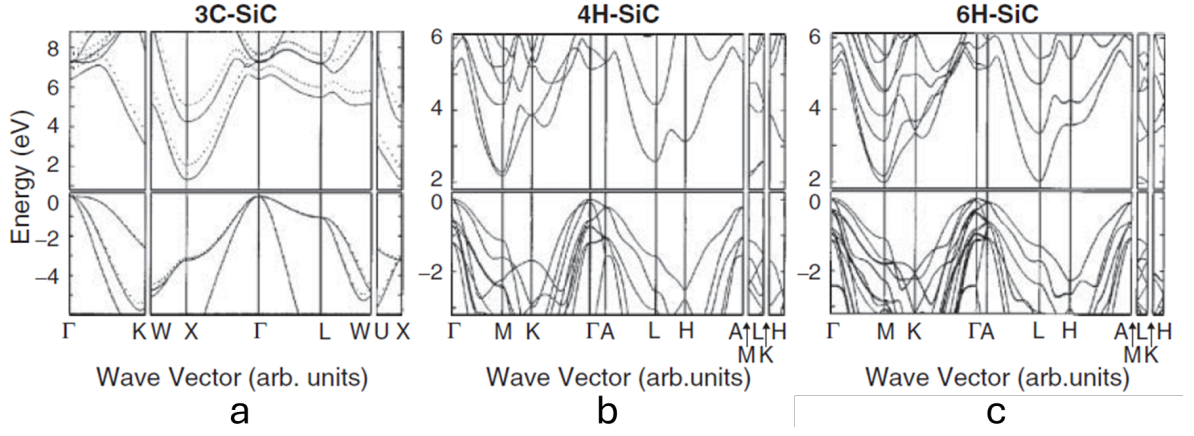
Figure 1.2: *Electronic band structures of 3C-SiC (a), 4H-SiC (b) and 6H-SiC (c) [7].*
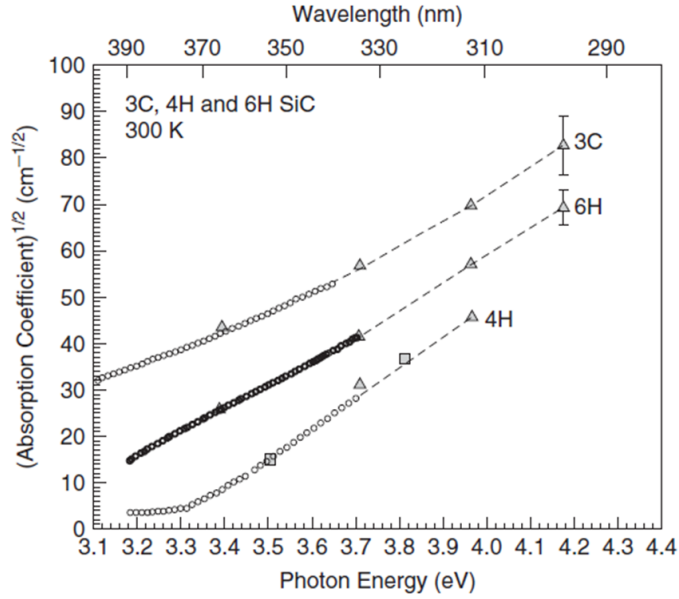
Figure 1.3: *Optical absorption coefficients as a function of photon energy for 3C, 4H and 6H-SiC polytypes[1].*

valence band is 10 meV shifted [1]. Instead, the magnitudes of the spin–orbit splitting and crystal-field splitting for 4H-SiC are respectively 6.8 meV and 60 meV [1]. The polytype 4H-SiC is the second one with the highest bandgap value (3.27 eV) after the polytype 2H (3.3 eV). Wide band-gap value implies low intrinsic concentration and high radiation hardness that are very important aspects for electronic devices.

Because of the indirect bandgap nature of SiC polytypes, the absorption coefficient increases slowly even when the photon energy is higher than the bandgap as shown in fig.1.3 for the major SiC polytypes. Absorption coefficient, α_o, is related to the the penetration depth, pt, as $1/\alpha_o = pt$, and is fundamental to keep in mind this value for any optical characterization techniques. For example, at room temperature the penetration depth in all SiC polytype at 325 nm is ≈ 7 μm and at 266 nm is ≈ 0.6 μm [1, 8].

Another important consequence of the indirect bandgap structure of SiC is that

Figure 1.4: *Scheme of typical recombination processes of carriers in SiC.*

phonons are intensively involved in carrier recombination processes, furthermore the binding energy of the free excitons in SiC is $20 - 30$ meV so they can exist even at room temperature [9, 10] (this aspect will be discuss more in details in section 1.5). Hence, in a high quality and purity SiC crystal it is possible to observe only band-to-band or free exciton pe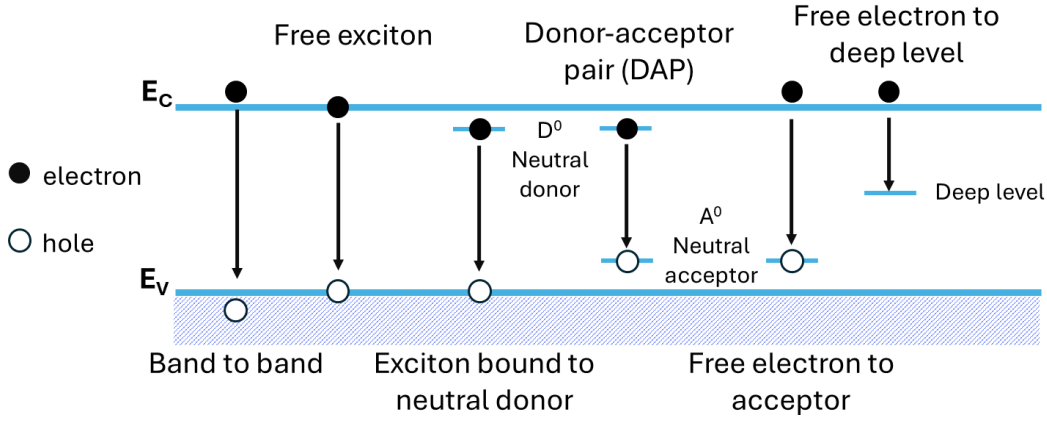aks. However, in a real crystal extended defects, point defects and impurities are present and can occur at different sites leading to several different energy levels within the bandgap and so to different recombination paths (radiative and non-radiative, illustrated in fig.1.4) that compete with each other [11, 10]. It is worth to note that when the wavefunction of an electron that is bound to a donor can interact with that of a hole that is bound to an acceptor, then donor–acceptor pair (DAP) recombination occurs [9]. An example of a typical PL spectrum measured at 2K for high-purity 4H-SiC epitaxial layer is reported in fig.1.5a. The I series originate from the recombination of free excitons, the P and Q series are related to the recombination of bound exciton with neutral nitrogen donors at not-equivalents lattice site (site effect). In fig.1.5b, the PL spectra of high-purity 4H-SiC epitaxial layer at different temperatures are reported. At room temperature the free exciton band dominates.

Mobility

Similar to other semiconductors, the mobility of SiC, μ, is limited by scattering processes with impurities (ionized and neutral) and phonons (acoustic, polar optical, non-polar optical, intervalley) and can be expressed by the Matthiessen's rule $\frac{1}{\mu} \approx \sum_i \frac{1}{\mu_i}$, where μ_i represents the mobility associated with the different scattering processes [13]. In lightly-doped n-type SiC, the electron mobility is predominantly influenced by acoustic phonon scattering in the temperature range 70–200 K and by intervalley scattering at temperatures higher than 300 K, as shown in fig.1.6a, which is similar to the behaviour of Si. In the case of heavily-doped n-type SiC, the primary scattering process is the one with neutral impurities at low temperature and intervalley scattering at high temperature as shown in fig.1.6b. It is worth to underline that the electron mobility
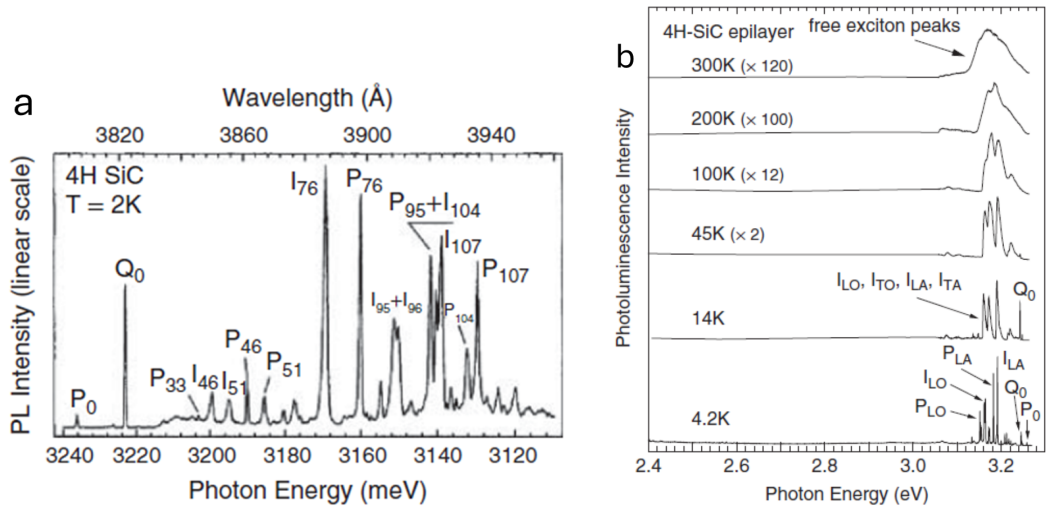
Figure 1.5: *a) Typical PL spectrum of high-purity 4H-SiC acquired at 2K [12]. b) PL spectra of high-purity 4H-SiC epitaxial layer at different temperatures in the range 4.2 − 300K [12].*

is also affected by the symmetry of the polytype. In particular, hexagonal and rhombohedral SiC exhibit strong anisotropy in electron mobility. For example, in 6H-SiC the electron mobility along the c-axis (about 100 $cm^2V^{-1}s^{-1}$ at room temperature) is only 20–25% of that perpendicular to the c-axis. In 4H-SiC the mobility anisotropy is relatively small, in fact, the electron mobility at room temperature along the c-axis is approximately 1200 $cm^2V^{-1}s^{-1}$ that is 20% higher than in the direction perpendicular to the c-axis [14]. It's not surprising that the electron mobility in 3C-SiC is isotropic due to its cubic symmetry; the electron mobility values reaches 750-1000 $cm^2V^{-1}s^{-1}$ in lightly doped and high-quality material.

Breakdown Electric Field Strength

A semiconductor junction breaks down when the electric field strength reaches a critical value characteristic of the material. This value is called the critical electric field strength or breakdown electric field strength (E_B). This value can be calculated taking into account the impact ionization coefficients or it can be obtained experimentally from the breakdown characteristics of devices (avoiding the effect of electric field crowding) [1, 15]. Impact ionization coefficients are defined as the number of electron–hole pairs generated by impact ionization per unit length under a given electric field. Compared to Si, the breakdown electric field strength of 4H-SiC at a given doping density is ten times higher [16], as shown in fig1.7. This leads to two important aspects for electronic applications:

- it is possible to fabricate devices in SiC with the same dimension of a device in Si but that can stand ten times higher voltage before the break down;

- it is possible to fabricate devices in SiC that work at the same voltage of a device
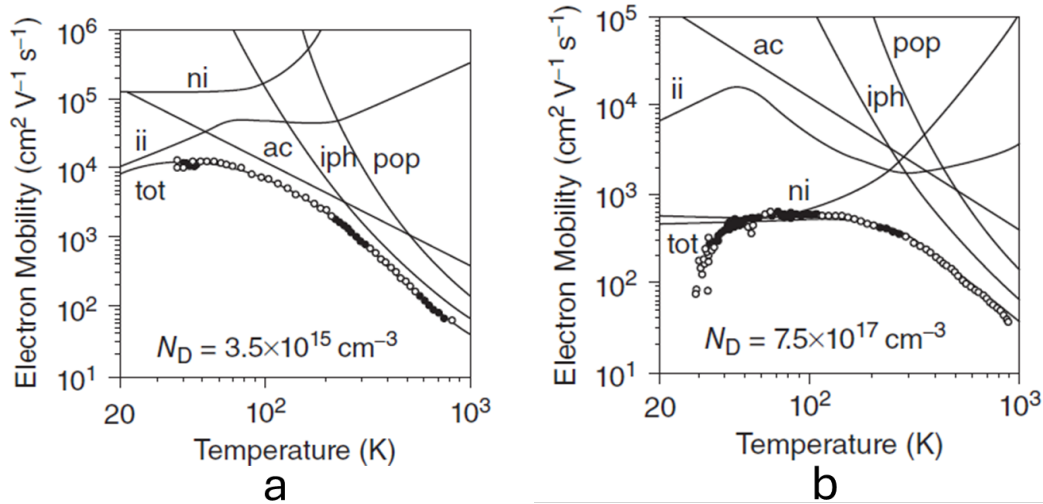
Figure 1.6: *Temperature dependence of electron mobility in lightly-doped n-type 4H-SiC (a) and in heavily-doped n-type 4H-SiC (b). In each case, the mobility determined by different scattering processes is represented [13].*

in Si but that are ten times smaller.

It is clear that the high critical breakdown electric field strength of SiC, especially for the hexagonal polytypes, is the main reason why SiC is so attractive for power device applications.

1.1.3 Mechanical and Thermal Properties

As mentioned before, Si-C bonds are similar for all SiC polytypes and as a consequence mechanical and thermal properties are very similar among different SiC polytypes [3]. Thermal conductivity is influenced mainly by the doping density and crystal direction (as well as temperature) and at room temperature it is in the range 3.3-4.9 $Wcm^{-1}K^{-1}$ that is three times higher than Si [17]. In terms of mechanical properties, SiC is one of the hardest known materials and its high hardness and elasticity retains even at very high temperatures [18]. The major mechanical and thermal properties of SiC and Si for comparison are reported in table 1.1. The high thermal conductivity coupled with low thermal expansion coefficient (about $4x10^{-6}/°C$) and high strength give this material also exceptional thermal shock resistance qualities.

1.1.4 Other Properties

Another interesting and useful aspect of SiC is that it is relatively easy to control both n-type and p-type doping over a wide range. For n-type doping typically Nitrogen of Phosphorus are used whereas Aluminum for p-type doping. Nitrogen substitutes at the C lattice sites, while Phosphorus and Aluminum substitute at the Si lattice sites [1, 19]. In hexagonal polytypes the ionization energies of dopants depend on the lattice
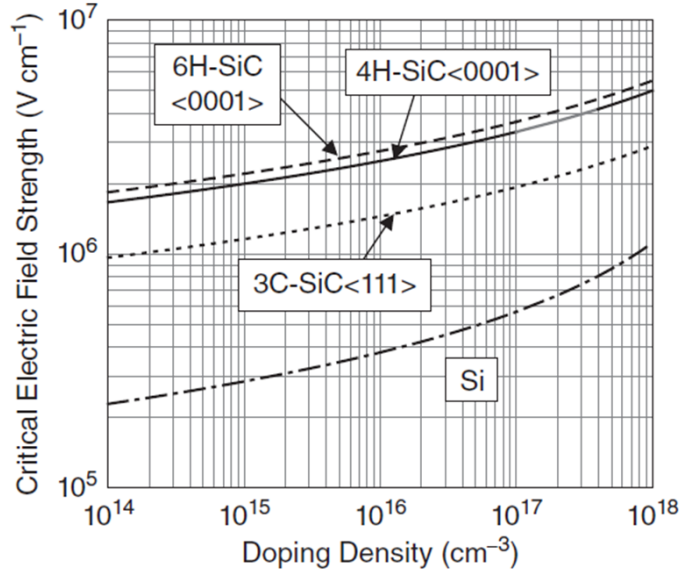
Figure 1.7: *Critical electric field strength versus doping density for 4H-SiC (along [0001] direction), 6H-SiC (along [0001] direction) and 3C-SiC (along [111] direction) [1].*

site, hexagonal or cubic site. This is another example of the "site effect" discussed above. Thanks to the wide bandgap, the intrinsic carrier density at room temperature is very low in SiC, for example is $5x10^{-9}cm^{-3}$ for 4H-SiC (for Si is $\sim 10^{10}cm^{-3}$). This explains why SiC electronic devices can operate at high temperatures with low leakage current. Furthermore, SiC is the only compound semiconductor that can be thermally oxidized to give high-quality SiO_2 (the same native oxide as Si), a fundamental aspect for devices production [20]. Lastly, SiC exhibits extremely high chemical inertness, for example to perform wet etching is very difficult because neither acids nor alkali attach the SiC surface at room temperature [20].

1.2   Synthesis

SiC is known by large time (as the mineral moissanite) and was mainly used in the field of industry as an abrasive, as heating elements and as cutting tools due to its high endurance and temperature resistance. In fact, the physical and chemical stability of SiC and the existence of various polytypes has made the crystal growth of SiC extremely difficult and the first use of SiC as a semiconductor started in the 1960s thanks to the works of Lely that allowed to get small pure SiC crystals plates by a sublimation technique [24]. In order to produce a device semiconductor, the first step is to grow an epitaxial layer, of certain thickness and doping, on a degenerate doped substrate trying to limit the formation of defects on both substrates and epitaxial layers. The main synthesis techniques of substrates and epitaxial layers are described below.

Table 1.1: *Major physical properties of low n-type doped 3C, 4H, 6H and Si at room temperature ([1, 3, 14, 17, 18, 21, 22, 23].*

|	3C	4H	6H	Si
Stacking sequence	ABC	ABCB	ABCACB	-
Bandgap (eV)	2.36	3.26	3.02	1.12
Exciton gap (eV) (at 2K)	2.36	3.26	3.02	
Relative dielectric constant				11.9
$\epsilon_r \perp$ c-axis	9.72	9.76	9.66	
ϵ_r // c-axis	9.72	10.32	10.03	
Electron mobility (cm^2 V^{-1}s^{-1})				1200
μ_e // c-axis	1000	1200	100	
$\mu_e \perp$ c-axis	1000	1020	450	
Electron saturated drift velocity (cm s^{-1})	$\sim 2\times10^7$	$\sim 2.2\times10^7$	$\sim 1.9\times10^7$	1×10^7
Electron effective mass in units of electron rest mass m$_0$				m$_e^l$=0.98 m$_e^t$=0.19
m$_e$ // to c-axis	0.67	0.33	2.0	-
m$_e \perp$ to c-axis	0.25	0.42	0.48	-
Intrinsic carrier density (cm^{-3})	0.1	5×10^{-9}	1×10^{-6}	$\sim 10^{10}$
Hole mobility (cm^2 V^{-1}s^{-1})	100	120	100	~ 280
Hole saturated drift velocity (cm s^{-1})	$\sim 1.3\times10^7$	$\sim 1.3\times10^7$	$\sim 1.3\times10^7$	$\sim 1\times10^7$
Hole effective mass in units of electron rest mass m$_0$				m$_{hh}$=0.49-m$_{lh}$=0.16
m$_h$ // to c-axis	~ 1.5	1.75	1.85	-
m$_h \perp$ to c-axis	~ 0.6	0.66	0.66	-
Breakdown electric field (MV cm^{-1})				0.6
E_B // to c-axis	1.4	2.8	3.0	
$E_B \perp$ to c-axis	1.4	2.2	1.7	
Thermal conductivity (W cm^{-1} K^{-1})	3.3-4.9	3.3-4.9	3.3-4.9	~ 1.5
Young's modulus (GPa)	310-550	390-690	390-690	160
Elastic constant (GPa)				
c$_{11}$	290	500	500	166
c$_{12}$	235	111	111	64
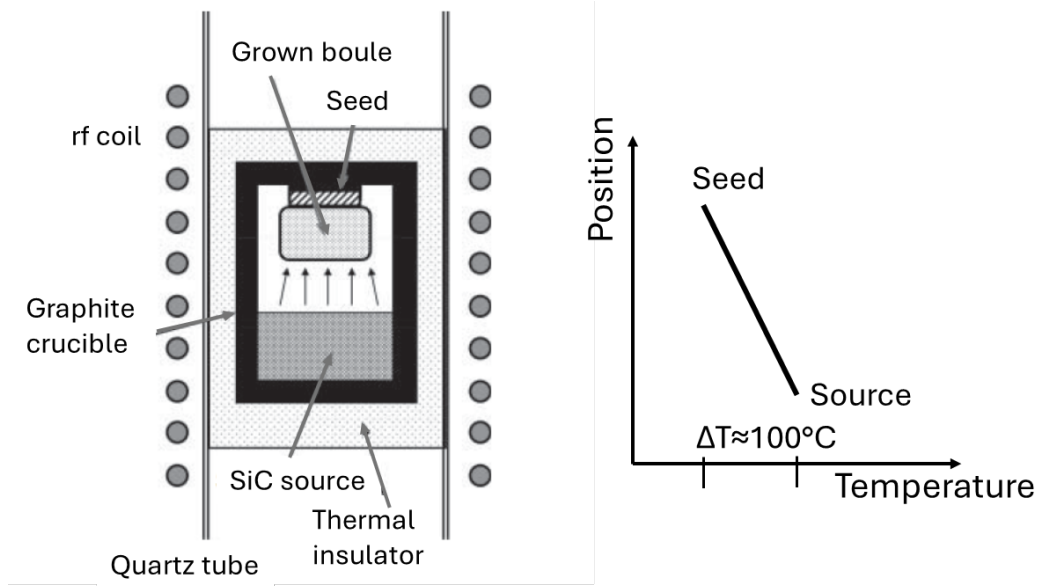
Figure 1.8: *Scheme of a crucible and approximate temperature profile used for seeded sublimation growth of SiC. Adapted from [24].*

1.2.1 Substrates

At the end of 1970s Tairov and Tsvetkov improved the Lely synthesis and invented a method for the growth of SiC boules, the modified Lely method or seeded sublimation method [24]. A schematic illustration of a crucible for the modified Lely method is reported in fig.1.8. The SiC seed crystal, (usually get by Lely method) is positioned at the top of the cylindrical crucible. On the contrary, the SiC source (SiC powder or sintered poly-crystalline SiC) is placed at the bottom of the crucible. The crucible, that is thermally isolated by graphite felt or porous graphite, is heated up to 2300-2400 $°C$ by resistive heating or radio frequency induction. At this temperature the SiC source sublimes and the sublimed species are guided to the seed by a high-purity low pressure Ar or He flow. The sublimed species condense and crystallize on the seed because its temperature is fixed at about 100 $°C$ lower than the source temperature. The growth rate depends essentially on sublimation rate (related to the SiC source temperature) as well as transport efficiency from the source to the seed (related to pressure, temperature gradient, distance between source and seed). The main sublimed species are Si, Si_2C, and SiC_2 so the gas phase in sublimation growth is usually Si-rich because of preferential evaporation of Si from the SiC source. This can lead to the graphitization of the source so silicon is added to the source to maintain the stoichiometry in order to avoid carbon inclusions in the growing crystal or boule. Furthermore, the growth is carried out in a quasi-closed graphite crucible, and it is possible to control only the process parameters such as the temperature and pressure from the outside (without monitoring the inside). Bulk SiC crystal can be grown from gases with a technique known as high-temperature chemical vapor deposition (HTCVD) first published by Kordina in 1996
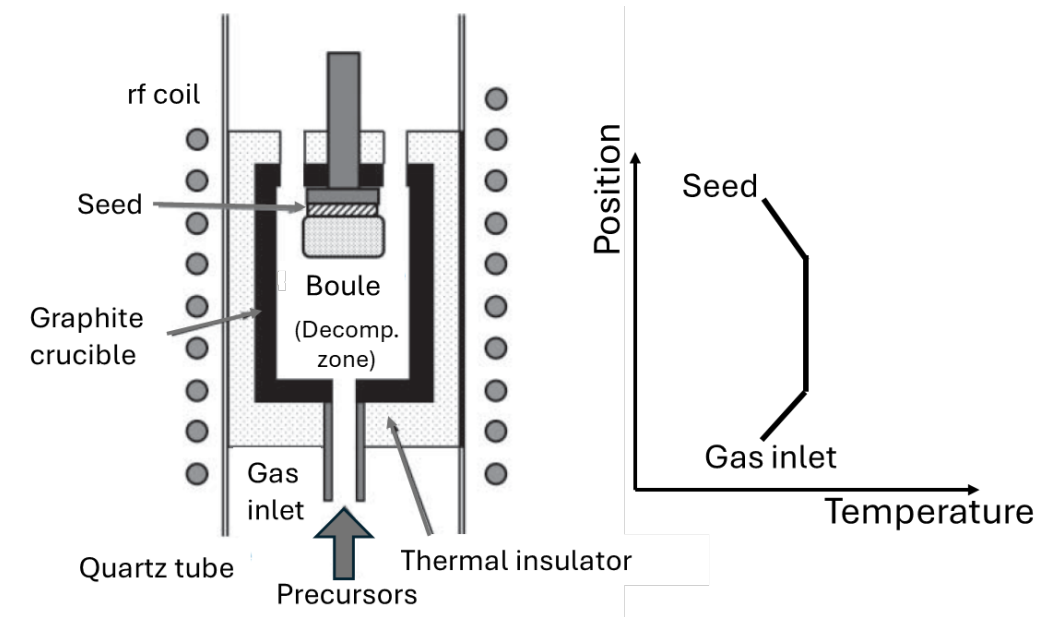
15

Figure 1.9: *Scheme of a reactor and approximate temperature profile used for HTCVD of SiC. Adapted from [24].*

[25]. A scheme of the HTCVD reactor is reported in fig1.9. In this case, the crucible is made of graphite, the seed crystal is placed at the top and there is a gas inlet at the bottom and gas outlet at the top. SiH_4 is used as Si precursor and a hydrocarbon such as C_2H_4 and C_3H_8 as C precursor. The precursor gases are guided through a heating zone to the seed by the carrier gas (argon, hydrogen or a mix of them). This setup is very similar to that of the vertical CVD reactors for the epitaxial growth but the temperature range for bulk SiC is extremely high 2100-2300 $°C$. The growth rate can reach 0.7 mm/h. The main advantage of HTCVD is the possibility to grow high-purity materials thanks to the possibilities to use high-purity gas as precursor, to control the Si/C ratio and the continuous supply of source material (gas inlet can be controlled independently). However, seeded sublimation growth is the most mature technique and is the most used for substrates production today.

For electronic applications it is mandatory to grow SiC boules of a desired single polytype but due to the low stacking faults energy for SiC, polytype mixing may happen during the growth specially when the growth conditions are not optimized [24]. Experimental evidences show that the factors that influence the polytype are the temperature and pressure of the process, the C/Si ratio, the polarity of the seed (Si or C face) and the hexagonality of the polytype (defined as the ratio of h and k site of a polytype). For example, 4H-SiC preferentially grows at relatively low temperature and pressure than 6H-SiC (as shown in fig.1.10) and it is more stable than 6H-SiC in C-rich growth conditions [26].

16

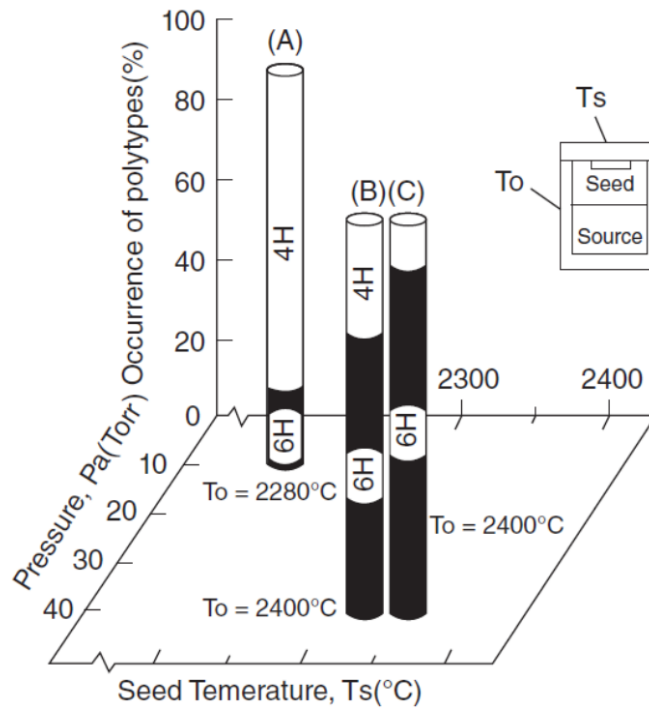**Figure 1.10:** *The effects of growth temperature and pressure on polytype stability in the seeded sublimation growth of SiC [26].*
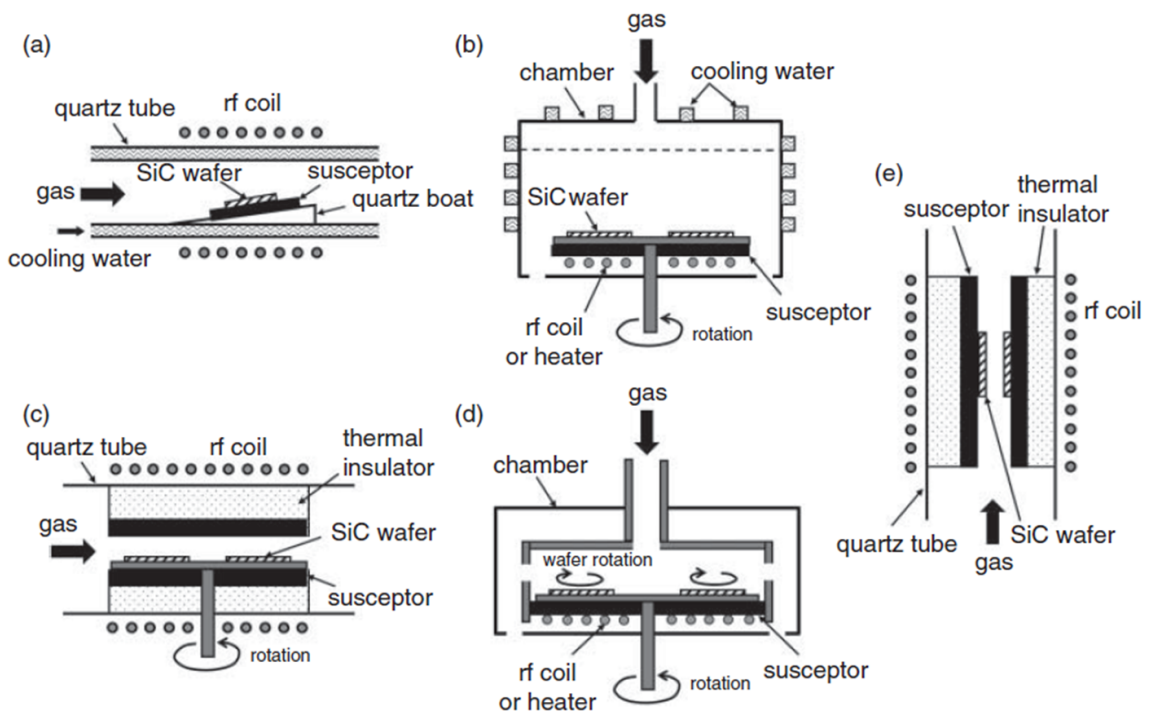

Figure 1.11: *Illustrations of several typical reactors used for SiC CVD. **a)** Horizontal cold-wall reactor, **b)** vertical cold-wall reactor, **c)** horizontal hot-wall reactor, **d)** hot-wall planetary reactor and **e)** vertical chimney-type reactor [27].*

1.2.2 Epitaxial Layers

To grow epitaxial layer with designed thickness and doping density is fundamental for the realization of devices for electronic applications. Epitaxial growth consists in the growth, on top of a substrate material, of a crystalline layer that maintains the crystalline structure of the substrate [27]. The process is called homoepitaxy when the substrate and the epilayer are the same material (i.e. 4H-SiC on 4H-SiC). Conversely, when the substrate and the epilayer are different materials, the process is called heteroepitaxy (i.e. 3C-SiC on 4H-SiC). Today, homoepitaxial growth by chemical vapor deposition (CVD) using step-flow growth controlling the C/Si ratio is the most utilized growth methods for SiC epitaxial layers.

Despite the existence of several reactors employed for SiC CVD (horizontal or vertical geometry and cold wall or hot wall configurations, reported in fig.1.11), each process essentially consists in an in situ etching to remove the subsurface damages and to get a regular step structure followed by the main epitaxial growth. The etching is usually performed with pure H_2, HCl/H_2, hydrocarbon/H_2, or SiH_4/H_2 at very high temperature (the same temperature used for the main growth). The employed precursors are usually SiH_4, C_3H_8 and C_2H_4 and the carrier gas are hydrogen and argon. N_2 and $Al(CH_3)_2$ are used for n-type and p-type dopants, respectively. The typical growth temperature is in the range 1100–1700 °C and the growth rate is in the range 3–15 μm/h.

To obtain a stepped surface, the SiC crystal is sliced with an off-angle rather than exactly perpendicular to the c-axis, resulting in a substrate surface with high density of atomic steps. The cutting is done along the direction $[11\bar{2}0]$ because the plane $[11\bar{2}0]$ is the one with the highest density of atoms. Today the standard value of the off-angle with respect to the direction $[11\bar{2}0]$ is 4°. The introduction of the off-angle has been the key point to preserve the polytype in homoepitaxial growth. The advantage of an off-axis growth rather than an on-axis one is shown in fig.1.12. In particular, the growth modes and stacking sequences of the layers grown on-axis 4H-SiC(0001) and off-axis 4H-SiC(0001) are reported in fig.1.12a and fig.1.12b, respectively. A detail of the bond configuration near an atomic step and on the (0001) terrace of 4H-SiC is depicted in fig.1.13. The precursors gases are heated and decomposed, then the source species diffuse toward the substrate surface where they are adsorbed. These species migrate on the surface and are incorporated at the crystal steps and/or at kinks, so the area where the potential is lower. A competitive growth process (nucleation on terraces) occurs when the supersaturation is high enough. In details:

- On on-axis [0001] the steps density is very low and larger terraces [0001] exist, as shown in fig.1.12a. As a consequence, the crystal growth may initially occurs on the terraces through two-dimensional nucleation facilitated by the high level of supersaturation. As indicated in fig.1.10, the polytype of the grown layers
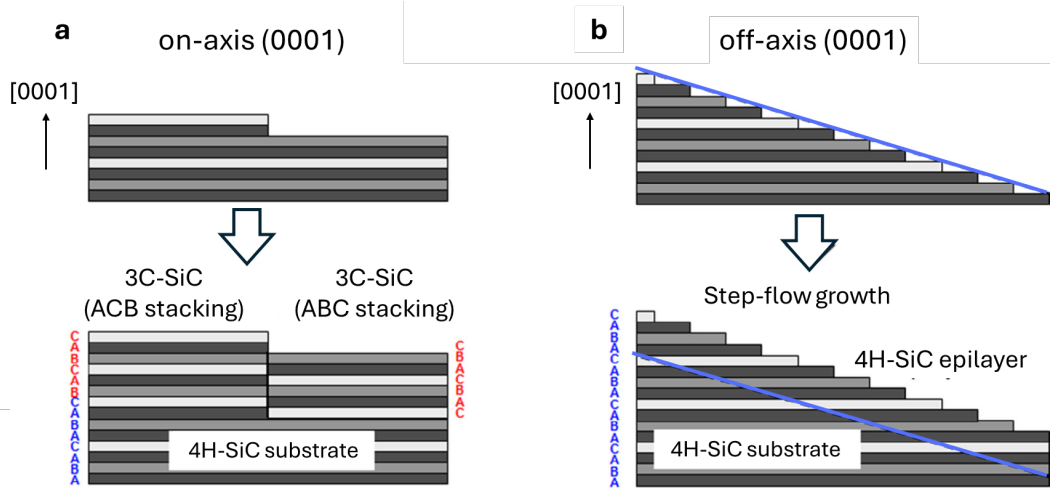
Figure 1.12: *Schematic representation of growth modes and stacking sequences of SiC layers grown on **a)** on-axis 4H-SiC(0001) and **b)** off-axis 4H-SiC(0001). Adapted from [28].*

is determined by the growth conditions, especially temperature, and the most stable polytype at the typical temperature of epitaxial growth is 3C-SiC [26]. This phenomena can lead to the change of the polytype during the epitaxial growth that means poor crystal quality.

- On off-cut substrates the steps density is high, and the terraces width is small, as shown in fig.1.12b. Consequently, the adsorbed species are able to reach the steps easily. The incorporation of the adsorbed species on the steps is determined by the bonds of the step (as evidenced in fig.1.13) [28]. For this reason the homoepitaxial growth on off-cut substrates can be considered a lateral growth from the steps and is referred to as "step-flow growth". This mechanism allows to preserve the polytype during the epitaxial growth because the edge of the step acts as a template to replicate the polytype from the substrate. This implies that the polytype of SiC epilayers can be controlled by the step density of substrates.

The main disadvantage of epitaxial growth using off-cut substrates is that basal plane dislocations (BPDs) propagate from the substrate surface to the epilayer. It is known that the BPDs, when high currents go through a device, act as a source of Shockley stacking faults formation, leading to increased resistance and resulting in the destruction of the device itself (known as bipolar degradation) [30]. This phenomenon can be reduced decreasing the off-angle and/or converting the BPDs to threading edge dislocations (TEDs) [31]. BPDs and TEDs are typical dislocations of crystalline materials that will be discussed in the next sections.

19

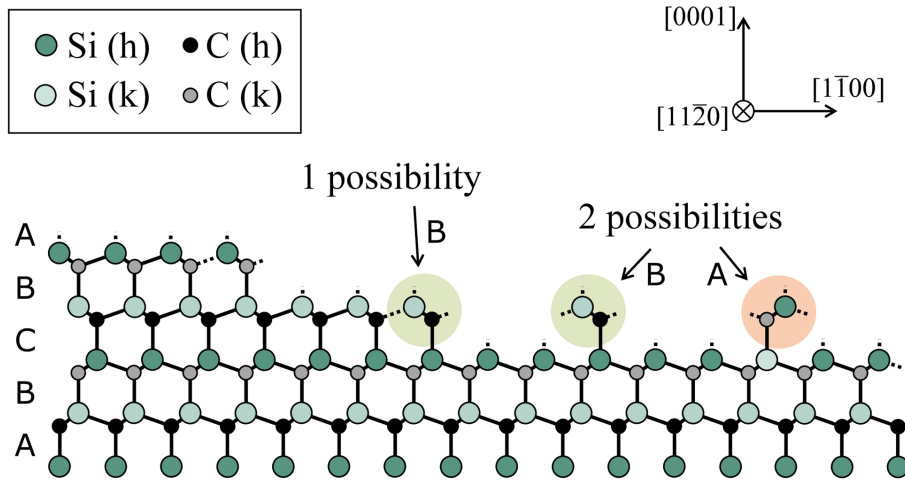**Figure 1.13:** *Bond configuration near an atomic step and on the (0001) terrace of 4H-SiC [29].*

1.3 Major Defects in Silicon Carbide

Semiconductors, intentionally engineered or naturally, have defects. The properties of these defects, from impurities to native and extended defects, play a fundamental role in a wide range of applications. For example, the concentration of defects influences the reliability of devices as well as their performance, the introduction of deep levels that act as trapping centers decreases the minority charge carrier lifetime, the control of defect populations can enhance the efficiency of light-emitting diodes and solar cells, on the other side dopants spins and optically active centers represent promising building blocks for quantum computers [30, 32, 33, 34]. Defects can be introduced during the growth and during all the steps of devices processing. Essentially, it is possible to classify defects according to their dimensionality: zero-dimensional such as point defects, one-dimensional such as dislocations, two-dimensional such as stacking faults and surface defects, and three-dimensional such as grain boundaries and precipitates [35]. All these defects can exist in both bulk and epitaxial layer of SiC but usually their occurrence and importance is different.

1.3.1 Typical Point Defects

The zero-dimensional defects are known as point defects, imperfections that occur at a specific lattice site (or few) of a crystal. So, their impact is extremely negative in epitaxial layers. Point defects can be divided in native or intristic defects and extrinsic defects. The former involve atoms from the host crystal, the latter involve impurity atoms (dopants or other impurities residues of the growth). Point defects can occupy substitutional or interstitial sites within the crystal structure. A schematic illustration of major point defects in 4H-SiC is reported in fig.1.14. A vacancy is an unoccupied
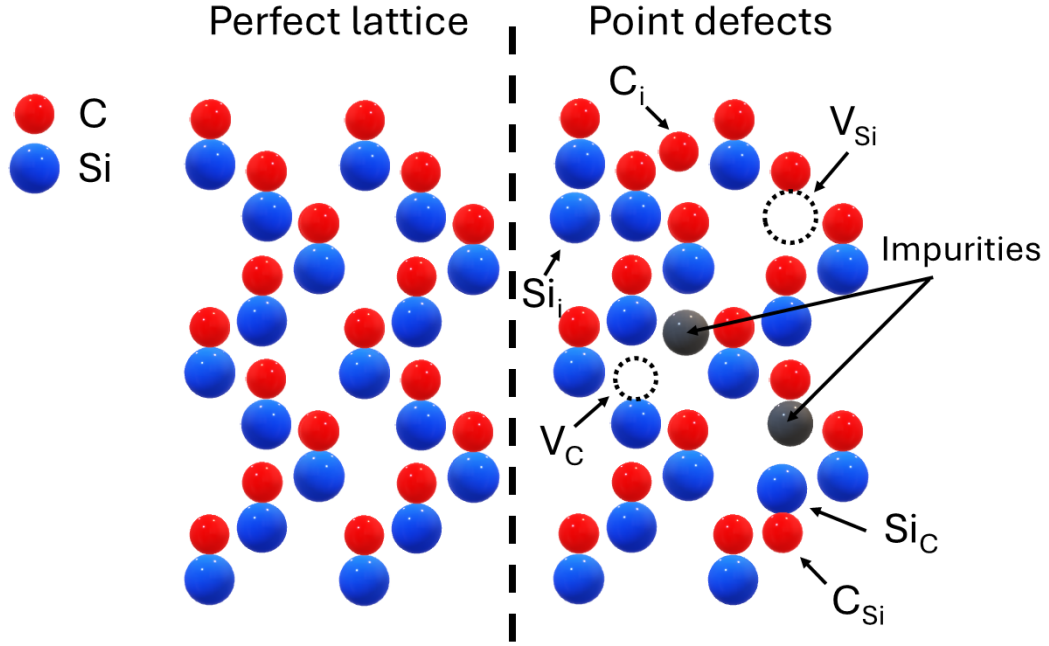
Figure 1.14: *Schematic representation of point defects in 4H-SiC lattice.*

lattice site, an anti-site occurs when an atom of one species occupies the lattice site of the other atom species and interstitial is an additional atom (self-interstitial or impurities) in between lattice sites. As a consequence, SiC has six basic intristic defects (carbon vacancy (V_C), silicon vacancy (V_{Si}), carbon anti-site (C_{Si}), silicon anti-site (Si_C), carbon and silicon interstitials (C_i and Si_i)) with the addition of the possible defects complexes such as divacancies or anti-site vacancy pairs. Furthermore, the same point defect has different properties in different SiC polytypes as well as, due to the "site effect", in a specific SiC polytype, the same kind of point defect can have different electronics properties at h and k_n site. The point defects that usually have more impact, because they are electrically active, on 4H-SiC are:

- the carbon vacancy (V_C), the one with the lowest formation energy ($\sim 3eV$), so the most abundant [36, 37];

- the silicon vacancy (V_{Si}), having formation energy about 3-4 eV higher than that of the V_C [38, 39];

- the carbon antisite vacancy pair ($C_{Si} - V_C$), specially in p-type SiC [40]. This defect has been identified in the positive and in negative charge states [41], and each state can have four configurations due to the site effect [42];

- The divacancy $V_C - V_{Si}$, caused by the migration of V_C and V_{Si}. Also this defect can have four configurations due to the not-equivalent lattice sites [43, 44].

V_C exists in several charge states that have been identified by EPR (electron paramagnetic resonance) spectroscopy. In particular, V_C^{2-} has been attributed to the fa-

Figure 1.15: a) *Energy positions of the V_C obtained through theoretical calculations and Electron Paramagnetic Resonance measurements. Energy position of $Z_{1/2}$ and $EH_{6/7}$ deep levels obtained by DLTS [12].* **b)** *Energy levels of other expected intrinsic defects in 4H-SiC [12].*
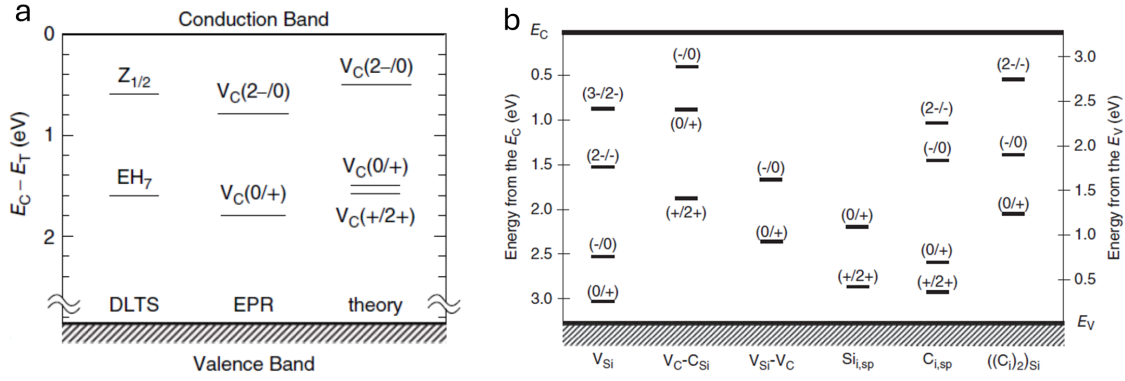
mous deep level known as "lifetime killer defect" $Z_{1/2}$ by comparing the concentrations obtained by DLTS (deep level transient spectroscopy) with those obtained by EPR (summarized in fig.1.15a) [45]. Also the deep level defect known as $EH_{6/7}$ has been attributed to a carbon vacancy with a different charge state. $Z_{1/2}$ (E_C-0.63 eV) [46] and $EH_{6/7}$ (E_C-1.55 eV) [47] are considered the most important deep levels of SiC due to their exceptional thermal stability (up to 1700°) and because they are the defects with the highest concentration in epitaxial layers [28]. The energy positions of several intrinsic defects expected in 4H-SiC, obtained by simulations [36, 48, 49], are reported in fig.1.15. To date, the experimental assignment of all the deep levels to the corresponding intrinsic defect has not yet been obtained completely.

1.3.2 Typical Extended Defects in SiC

In contrast to point defects that are confined to a specific lattice site (or few), extended defects can reach the dimension of few μm. The most widespread extended defects in SiC are dislocations, stacking faults and surface defects. In details:

- dislocation is a one-dimensional "line" defect that involves a distortion of the crystal lattice that is quantified by the Burgers vector, often denoted as **b** [52]. According to the propagation direction, dislocations are classified in TED (Threading Edge Dislocation), BPD (Basal Plane Dislocation) and TSD (Threading Screw Dislocation). TED and BPD have the same Burgers vector $[11\bar{2}0]/3$ that results in an extra half plane or a missing half plane within the crystal and the dislocation is in correspondence of the edge of this plane as depicted in fig.1.16a. When the dislocation is along the basal plane (AB line in fig.1.16a.) the dislocation is a BPD, when it is along the [0001] direction (BC line in fig.1.16a.) the dislocation is a TED. Often, inside the boule crystals, the conversion from BPD to TED and vice-versa is observed [31, 53]. In TSD the lattice plane shifts by
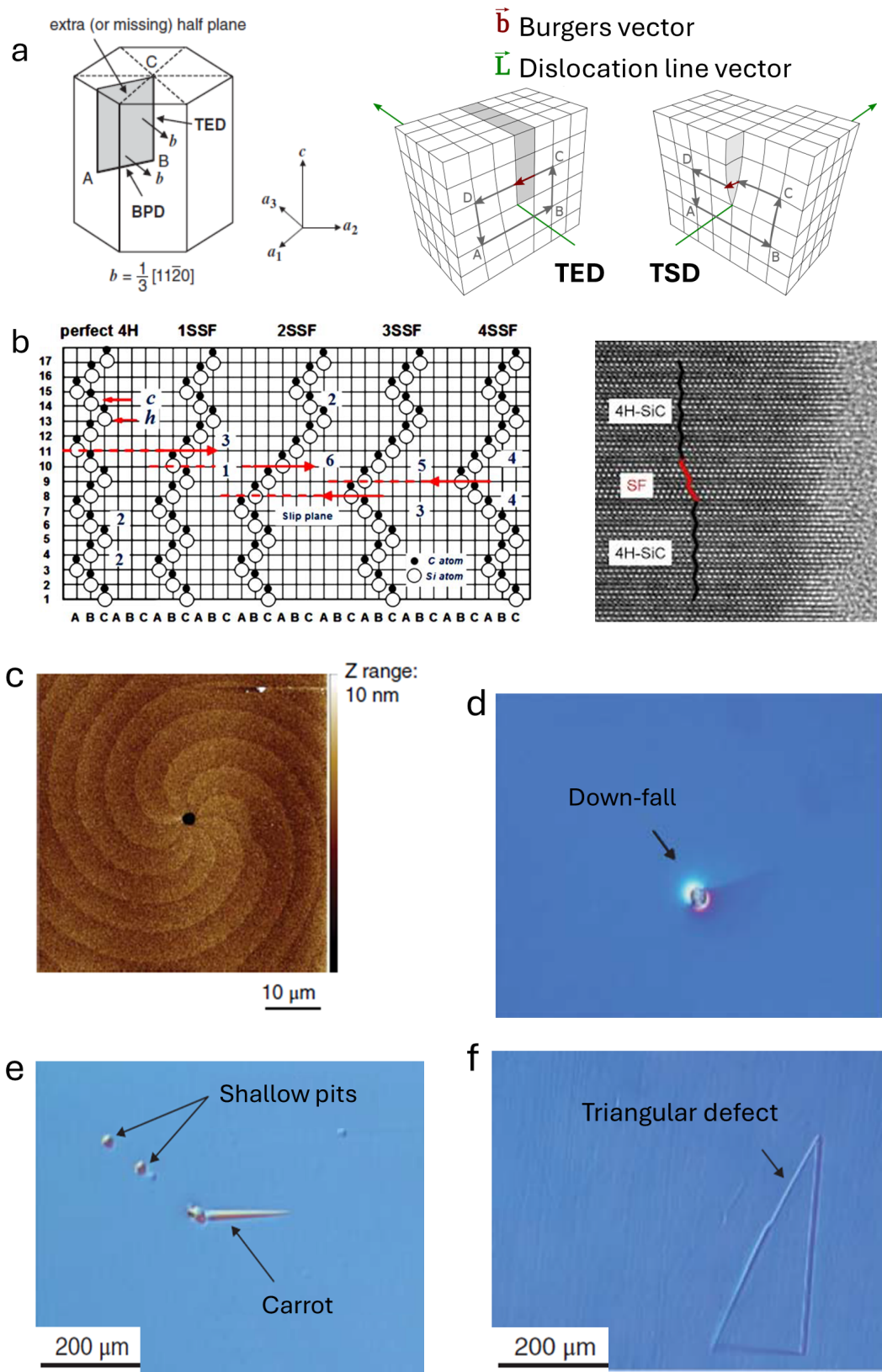
22

Figure 1.16: *a) Schematic illustration of an extra half plane in hexagonal SiC crystal [24] and of TED and TSD, adapted by Martin Fleck from [35]. **b)** Scheme of some SFs and a TEM image in 4H-SiC [50, 51]. **c,d,e,f)** typical surface defects, in order a micropipe, a down-fall, shallow pits, a carrot and a triangular defect [27].*

one layer or more like a spiral staircase and the Burgers vector is parallel to the dislocation line [54]. Furthermore, also mixed dislocations exist. In fig.1.16a. it is also reported an illustration of a screw and an edge dislocation. Dislocations are mainly due to thermal stress caused by inhomogeneous temperature during the boule growth or during the cooling.

- Stacking fault (SF), as suggested by the name, is an error in the stacking sequence of a polytype and involves the presence of a plane of atoms that is in the wrong sequence. For this reason SFs are an example of two-dimensional defects [52]). Considering the low stacking fault energy formation, 14 mJm^{-2} for 4H-SiC and 2.9 mJm^{-2} for 6H-SiC [55], and the occurrence of many SiC polytypes, it is clear that SFs are very common defects and that a multiple of SFs exists, some examples are reported in fig.1.16b. Unfortunately, the formation of SFs takes place during epitaxial layers growth even if the substrate is SFs free. It is possible to identify SFs by cross-sectional TEM, furthermore most of the SFs are characterized by photoluminescence emission [50, 56, 57, 58].

- Micropipes defects are hollow core associated with a super-screw dislocation (screw dislocations with Burgers vectors larger than 1c, where c is the lattice parameter along the [0001] direction) [59]. Essentially, a micropipe is a pinhole, with a diameter from 0.5 μm to several micrometers, extending along the [0001] direction through the entire SiC wafer, as shown in fig.1.16c. Therefore, SiC devices that contain just a micropipe exhibit degraded performance that lead to devices failure [60].

- Surface defects arises during epitaxial growth, but the formation mechanism is not well understood. The most common surface defects in 4H-SiC are down-fall (fig.1.16d), carrots (fig.1.16e), comets, pits (fig.1.16e), and triangular defects (fig.1.16f). The carrots and triangular defects are elongated along the step-flow growth direction. The comets are carrots with a structure similar to a "tail". The down-fall is a SiC particle initially formed on the susceptor wall of the reactor that falls down on the surface. The density of surface defects is mainly influenced by the quality of the substrates surface and the conditions used for the growth process [27, 61].

Most of the dislocations in 4H-SiC homoepitaxial layers originate from dislocations in 4H-SiC substrates because, as discussed previously, during the step-flow growth the substrate acts as a template for the epitaxial layer. As a consequence, assuming that the conditions of epitaxial layer growth are optimized, the dislocation density of SiC epitaxial layer depends on the quality of the substrate. In the same way the quality of the seed is a fundamental aspect in the growth of the bulk crystal, in fact the TEDs and BPDs are replicated from the seed to the boule. In general, all the extended defects (of

the epitaxial layers) affects negatively the SiC power devices in several ways. The most common effects are: local reduction of the minority carrier lifetime, increase of the on-resistance, increase of the leakage current, reliability of the gate oxide, lowering of the breakdown electric field strength and the degradation of the device itself [12, 60, 62]. However, notable technological improvements have been reached during the last years and high quality homoepitaxial wafers of 6 inch of 4H-SiC are available on the market.

1.4 Applications

As anticipated, SiC was mainly used in the field of industry as an abrasive, as heating elements and as cutting tools material due to its high endurance and temperature resistance. Nowadays, thanks to the optimization of the growth methods of bulk and epitaxial layer the potential of SiC as semiconductor can be fully exploited.

The wide bandgap, the breakdown electric field, the thermal conductivity, the mechanical strength, the chemical inertness, the high saturation drift velocity, the switching velocity, the intrinsic radiation hardness and the easy control of doping, make SiC a promising material to realize high-power, high-frequency and high-temperature devices that can also work in harsh environments [33, 63, 64, 65, 66, 67, 68, 69]. These devices include metal-oxide-semiconductor field-effect transistors (MOSFETs), junction field-effect transistors (JFETs), Schottky diodes and bipolar junction transistors (BJTs). It is possible to realize very efficient power supplies, grid-tied inverters for solar and wind energy systems, electric vehicle powertrains, high-power industrial motor drives, etc... Several SiC-based particle and radiation detectors have been developed in the last year as well as biomedical devices [70, 71, 72, 73, 74, 75, 76, 77]. They are employed in nuclear power plants, particle accelerators, and space missions to monitor radiation levels, detecting nuclear radiations, and ensuring the safety and reliability of nuclear facilities and space missions. SiC-based sensors for pressure and temperature have been developed to be used in high temperatures, pressures, and corrosive environments such as oil and gas industry [78, 79]. Furthermore, SiC is the ideal substrate for the growth of high quality graphene and other 2D materials such as transition-metal dichalcogenide (TMDC), Gallium nitride (GaN) and hexagonal Boron nitride (h-BN) [80, 81, 82, 83, 84, 85]. Last but not least, SiC is a promising material (along with diamond) for quantum computing applications because is possible using the SiC point defects as qubits [28, 86].

1.5 Exciton in Solids

By definition, exciton is an electrostatically neutral quasi-particle that transfers energy without transporting charge. It consists of an electron in the conduction band and an

hole in the valence band that are bound due to Coulomb interaction and that propagate together [87, 88]. Excitons are mainly generated through optical absorption, but can also be produced by electron-hole pair injection, via Auger processes, through impact ionization and in semiconductor quantum structures such as quantum wells, wires, or dots by quantum confinement [87, 88]. Excitons can be divided into two categories depending on their confinement in the crystal lattice or on the strength of the exciton interaction with phonons. In particular:

- in Wannier-Mott or weakly-bound excitons, represented in fig.1.17, the electron and the hole are spatially separated, in different lattice sites, due to weak electron-lattice coupling and the exciton can move freely within the crystal. It is possible to describe this kind of exciton considering it moving in an uniform crystal with dielectric constant ϵ_r [10, 88, 89]. The exciton energy levels can be well approximated by the Rydberg energy levels of an hydrogen atom modifying appropriately the reduced effective mass μ of the electron-hole system ($\frac{1}{\mu} = \frac{1}{m_e^*} + \frac{1}{m_h^*}$), where electron and hole effective masses are m_e^* and m_h^*, and considering the dielectric constant of the crystal:

$$E_n = E_g - \frac{\mu R_H}{m_e \epsilon_r^2} \frac{1}{n^2} \tag{1.1}$$

where E_g is the band gap energy, R_H is the Rydberg constant of the hydrogen atom, m_e is the free electron mass and n is the principal quantum number. According to this description, in absorption spectra (at low temperature) it is possible to observe several absorption peaks in the pre-edge absorption region in correspondence of n=1,2,3... With this model the radius of the exciton is $r_n = \frac{m_e \epsilon_r a_B}{\mu} n^2$, where a_B is the Bohr radius. $n = 1$ corresponds to the condition of shortest radius and lowest energy, in this case the binding energy of the exciton, the energy needed to ionize it, is given by:

$$E_b = \frac{\mu R_H}{m_e \epsilon_r^2}. \tag{1.2}$$

Usually, the binding energy for weakly-bound exciton is about tens of meV, comparable with the Boltzmann energy at room temperature (T=300 K $kT \approx 0.026 eV$), so they tend to dissociate into free carriers at room temperature.

- in Frenkel or tightly-bound excitons, represented in fig.1.17, the electron and the hole are localized on the same lattice site due to their strong electron-lattice coupling. For this reason, these excitons are strongly influenced by local defects, impurities, or lattice distortions that create energy levels within the bandgap of the material that can trap excitons and/or induce the exciton recombination. In this case it is not possible to describe the exciton with an hydrogen-like model as the exciton is strictly localized on a single atom (of the crystal, defect, donor or
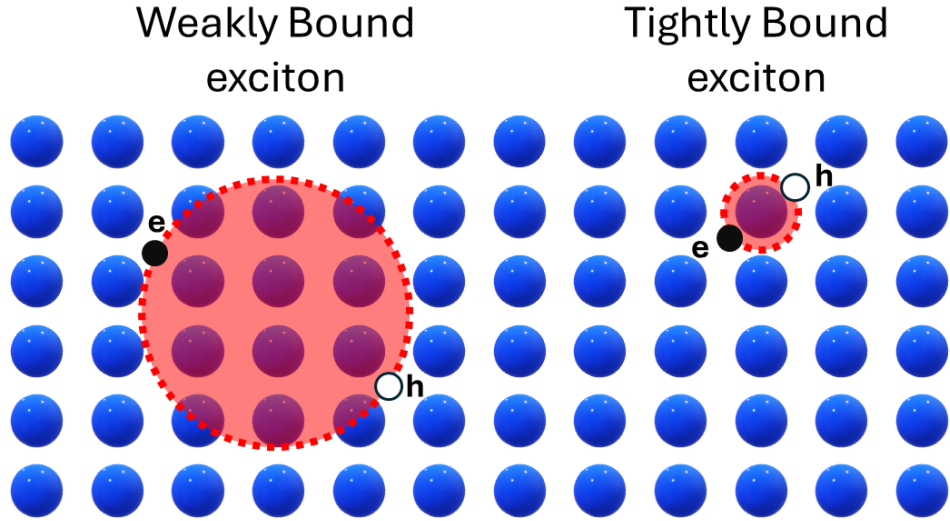
Figure 1.17: *Scheme of weakly bound (Mott-Wannier) and tightly bound (Frenkel) exciton.*

acceptor) and so the excitonic radius is comparable with the interatomic distance [10, 89]. As a consequence it is not possible to think to the tightly-bound excitons as moving in a uniform medium with a relative dielectric constant ϵ_r. Essentially, the Frenkel exciton is an excited state of a single atom and the excitation can hop/be transferred from atom to atom thanks to the coupling between neighbors as a wave (like all the excitation in a periodic structure) [88]. Frenkel excitons are typical of large bandgap crystals and their binding energy is hundreds of meV, much higher than the room temperature Boltzmann energy (T=300 K $kT \approx$ 0.026 eV), so it is possible to observe exciton peaks even at room temperature.

Of course, there are many intermediate cases of exciton.

Excitons tend to recombine through various mechanisms, the main processes include radiative path, non-radiative path and exciton-exciton annihilation [11]. In radiative recombination, the exciton recombination results in the emission of a photon with energy equal to the exciton binding energy. In non-radiative recombination, the energy can be dissipated in different ways including Auger recombination, in which the energy is transferred from the recombining exciton to another carrier (electron or hole), trap-assisted recombination that is caused by defects or impurities that can act as trapping centers for carriers (radiative decay could also occur depending on the energy level position of the defect), and also surface recombination, due to high surface defect densities or dangling bonds. In high exciton density conditions, excitons can interact with each other thanks to the Coulomb forces leading to exciton-exciton annihilation resulting in the generation of free carriers and heat.

Naturally, the mobility of the excitonic couple (under the influence of an external electric field or thermal energy) depends on various factors including the nature of the semiconductor material, the temperature, the thermal vibration of the lattice,

the presence of defects or impurities in the crystal lattice and the density of excitons [88]. For example, in materials with strong exciton binding energies, such as wide bandgap semiconductors, the mobility of the excitonic couples is lower compared to materials with weaker binding energies. This is a consequence of the strong localization of tightly bound excitons. At higher temperatures, thermal energy can promote the exciton dissociation which implies the electron-hole pairs separation into free carriers. This can increase the mobility of carriers and decrease the one of the excitons. Defects and impurities, in addition to act as trapping centers for excitons, can also scatter them overall reducing the exciton mobility.

The presence of exciton in semiconductor materials is linked to the wide bandgap and the study of their dynamics is relevant for the characterization of the material's transport properties in particular in connection to the presence of defects. This aspect will be deepened in the research here presented in connection to SiC.

Chapter 2

Basic Concepts of Methodologies

In this chapter the basic concepts of the main characterization techniques used in this thesis, micro-Raman spectroscopy and time-resolved photoluminescence spectroscopy (TRPL) are discussed. Both techniques involved the interaction between radiation and matter but they are fundamentally different.

2.1 Raman Spectroscopy

Raman spectroscopy is one of the most common techniques used for the investigation of structural properties of materials. It is a scattering spectroscopy that exploits the interaction of electromagnetic radiation, capable of causing variations in the vibrational levels of the material, with matter. What is evaluated in Raman spectroscopy is the variation between the incident and the scattered photon energy that fall within the infrared region. Essentially, radiation can be scattered in elastic or inelastic way giving rise respectively to [90, 91]:

- Rayleigh scattering, in which the scattered radiation has the same energy as the incident radiation, usually a laser source with frequency ν_0:

$$h\nu = h\nu_0 \tag{2.1}$$

- Raman scattering, in which the scattered radiation has different energy from the incident radiation, can be expressed by:

$$h\nu = h\nu_0 \pm h\Delta\nu \tag{2.2}$$

where $h\Delta\nu$ is the energy difference between two vibrational states. Therefore, the scattered photon can lose or acquire energy giving rise respectively to Stokes and anti-Stokes lines.

An example of Raman spectrum is reported in fig.2.1a. The spectrum consists of a very

intense line at frequency ν_0 (assumed as the frequency of the monochromatic source), due to the Rayleigh scattering, and a series of much less intense lines, due to Raman scattering, by a factor ranging from 10^{-5} to 10^{-8} of the intensity of the incident beam at both lower (Stokes) and higher (anti-Stokes) frequencies than ν_0 .

Several fundamental aspects of Raman scattering can be derived by using a classical description of the interaction between radiation and matter. As complicated as the oscillation of a molecule with many atoms may be, it is always possible to express such vibration as a combination of independent normal modes. Therefore, we can derive the classical description of Raman scattering considering the interaction of the incident radiation, described by a monochromatic (ν_0) electromagnetic plane wave, with a diatomic molecule. Let us introduce the electric field of the monochromatic plane wave:

$$E = E_0 \cos\left(2\pi\nu_0 t\right). \tag{2.3}$$

A diatomic molecule with vibration frequency ν_m is equivalent to a harmonic oscillator with frequency ν_m, thus it is possible to describe the variation of the internuclear distance as follows (q_0 is the equilibrium position):

$$q(t) = q_0 \cos\left(2\pi\nu_m t\right). \tag{2.4}$$

The electric field of the incident radiation (of frequency ν_0) induces an oscillating electric dipole moment P on the irradiated material:

$$P(t) = \alpha E_0 \cos\left(2\pi\nu_0 t\right) \tag{2.5}$$

where α is the polarizability of the molecule that depends on the material itself and on the position of the nuclei. For small atomic displacement from the equilibrium position q_0, the polarizability changes as:

$$\alpha(t) = \alpha_0 + \left.\frac{\partial\alpha}{\partial q}\right|_0 q_0 \cos\left(2\pi\nu_m t\right). \tag{2.6}$$

Replacing it in eq.(2.5) we get the following expression of the dipole momentum:

$$P(t) = \alpha_0 E_0 \cos\left(2\pi\nu_0 t\right) + \left.\frac{\partial\alpha}{\partial q}\right|_0 \frac{q_0 E_0}{2} \cos\left[2\pi(\nu_0 + \nu_m)t\right] + \left.\frac{\partial\alpha}{\partial q}\right|_0 \frac{q_0 E_0}{2} \cos\left[2\pi(\nu_0 - \nu_m)t\right]$$
$$\tag{2.7}$$

in which there are three different oscillating components. Since an oscillating electric dipole moment is a source of electromagnetic radiation, it can be stated that when a molecule vibrates with frequency ν_m and interacts with electromagnetic radiation of frequency ν_0, the system gives rise to radiation constituted by three components. One related to Rayleigh scattering with frequencies ν_0 and two related to Raman scattering with frequencies $\nu_0 \pm \nu_m$, in particular $\nu_0 - \nu_m$ for Stokes and $\nu_0 + \nu_m$ for anti-Stokes.

Actually, the polarizability is not necessarily an isotropic quantity and the relation between the electric field of incident radiation and the induced polarization of the material is associated to the polarizability tensor by the equation $P = \hat{\alpha}E$ that is equivalent to:

$$
\begin{bmatrix} P_x \\ P_y \\ P_z \end{bmatrix} = \begin{bmatrix} \alpha_{xx} & \alpha_{xy} & \alpha_{xz} \\ \alpha_{yx} & \alpha_{yy} & \alpha_{yz} \\ \alpha_{zx} & \alpha_{zy} & \alpha_{zz} \end{bmatrix} \begin{bmatrix} E_x \\ E_y \\ E_z \end{bmatrix}.
\tag{2.8}
$$

Since polarizability is usually a symmetric tensor $\alpha_{ij} = \alpha_{ji}$ for $i \neq j$. Consequently, a vibrational mode is Raman-active when one of these components is such that $\left.\frac{\partial \alpha}{\partial q}\right|_0 \neq 0$.

The intensity of the light emitted by the oscillating dipole is proportional to $|\ddot{P}|^2$ as follow:

$$
\begin{aligned}
I = \frac{16\pi^4}{3c^2} E_0^2 \Big\{ &\nu_0^4 \alpha_0^2 \cos^2(2\pi\nu_0 t) + (\nu_0 + \nu_m)^4 \left[\left.\frac{\partial \alpha}{\partial q}\right|_0 \frac{q_0}{2}\right]^2 \cos^2[2\pi(\nu_0 + \nu_m)t] \\
&+ (\nu_0 - \nu_m)^4 \left[\left.\frac{\partial \alpha}{\partial q}\right|_0 \frac{q_0}{2}\right]^2 \cos^2[2\pi(\nu_0 - \nu_m)t] \Big\} + cross - term
\end{aligned}
\tag{2.9}
$$

neglecting the cross term because the radiated power will average to zero over long time. The predicted ratio between the intensities of the Stokes and anti-Stokes lines is

$$
\frac{I_{Stokes}}{I_{Anti-Stokes}} = \left(\frac{\nu_0 - \nu_m}{\nu_0 + \nu_m}\right)^4 < 1
\tag{2.10}
$$

and is in contrast with experimental evidences as shown in fig.2.1a. This inconsistency is eliminated by the quantum theory of Raman scattering. However, it is possible to give a simplified qualitative description referring to the diagram of the energy levels of a molecule, represented in fig.2.1b. The transitions associated with the Raman effect are vibrational transitions that occur within the ground electronic state (E_0). When radiation with ν_0 frequency interacts with the system, two transitions occur (within the ground electronic state): one originating from the vibrational ground state $\nu = 0$ towards a virtual level m, and another from the first excited vibrational state $\nu = 1$ towards a virtual level m'. From both virtual states, rapid decay occurs:

- the decay from the virtual state m to the vibrational ground state $\nu = 0$ of the ground electronic state occurs with the emission of a photon of frequency ν_0, resulting in the Rayleigh line;

- the decay from the virtual state m to the first excited vibrational state $\nu = 1$ of the ground electronic state occurs with the emission of a photon of frequency $\nu_0 - \nu_m$, giving rise to the Stokes line;

- the decay from the virtual state m' to the vibrational ground state $\nu = 0$ of the ground electronic state occurs with the emission of a photon of frequency $\nu_0 + \nu_m$,
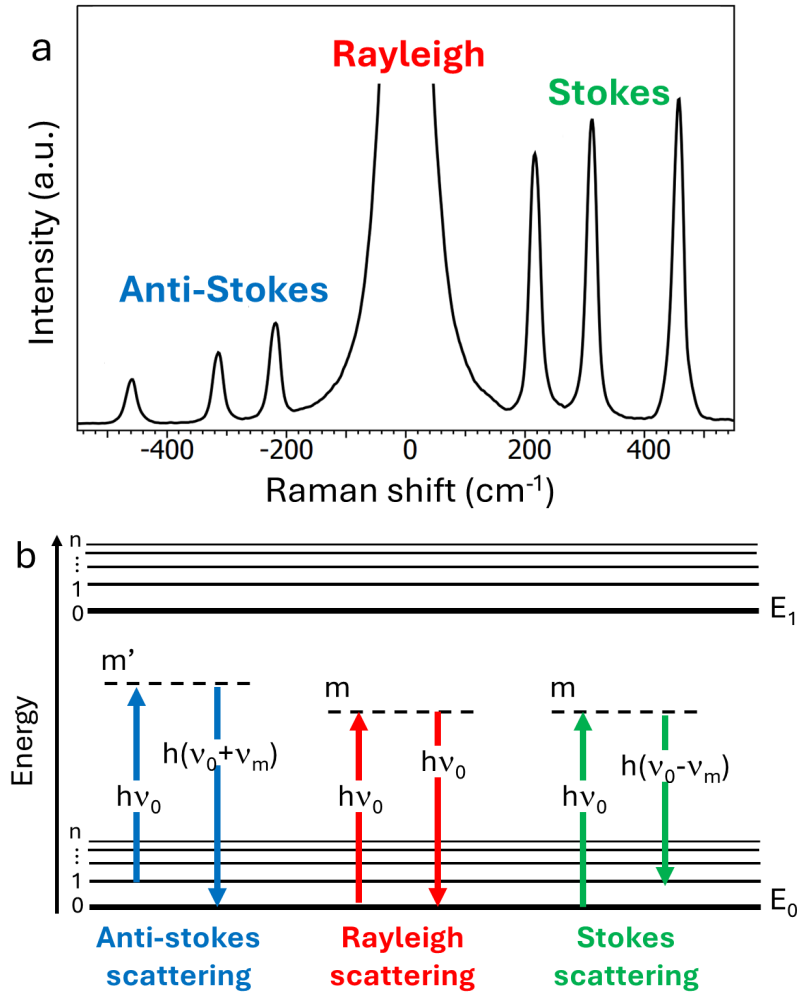
Figure 2.1: *a) Example of a Raman spectrum [92].* *b) Scheme of energy levels involved in Rayleigh, Stokes and Anti-Stokes scattering.*

giving rise to the anti-Stokes line.

Considering that at thermal equilibrium the distribution of the carriers follows the Boltzmann distribution, it is clear that the population of the vibrational state $\nu = 0$ of the ground electronic level prevails compared to that in the vibrational state $\nu = 1$ of the ground electronic level. For this reason the Stokes transitions, that start from the vibration state $\nu = 0$, are more probable than the anti-Stokes and this leads to the difference in the intensity between Stokes and anti-Stokes lines.

2.1.1 Raman Microscopy

Since the 1970s, Raman spectrometers have been coupled with optical microscopes to achieve not only better spectral resolution but also good spatial resolution on the focal plane of the last lens of the microscope [37]. When the Raman spectrometer is coupled with a confocal microscope there is also good resolution along the vertical direction (within the sample), so it is possible to perform cross-sectional sample sections. The

analysis area can be visualized using a coaxial camera aligned with the direction of the incident laser and can be varied from a few to a few hundred square micrometers depending on the used lenses.

2.2 Photoluminescence Spectroscopy

Photoluminescence consists in the emission of light from an excited electronic state of "matter" caused by absorption of opportune electromagnetic radiation. However, photoluminescence is not the only relaxation phenomenon involved between an excited electronic states and the electronic ground state [93, 94]. To have an overview about the possible electronic transitions and the several relaxation phenomena it is useful to introduce the Jablonski diagram, reported in fig.2.2. In this diagram the singlet electronic states are indicated with S_n, where n=0 is the electronic ground state, n=1 is the first excited electronic state... At the same way, with T_n the triplet states are indicated. In each electronic level some of the vibration energy levels are depicted by thin lines. Absorption process involves transitions between singlet electronic states and these transitions occur in a characteristic time of $10^{-15}s$. This value is so short that the displacement of nuclei can be neglected (Franck-Condon principle) during the absorption process. It is worth to note that at room temperature the excited vibrational and electronic states are not significantly populated according to the Boltzmann distribution. Hence, absorption occurs mostly from the lowest vibrational energy states of S_0.

After the absorption process, the possible relaxation processes are:

- Internal conversion, a non-radiative transition between two electronic states with same spin multiplicity ($S_2 \rightarrow S_1$ in fig.2.2) that can be followed by a vibrational relaxation to the lowest vibrational level of the final electronic state, the process occurs in a time-scale of $10^{-13} - 10^{-11}$ s.

- Fluorescence is the transition $S_1 \rightarrow S_0$ accompanied by the emission of photons and its time-scale is related to the lifetime of the S_1 state, before the emission of a photon or a non-radiative decay process, that is in the range $10^{-9} - 10^{-7}$ s. The emission process occurs with the same characteristic time of absorption $10^{-15}s$.

- Intersystem crossing, a non-radiative path that connects isoenergetic vibrational levels belonging to electronic states with different multiplicities, such as from a singlet to a triplet state ($S_1 \rightarrow T_1$ in fig.2.2). This process can be fast enough ($10^{-10} - 10^{-8}$ s) to compete with other relaxation processes from $S_1 \rightarrow S_0$ (fluorescence and internal conversion). In principle, crossing between states of different multiplicity is forbidden but spin–orbit coupling can be so strong to make it possible (for example when there are heavy atoms).
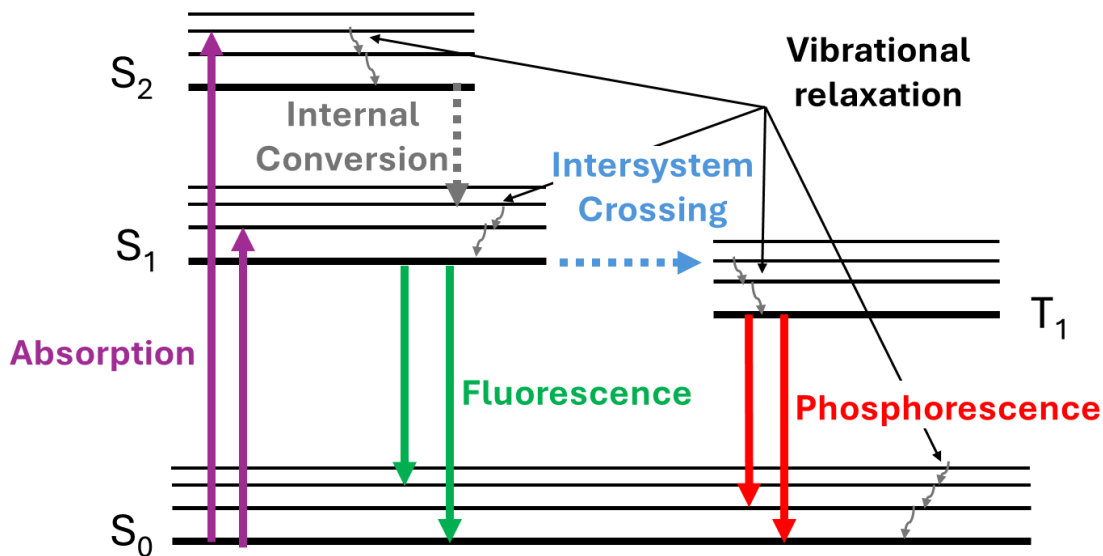
Figure 2.2: *Jablonski diagram of a molecule. Adapted from [93, 94].*

- Phosphorescence, a radiative process from $T_1 \rightarrow S_0$ with a characteristic time of $10^{-6} - 10$ s that occurs after intersystem crossing. This transition is also forbidden. As a consequence, the radiative rate constant is very low, several orders of magnitude smaller than the one of fluorescence.

Lastly, the system can continue the internal conversion from any electronic excited state towards the S_0 state relaxing without light emission, even if this process is less efficient than fluorescence and intersystem crossing. The Jablonski diagram refers to the easy case of a molecule. In more complex situations, non-radiative processes can be due to the presence of dopants, extended or point defects. A general feature of emission spectra is that the peak position is shifted to lower energy respect to the absorption spectrum and it is possible to observe also the vibrational fine structure. The energy shift between absorption and emission peak position is called Stokes shift and is due to all the non-radiative relaxation processes that occur before the emission process. Another general feature of fluorescence in homogeneous systems is that the emission spectrum does not depend on the excitation wavelength because the emission occurs always from the lowest excited state according to Kasha's rule (actually, violations of this rule have been reported).

2.2.1   Time-resolved Photoluminescence Spectroscopy

Important information can be obtained when the system is under pulsed excitation. In fact, when N_0 molecules are excited by pulsed excitation, a non-stationary density of centers N is promoted in the excited states and then can decay to the ground state in a radiative or non-radiative way (neglecting photo-chemical reactions) [93, 94, 95].

The depopulation of the excited state can be described by the following equation:

$$\frac{dN}{dt} = -(k_{rad} + k_{nr})N \tag{2.11}$$

where k_{rad} is the radiative rate constant and k_{nr} is the non-radiative rate constant. The solution is given by:

$$N(t) = N_0 \exp\left(-t/\tau\right) \tag{2.12}$$

where τ is the total lifetime of the excited state defined as:

$$\tau = \frac{1}{k_{rad} + k_{nr}} \tag{2.13}$$

and N_0 is the population of the excited state at the end of the excitation pulse. However, fluorescence is a random process, and very few molecules emit precisely at $t = \tau$. Infact the meaning of lifetime is the average time that a center spends in the excited state prior to return to the ground state. The de-excitation can be observed experimentally by time-resolved photoluminescence spectroscopy (TRPL), measuring the temporal decay of the emitted light. Considering that the intensity of the emitted light, I, is proportional to the density of centers de-excited per unit time (eq.2.12):

$$I(t) = I_0 \exp\left(-t/\tau\right) \tag{2.14}$$

that is an exponential decay law, where I_0 is the intensity of the emission at the end of the excitation pulse. So the lifetime τ indicates the time in which the intensity of the emitted radiation decrease to I_0/e. It is important to underline that single exponential decay is not the only possible law describing the depopulation of the excited state, double exponential and stretched exponential are often observed.

To performe time-resolved measurements it is necessary to collect the emission spectrum at determinate delay time t from the excitation pulse and with a temporal gate Δt, as represented in fig.2.3.
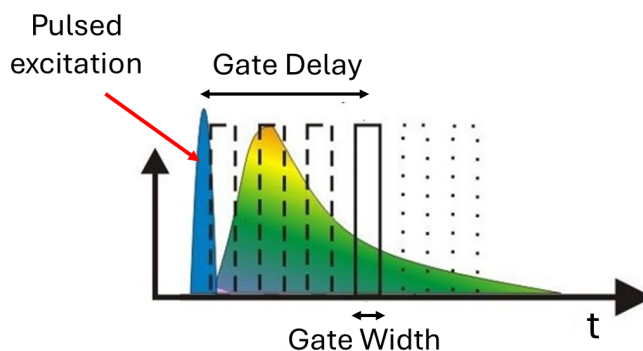

Figure 2.3: *Scheme of a time-resolved photoluminescence spectroscopy measurement, adapted from [96].*

Chapter 3

Materials and Methods

In this chapter a brief description of the studied samples, of the X- and electron irradiations and of the thermal treatments conducted to study the thermal stability of SiC are reported. Furthermore, the experimental setups are described introducing their main parameters.

3.1 Materials

All the SiC materials used in this thesis were provided by STMicroelectronics. They are high purity wafers produced by the chemical vapor deposition (CVD) technique. The substrates are 6 inch 4H-SiC wafer of 350 μm thickness and are grown from three different suppliers. The substrates are named SK, SY and Cree depending on the suppliers. The substrates have been employed to realize epilayers by the CVD method too.

The epitaxial layers were grown with the same condition and features obtaining 12 μm thickness, n-type doping 10^{16}cm^{-3} using Nitrogen, on the SK, SY and Cree substrate, in an Hot-wall horizontal CVD batch reactor able to process three wafers at once, by STMicroelectronics. The growth temperature is in the $1600 - 1700°C$ range under vacuum pressure.

The wafer thickness was measured through interferometry (FT-IR) by STMicroelectronics. Also the doping was measured by STMicroelectronics, by voltage-capacitance analysis with Mercury-based probe to guarantee flat Schottky contact between the probe and the wafer surface. After preliminary characterization of the whole wafer it has been cut in different pieces to obtain many samples to be processed in the experiments.

3.2   Irradiations

In order to evaluate the radiation resistance of the epilayers grown on the SK and SY substrates, the wafers with epilayer were cut in various pieces of typical size of about 1 cm x 1 cm and these new samples have been exposed to radiation at room temperature. Three different sources have been used during these experiments as explained in the following paragraphs.

3.2.1   X-ray irradiations

The x-rays irradiation have been conducted in ambient atmosphere at room temperature with two different x-ray tubes both with a W target. At the LAX Laboratory of the Università degli studi di Palermo (Italy), operating with an anode bias voltage of 28 kV, a dose of 16 $kGy(Si)$ has been deposited. At the Laboratoire Hubert Curien at the University of Jean Monnet of Saint-Étienne (France), operating with an anode bias voltage of 100 kV, a dose of 100 $kGy(SiO_2)$ has been deposited.

3.2.2   Electron irradiations

The electron irradiations have been conducted with the pelletron accelerator SIRIUS at the École polytechnique, Palaiseau (LSI, CEA, CNRS (France)) employing a 2.5 MeV electron beam in vacuum condition and at room temperature depositing a dose in the range of $1 - 100$ $kGy(Si)$.

3.3   Thermal Treatments for the study of Thermal Stability

In chapter 6 the study of the thermal stability of 4H-SiC substrates is reported. In particular, thermal treatments were conducted by STMicroelectronics on wafers substrates in a vertical activator able to process up to 75 x 6" wafers at once placed in a boat. The thermal treatments were conducted at different temperatures (below $2000°C$), always in Argon atmosphere at 50 $mBar$. The process consists of a fast temperature ramp up to the fixed treatment temperature, this temperature was then maintained for few seconds and then the system cooled down naturally to room temperature. After the process, the wafer substrates were cleaned with a water jet to remove possible dust coming from the activator.

Other thermal treatments up to a temperature of 900°C have been carried out after the irradiation experiments in a muffle furnace in ambient atmosphere. In this case the irradiated sample has been inserted in the furnace already heated at the fixed temperature of the treatment and was kept inside the furnace up to the selected
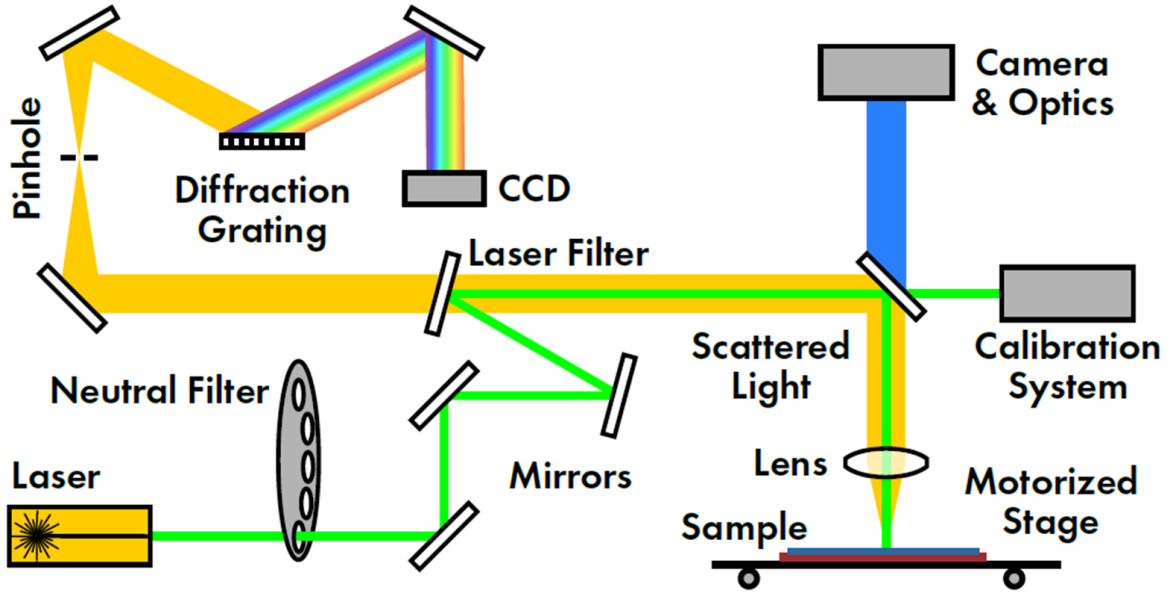
Figure 3.1: *Scheme of the Raman setup [97].*

experiment time. Afterward, the sample was suddenly extracted form the furnace and was naturally cooled to room temperature.

3.4 Methods

3.4.1 μ-Raman

The μ-Raman measurements have been conducted with an Horiba LabRam HR-Evolution Spectrometer coupled to a confocal microscope with a 100x objective, an excitation laser source of 633 $nm(1.96\ eV)$ filtered with a neutral density filter (50%) in order to not affect the samples. The Raman spectra were dispersed on a grating with 600 $lines/mm$. The dimension of the pinhole was fixed at 200 or 50 μm for the measurements conducted respectively on substrates or epitaxial layers. In these conditions, we obtained a spectral resolution of 1 cm^{-1}. The μ-Raman measurements have been carried out with the confocal microscope in back-reflection geometry focusing the laser on the wafer surface. A vertical resolution of $2-3\ \mu m$ was estimated, so the measurements conducted on the epitaxial layers are not influenced by the underneath substrate. All the acquired spectra have been calibrated with respect to the Si peak at 520.7 cm^{-1}.

Fig.3.1 shows the diagram of a typical Raman spectrometer. The laser beam, thanks to a system of mirrors, reaches the sample after being focused on a spot of $1-2\ \mu m$ by the microscope objective. The beam power is appropriately reduced by neutrals density filters. The scattered radiation is collected along the direction opposite to the incident direction (so perpendicular to the sample's surface) by the same objective and is guided toward the spectrometer while the Rayleigh component of the scattering is blocked by

an appropriate filter. After that, the scattered light goes through a pinhole, that allows the confocal measurements by selecting only the portion of light originating from the focal plane of the microscope objective. Finally, the Raman spectrum is obtained through a diffraction grating and acquired by a CCD.

3.4.2 Time Resolved Photoluminescence Spectroscopy

Time-resolved photoluminescence spectroscopy has been conducted with the setup represented in fig.3.2. Essentially, the setup is divided in the excitation unit, the monochromator and the detector.

The excitation unit is a Vibrant OPOTEK tunable laser, that consists of an optical parametric oscillator (OPO) that is pumped by a Q-switched Nd:YAG laser. The Nd:YAG laser provides 5 ns pulses at 1064 nm with a maximum repetition rate of 10 Hz. The active medium of the laser is pumped by an high-power Xenon lamp, and the Q-switch is triggered by a Pockels cell within the laser cavity. The 1064 nm beam passes through a second harmonic generator (SHG), where it is converted to its second harmonic 532 nm, and then through a third harmonic generator (THG), where it is converted to its third harmonic 355 nm. This beam is then directed to the OPO in which a non-linear crystal permits to generate tunable wavelengths. In particular, according to the conservation of energy and momentum, a signal and an idler beams that are perpendicularly polarized are generated. A polarizer is necessary to select the signal $(410 - 710\ nm)$ or the idler $(710 - 2400\ nm)$ beam. Furthermore, UV-modules can be added to the path to duplicate both the signal or idler beam. This enables to extend the tunability range of the excitation beam to the $210 - 410\ nm$ range.

After that, the excitation beam is guided towards the sample. The emitted light is collected by a lens, passes through a slit (that can be changed manually), is directed to the monochromator and finally to the detection system. It is possible to select three different gratings which differ in the blaze wavelength λ_b and in the grooves density. In this thesis all the measurements were conducted with the grating with a $\lambda_b = 300\ nm$ and 150 $grooves/mm$ and with the slit fixed at 250 mm, obtaining a spectral resolution of 5 nm.

The detector is an Intensified CCD camera (PI-MAX Princeton Instruments) that is synchronized to the excitation laser by a programmable timing generator (PTG) which is triggered by the laser. This system allows to enable and disable the CCD acquisition in a controlled way to perform the time-resolved measurement. In particular, it is necessary to record the emission spectrum in a fixed temporal window (Gate width) after a specific delay time (Gate delay) from the excitation pulse, as represented in fig.2.3. To reconstruct the whole kinetics of the decaying emission a series of measurements is needed with variable Gate delays from the laser pulse.
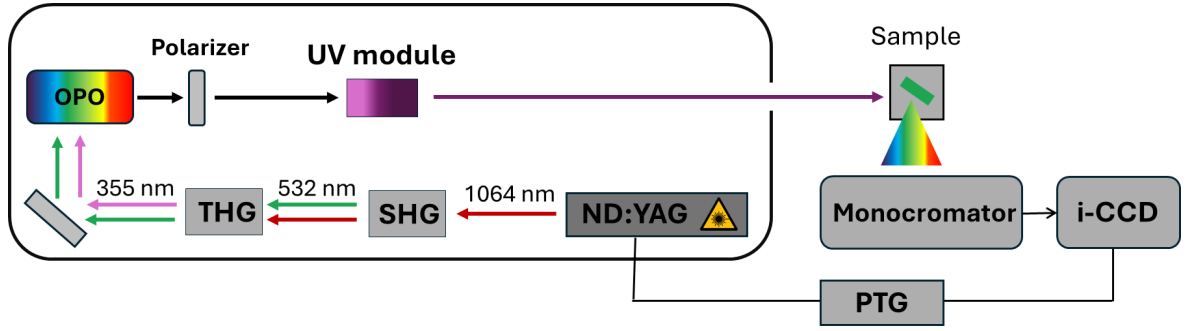
Figure 3.2: *Scheme of time-resolved photoluminescence setup.*

3.4.3 Steady-State Absorption

Steady-state absorption measurements have been carried out with a JASCO V-530 double beam spectrophotometer equipped with two light sources. The first is a deuterium lamp for UV range 190-340 nm, the second one is an halogen lamp for VIS range 330-1100 nm. The light is guided to a monochromator with a 1200 grooves/mm grating. After that, the monochromatic beam is split in two. One beam reaches the sample and the other one is used as a reference. The two beams are then detected by a photomultiplier. The instrument output is the optical density (OD) defined as:

$$OD = log_{10}\frac{I_0}{I} \tag{3.1}$$

where I is the intensity of the transmitted light by the sample and I_0 is the intensity of the reference beam. The OD is recorded as a function of excitation wavelength over the selected spectral range.

3.4.4 Steady-state Photoluminescence

Steady-state photoluminescence (PL) measurements have been conducted using a JASCO FP-6500 spectrofluorometer, using as excitation source a 150 W Xenon discharge lamp operating in the 220-750 nm range. The excitation light is dispersed through a monochromator with a 1800 grooves/mm grating, furthermore, it is possible to select the dimension of the bandwidth allowing to select more or less a monochromatic excitation. The beam is focused on the sample by a lens, collected by another one in a typical 90° geometry and directed toward a second monochromator with the same features of the excitation one. At this point, the dispersed emission light is detected by a photomultiplier. The presence of two monochromators allow the acquisition of photoluminescence (PL) spectra, fixing the excitation wavelength and by scanning the emission wavelength, and photoluminescence excitation (PLE) spectra, scanning the excitation wavelength with a fixed emission wavelength. Furthermore, both monochromators have slits (that can be manipulated) to improve the resolution of both excitation

and emission spectra.

Chapter 4

Samples Characterizations

As discussed in chapter 1, in order to produce a 4H-SiC semiconductor device the first step is to grow an epitaxial layer (of 4H-SiC) with determined thickness and doping on top of a degenerately doped 4H-SiC substrate [24, 98]. The features of SiC-based devices are influenced by the presence of extended defects, point defects and impurities, that can be introduced during each step of the growth [99, 100, 101, 102, 103, 104, 105]. In this context, to reach the full potential of the SiC-based devices it is fundamental to grow highly uniform and low defective epitaxial layers. It is obvious that an inhomogeneous material is characterized by nonuniform properties that implies poor quality epilayer or the manufacturing of inhomogeneous devices (typically more than one hundred devices are created from a single wafer).

In the field of semiconductors, the most used techniques to prove the quality of the epilayers are electrical characterizations that require the growth of fixed metal contacts with the sample (as Hall or resistivity measurements) [46, 106, 107]. As a consequence, such characterizations can ruin the material or made it unusable. Furthermore, electrical techniques cannot be used online in the production process to monitor the quality and the properties of the SiC devices during their growth. It emerges the necessity to identify non-invasive characterization techniques able to find differences among wafers, to disentangle features of the substrate from those of epilayer and, least but not last, to check the material features during the different steps of the devices growth.

In this chapter the basic characterizations conducted on epitaxial layer of 4H-SiC grown on two different kinds of substrates of 4H-SiC (SK and SY) are reported. In particular, the non-invasive characterization techniques of micro-Raman, steady-state absorption, steady-state and time-resolved photoluminescence spectroscopy have been used in this thesis to compare the properties of substrates and of the epilayers.
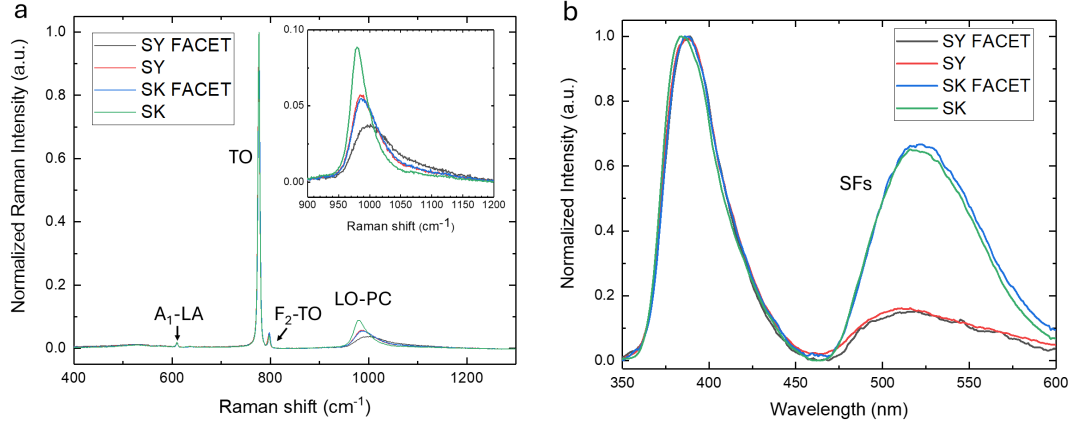
Figure 4.1: *a) Normalized Raman spectra of wafer substrates; in the inset is evidenced the range 900-1200 cm^{-1}, adapted from [108]. b) Photoluminescence spectra with excitation wavelength of 325 nm of wafer substrates normalized to the intensity of the excitonic band at 390 nm.*

4.1 Substrates

As reported in the previous chapter, STMicroelectronics supplied two 6 inch diameter wafer substrates of 4H-SiC, named SK and SY, that have been produced by two different factories but that have the same thickness 350 μm and the same Nitrogen doping level 10^{19}cm^{-3}. These values were declared by the producers. By an optical analysis, SK and SY present a darker area called facet, that is an area more doped than the surrounding wafer substrate. Actually, the origin of the facet is associated to the growth of the substrate itself and can have different oval or circular shapes and dimension.

4.1.1 μ-Raman Spectroscopy

Raman spectroscopy has been used to evaluate the structural and doping properties of the studied samples. In fig.4.1a, the micro-Raman spectra of SK and SY substrates normalized to the intensity of the TO band (around 780 cm^{-1}) are reported. These spectra correspond to the typical one of 4H-SiC polytype [98, 109]. The main TO and LO (around 980 cm^{-1}) bands and the minor A$_1$-LA (around 610 cm^{-1}) and F$_2$-TO (around 800 cm^{-1}) bands are present and are indicated in fig.4.1a. Furthermore, there is no evidence of stress that can cause distortion or shift of the Raman peaks. In general, in a polar semiconductor such as SiC, the free carriers interact with the LO phonons giving rise to the LOPC (longitudinal optical phonon-plasmon coupled) mode (around 980 cm^{-1}). As a consequence, the LO mode depends strictly on the carrier density (in the monitored region). In particular, when the carrier density (or doping) increases, the LO peak shifts toward higher Raman shift values with peak broadening [98, 109].

44

By comparing the LOPC mode in the spectra reported in fig.4.1a it is clear that the doping of the substrates is quite different. The peak position, estimated by a Gaussian fit, of the LOPC band of SY is $988.5 \pm 0.6 cm^{-1}$, for SY facet it is $1002.1 \pm 0.9 cm^{-1}$, for SK is $981.5 \pm 0.4 cm^{-1}$ and for SK facet it is $989.5 \pm 0.7 cm^{-1}$. The carrier density can be calculated by properly fitting the LOPC band but only for highly doped n-type SiC. This fitting procedure is complex and out of the scope of this thesis but a detailed explanation can be found in the works [109, 110, 111]. The comparison with literature data of the peak position of the LOPC is fair enough to state that doping is minimum for SK, is similar for SK facet and SY, and is maximum for SY facet. Furthermore, the frequency of vibration enables to state that the doping level is compatible with the declaration of the supplier companies that is larger than $10^{17} cm^{-3}$. The peak position of the TO band (estimated by a Gaussian fit and used as reference) is $776.5 \pm 0.5 cm^{-1}$ and is the same for all the samples.

4.1.2 Steady-State Absorption

Absorption spectra in the visible-UV range have been employed to deepen the spectroscopic properties of the substrate wafers. Fig.4.2b reports the absorption spectrum of SY wafer and fig.4.3b the spectrum of SK wafer. Measurements were collected from the center of the wafer (red dashed line) and from the center of the facet (black dashed line). In both cases, it is possible observe two different O.D. levels depending on whether the measurements were carried out on the facet regions or not. The band around 2.7 eV has been attributed to inter-conduction band transitions [112, 113, 114]. On the facet of both SK and SY substrates this band is broader and the O.D. value is higher respect to the rest of the wafer, suggesting that in the inter-conduction band transitions the levels introduced by Nitrogen doping are involved and that these levels have small differences in the different regions of the wafers.

4.1.3 Steady-State Photoluminescence

Further investigation of the electronic state of the wafer has been carried out by photoluminescence spectroscopy. In fig.4.1b, the photoluminescence spectra under excitation with a 325 nm (3.8 eV) wavelength of wafer substrates, both facet and out of facet, normalized to the amplitude of the band at 390 nm are reported. This latter band can be associated to the excitonic radiative recombination [115, 116]. The broad band around 520 nm can be attributed to the recombination processes in correspondence of the family of defects known as stacking faults (SFs) [50, 51, 117, 118, 119]. As discussed in chapter 1, the SFs are one of the most common extended defects in SiC due to their low formation energy and, because of the occurrence of many SiC polytypes, multiple types of SFs can be present simultaneously. Most of the SFs have a characteristic peak
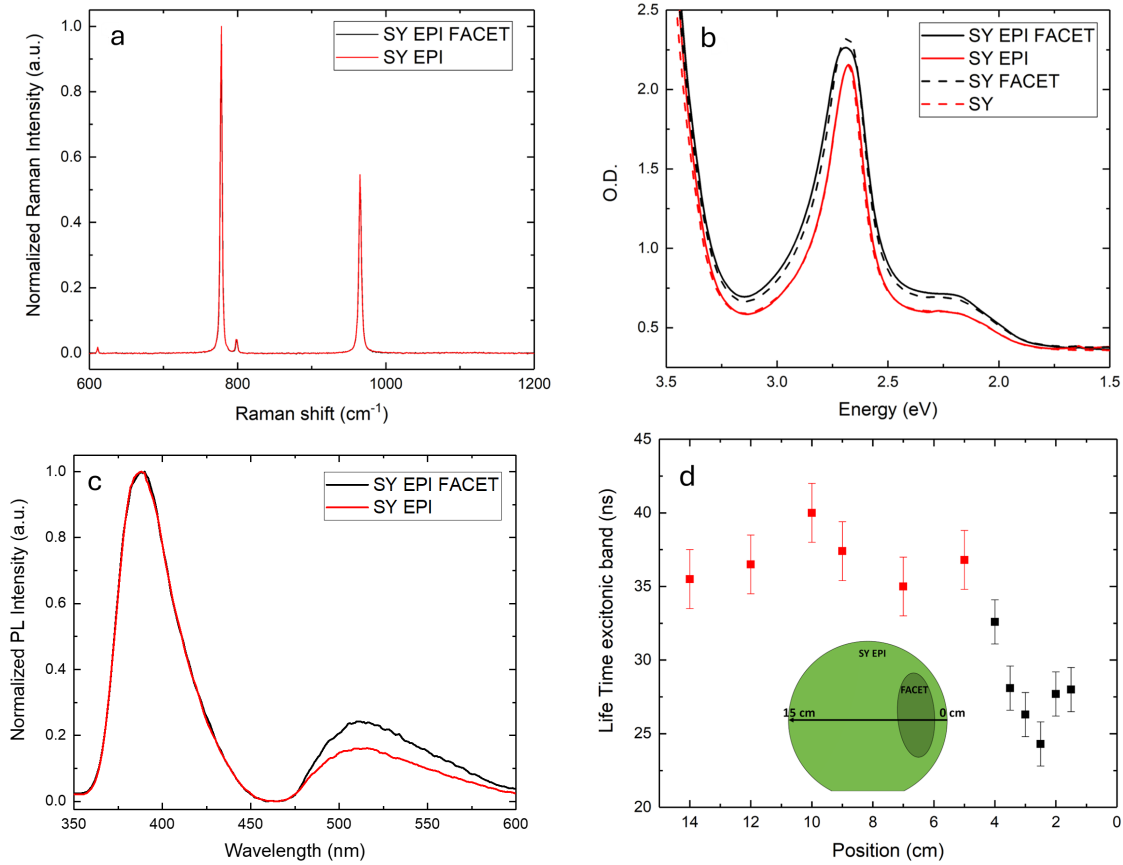
Figure 4.2: *a) Normalized Raman spectra of SY EPI wafer conducted in the center (in red) and in the center of the facet (in black) [108]. b) Absorption spectra in the UV-Visible range 1.5-3.5 eV conducted in the center of the SY EPI wafer (in red) and in the center of the facet (in black), in the center of SY substrate (dashed red line) and in the facet (dashed black line) [108]. c) Photoluminescence spectra with excitation wavelength of 325 nm (3.8 eV) of SY EPI wafer normalized to the intensity of the excitonic band. d) Lifetime of excitonic band under excitation at 266 nm (4.66 eV) as a function of the position along the diameter of the SY EPI wafer [108].*

emission, in particular, in literature SFs emission in the 420-550 nm range have been reported in good agreement with the observed emission [50, 51, 117, 118, 119].

Normalizing with respect to the excitonic band enables to qualitatively discern which of the SK and SY substrates is characterized by a higher quantity of defects (SFs). In this case, within the same wafer (facet and out of facet) the amount of SFs is the same and, furthermore, the SFs related band of SK wafer has an intensity that is four times higher than the one of SY wafer suggesting that SK wafer substrate contains more SFs than SY wafer substrate.

4.2 Epitaxial Layers

Starting from the same SK and SY substrates reported in the previous paragraph, 12 μm of epitaxial 4H-SiC were grown utilizing always the same growth conditions
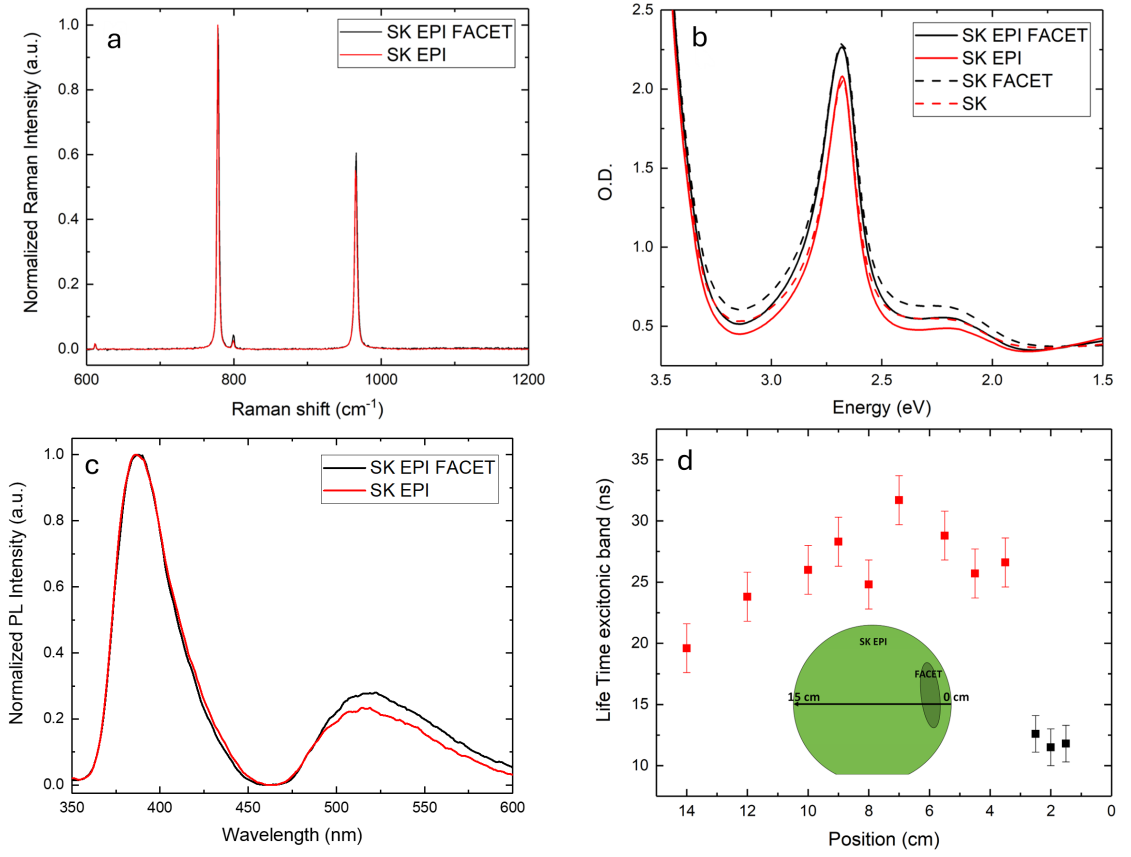
Figure 4.3: *a) Normalized Raman spectra of SK EPI wafer conducted in the center (in red) and in the center of the facet (in black) [108].* ***b)*** *Absorption spectra in the UV-Visible range 1.5-3.5 eV conducted in the center of the SK EPI wafer (in red) and in the center of the facet (in black), in the center of SK substrate (dashed red line) and in the facet (dashed black line) [108].* ***c)*** *Photoluminescence spectra with excitation wavelength of 325 nm (3.8 eV) of SK EPI wafer normalized to the intensity of the excitonic band.* ***d)*** *Lifetime of excitonic band under excitation at 4.66 eV as a function of the position along the diameter of the SK EPI wafer [108].*

by STMicroelectronics. The doping of the epilayer is about 10^{16}cm^{-3} (n-type realized using Nitrogen), three orders of magnitude lower than the substrates, and it was measured by mercury-probe measurements by STMicroelectronics. The wafers substrate+epitaxial layer are named SY EPI and SK EPI, in the following. A scheme of both SY EPI and SK EPI wafers is reported in fig.4.4. It is possible to observe the presence of facets in both cases, highlighted by darker-colored regions. The SY EPI wafer has an oval shaped facet of 3.5 cm x 8 cm and SK EPI wafer has an oval shaped facet of 2 cm x 5 cm. By using a diamond tip, a slice along the diameter of both wafers has been cut and then it was divided in 24 pieces with dimensions about (5x5 mm^2) as shown in fig.4.4. Each piece is named 'SY EPI#n' ('SK EPI#n'), or 'SY EPI#n (F)' ('SK EPI#n (F)') in correspondence of the facet, where 'n' refers to an incremental distance from the edge of the wafer closest to the facet. A spectroscopic characterization has been carried out for the wafers substrate+epitaxial layers to obtain a comparison with the native material and to highlight their properties before any further step in
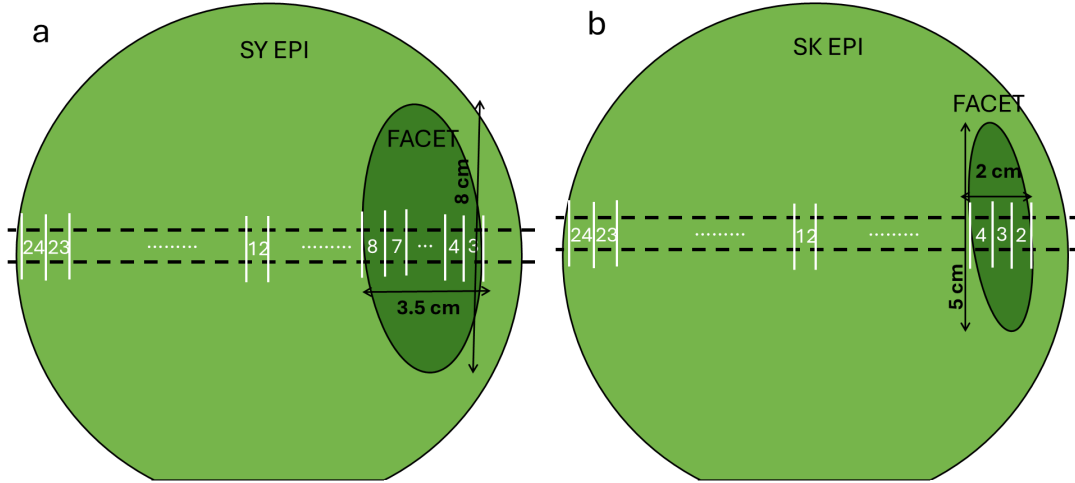
Figure 4.4: *Graphic representation of SY EPI wafer **(a)** and SK EPI wafer **(b)** adapted from [108]. The facets are represented by a darker region and the dashed lines represent the region used to cut samples, numbered in increasing sequence depending on the distance from the facet.*

view of devices realization.

4.2.1 μ-Raman Spectroscopy

In fig.4.2a and 4.3a, the micro-Raman spectra acquired on the SY EPI and SK EPI wafers in the normal and in the facet region are reported. In this case the recorded spectra are very similar, the peak position of the TO band is $776.3\pm0.5cm^{-1}$ and that of LO (LOPC) band is $963.5\pm0.5cm^{-1}$. According to literature, the LO Raman peak does not change position and shape for doping levels equal or lower than $10^{16}cm^{-3}$ [111], that is the estimated doping value by STMicroelectronics using the mercury probe technique. In this case, the Raman characterization enable to verify that the epilayer doping is within the expected concentration. The micro-Raman characterization was carried out along the whole SY EPI and SK EPI wafers diameter investigating the LOPC band at $963.5cm^{-1}$. It is found that the band position and shape is unchanged in all the investigated positions leading to the conclusion that the doping all over the epilayers (including the part grown above the facet) is within the range of the expected concentration.

z-profile

Thanks to the confocal microscope coupled with the Raman spectrometer it is possible to record micro-Raman spectra underneath the samples surface (focusing on the surface and then moving the z-motor inside the sample). Acquiring micro-Raman spectra at different z positions it is possible to produce a "vetical scan" and get several information. For example, in the case of the wafer with epitaxial layers it is possible to study the
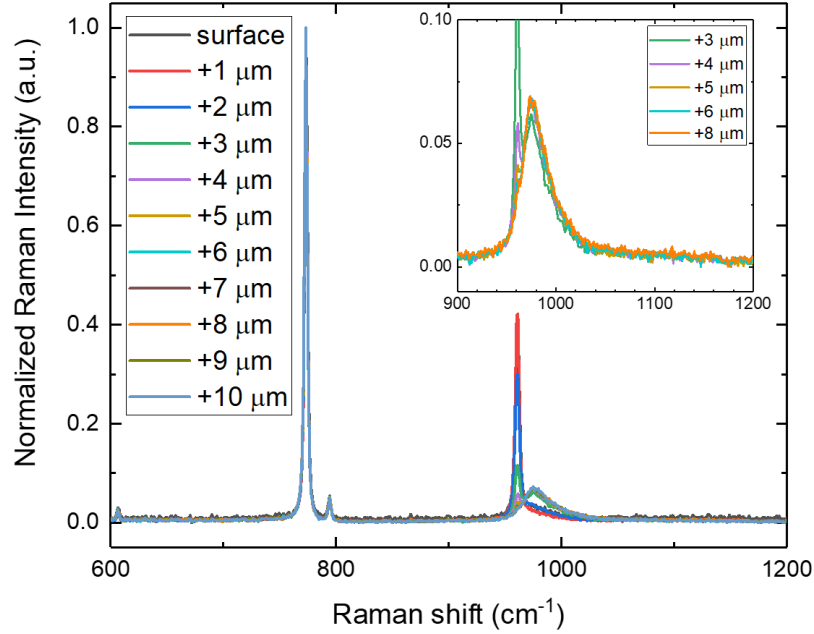
Figure 4.5: *Normalized micro-Raman measurements conducted on SY EPI wafer at different z positions below the sample surface. In the inset is reported the detail of the LOPC band at different depths.*

structure and the quality of the epilayer for its whole thickness and to monitor the quality and the amount of doping of the underneath substrate even after the epitaxial growth.

In fig.4.5 the normalized (with respect to the TO band) Raman spectra of the SY EPI wafer, acquired from the surface of the epilayer toward the substrate with steps of 1 μm, are reported. It is possible to observe that the shape of the LOPC band at $963.5 cm^{-1}$ changes gradually going from the surface to the substrate. In particular, the surface spectrum is characterized by a sharp band at low Raman shift, in accordance to a low doping value, whereas moving below the surface a broader peak is superimposed at larger Raman shift and at about 6 μm in depth just a broad peak is found in agreement with the measurements conducted on the naked SY substrate and in accordance to a large doping. These analysis enable to trust the Raman measurements carried out in the wafers substrate+epitaxial layer and to attribute the observed features to the epilayer or to the substrate, selectively.

4.2.2   Steady-State Absorption

In fig.4.2b and fig.4.3b, in addition to the absorption spectra of the SY and SK substrates discussed before, the absorption spectra of SY EPI and SK EPI wafers in the facet (in black) and out of the facet (in red) are also shown. The peak position and the shape of the spectra acquired in the corresponding positions between a wafer substrate and the wafer with epilayer are the same within the experimental error (verified by a

Gaussian fit). This remark is not surprising because of the nature of a steady-state absorption measurements, that are transmission measurements and as a consequence the most of the signal is due to the substrate that is thirty times thicker than the epitaxial layer.

4.2.3 Steady-State Photoluminescence

In fig.4.2c and fig.4.3c, the photoluminescence spectra under excitation with a 325 nm wavelength of wafer substrates, both facet and out of facet, normalized to the intensity of the excitonic band at 390 nm are reported. It is possible to observe by comparison with fig.4.1b, that the shape of the emission spectra of SY EPI and SK EPI wafer is very similar to the shape of the emission spectra of the respective kind of substrates. The only exception is in the amount of SFs defects. In particular, considering the relative intensity of the SFs emission band, around 520 nm, it is possible to state that the relative amount of SFs is minimum for SY EPI, is maximum for SK EPI FACET and is similar for SK EPI and SY EPI FACET. Within the same wafer, the SFs concentration seems to be higher on the facet, so it is possible that the substrate properties of the facet encourage the SFs formation in the epilayer.

4.2.4 Time-resolved Photoluminescence Spectroscopy
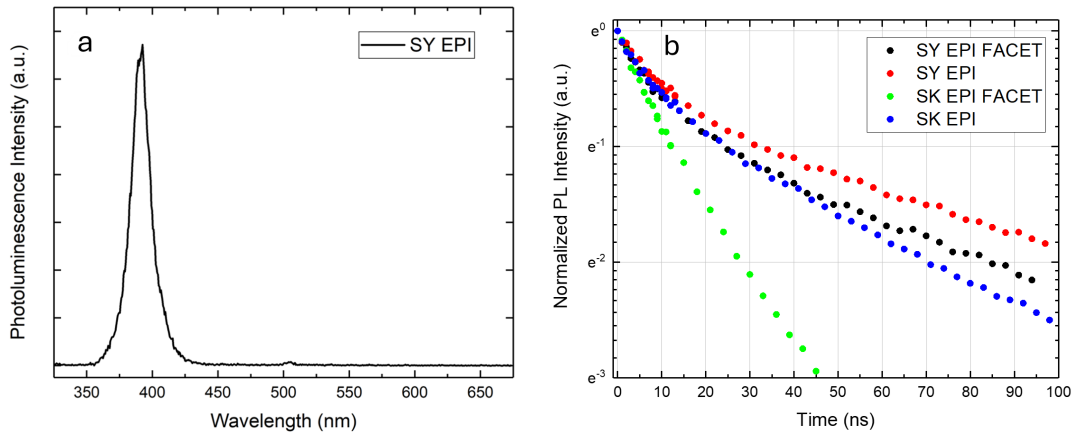
Figure 4.6: *a) Photoluminescence spectrum of SY EPI wafer under excitation at 266 nm (4.66 eV) [108]. b) Normalized photoluminescence decay under excitation at 266 nm (4.66 eV) of excitonic band of one sample per SY EPI facet, SY EPI, SK EPI facet and SK EPI [108].*

The quality of epitaxial growth can be evaluated basing on several parameters. In addition to doping homogeneity, the carrier lifetime is crucial, as it can be affected by crystal imperfections, deep levels and defects. In this thesis, the carrier lifetime was studied monitoring the recombination of the excitonic band at 390 nm under excitation at 266 nm (around 4.66 eV) by time-resolved photoluminescence spectroscopy (TRPL).

The penetration depth at the used excitation wavelength is about 0.6 μm, so the excitonic couple is generated within the epitaxial layer. The given lifetime values are determined as the time needed to the intensity of the excitonic recombination band to decay to $1/e$ of its value after 6 ns from the excitation laser pulse maximum. The associated errors refer to the experimental uncertainty due to the repeatability of measurements.

In figure 4.6a, the photoluminescence spectrum of one spot of the SY EPI sample is reported as example. The band at 391.2±0.1 nm (around 3.12 eV), determined by Lorentzian fit, is related to the recombination of the excitonic couple and has a FWHM of 15.7±0.2 nm. In both SY EPI and SK EPI wafer (facet and out of facet), the position and the shape of the excitonic band is the same. The Lorentzian shape of the excitonic band indicates that the exciton is delocalized and have good mobility (this is not surprising because exciton mobility is related to the translational symmetry of the lattice) [120, 121]. According to the model of exciton-phonon interaction in solids, developed by Toyozawa [122], when exciton-phonon coupling is taken into account, the resulting line shape is given by the competition between the mobile nature of excitons and their tendency to localize in the lattice sites due to the phonon-coupling. In particular, Lorentzian line shapes are predicted when mobility effects prevail over energy fluctuations, in the opposite case the expected line shape is a Gaussian [122].

The normalized photoluminescence decay of the excitonic band of SY EPI facet, SY EPI, SK EPI facet and SK EPI is shown in figure 4.6b. Each point indicates the area of the excitonic band at different time delays normalized to the area of the excitonic band of the first acquisition (6 ns after the laser pulse). The lifetime values are in the 10-40 ns range and are in agreement with data reported in literature for analogous epilayer thickness [123]. The lifetime value of the excitonic band in different positions along the diameter of SY EPI wafer is reported in fig.4.2d. Two different distributions of lifetime values, depending if the measurements were acquired on the facet (black points) or not, are evident. Specifically, the lifetime value in the facet area is shorter respect to the rest of the wafer. This can be explained considering that the exciton recombines in the levels introduced by Nitrogen doping at the substrate interface which has higher doping on the facet area, as shown in fig.4.1a where it is highlighted that the doping of the facet is larger than the normal substrate. Further to this, it is possible to notice that along the diameter there are some variations within the distributions of lifetime. This enables to have local information about the distribution of recombination centers and about the epitaxial growth quality, because the longer the lifetime of the charge carriers, the higher is the quality of the epitaxial layers [124].

The same observations and considerations are valid for SK EPI wafer. Lifetime values in different positions along the diameter of SK EPI wafer are reported in fig.4.3d. Despite the lower doping level of the SK substrate, the lifetime values in the SK EPI wafer are shorter compared to the ones of SY EPI. This indicates a higher presence

of defects that promote excitonic recombination in the SK EPI wafer respect to SY EPI. This finding is substantiated by the photoluminescence measurements reported in fig.4.2c and fig.4.3c where it is shown that SK EPI has more stacking faults than SY EPI. Basing on this, it is possible to state that the defects present in the epitaxial layer and at the interface have a significant role in the excitonic couple recombination processes.

In light of devices manufacturing with same characteristics, the recombination centers should be uniformly distributed and time-resolved photoluminescence spectroscopy can be worthwhile to probe the quality of epitaxial growth and the distribution of recombination centers.

4.3 Conclusion

In this chapter a characterization via non-invasive characterization techniques of two different kinds of substrates and the relative epitaxial layers of 4H-SiC grown on them has been discussed. By micro-Raman measurements, it has been shown that the doping of the substrates is not uniform, in particular it is higher on the facet area. On the contrary, epitaxial layer doping is within the expected range on the whole wafers epitaxial layer. Exploiting the z-resolution of the confocal microscope of the micro-Raman set-up, it has been also possible to study the homogeneity of the layers of substrate and of epitaxial layers after this latter growth.

Steady-state photoluminescence measurements allowed to know qualitatively the difference in the SFs amount of different wafers (both substrates and epitaxial layers) thanks to the comparison of the relative intensity of emission spectra normalized to the intensity of the excitonic band.

The monitoring of the decay time of the exciton recombination band conducted with time-resolved photoluminescence spectroscopy is an interesting way to probe the uniformity and the quality of epitaxial layer. The differences in lifetime values between facet and out of facet of the same wafer, and the fact that to higher doping (SY facet) is not directly associated a shorter lifetime value, enabled to understand that, in the studied epitaxial wafers, the exciton recombination processes involved both levels introduced by doping at the interface with the substrates and levels related to defects (not only SFs but also other extended defects, point defects and impurities) that are not distributed uniformly on the epitaxial layer as well as at the interface. This finding is of large importance in the qualification of epitaxial layers in order to evaluate their electronic quality and processes before to continue in the growth of devices.

Chapter 5

Effects of Radiations on 4H-SiC Epitaxial Layers

Today the major part of devices used in harsh environments are dominated by Si-based technology that enables to work at temperatures up to about 250°C and radiation levels in the range of Gy (1 krad = 10 Gy) [125, 126, 127, 128]. Research is exploring new materials and technologies that can reliably work in harsh environments, and as discussed in chapter 1, SiC is a material suitable to realize devices for harsh environments applications thanks to its superior properties compared to Si (view table 1.1), in particular, the wide bandgap, the thermal conductivity, the chemical inertness, the mechanical strength and the radiation resistance due to the large threshold energy for the defects formation (30-35 eV). The harsh environments are characterized by extreme temperature, wide temperature working range, high or low pressure, high levels of radiation and ionizing radiations, presence of chemicals and corrosive substances, vibrations, etc. In this context SiC devices can find applications in several fields (some are illustrated in fig.5.1) including space electronics, nuclear power facilities, the management of nuclear waste, nuclear radiation detectors, UV photo-sensors, as well as X-ray and charged particle detectors [70, 71, 72, 73, 129, 130, 131, 132, 133, 134, 135]. It is important to consider that the characteristics and the performance of SiC-based devices, but in general for all devices, can be altered by the presence of impurities, extended and point defects that can be intristic or caused by ionizing radiations [99, 100, 101, 102, 103].

It is not surprising that in recent years, the study of the effects of ionizing radiations on SiC-devices has increased, delving into how ionizing radiations can affect the structure, the transport properties and the formation of defects. Generally, the irradiation effects are studied directly on SiC devices by electrical characterization techniques [33, 136, 137, 138, 139, 140, 141]. But, this implies that some effects could be related to the device production and not to the materials features themselves. Most of all, the growth of epitaxial layer is fundamental for the final device and differences in production steps may have effects on this very thin layer also in connection to its radiation
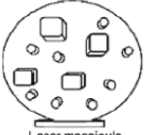
	Dose rate: $<1\,\mathrm{Gy\,s^{-1}}$ Dose: 0.01 to 50 Gy T range: RT	Laser megajoule	Dose rate: $>1\,\mathrm{MGy\,s^{-1}}$ Dose: $<1\,\mathrm{kGy}$ T range: RT
	Dose rate: 10^{-5} to 10^{-3} $\mathrm{Gy\,h^{-1}}$ Dose: $<10\,\mathrm{kGy}$ T range: -200 to $300\,^{\circ}\mathrm{C}$	CERN Large Hadron Collider	Dose rate: $<0.1\,\mathrm{Gy\,h^{-1}}$ Dose: $<100\,\mathrm{kGy}$ T range: RT
Waste	Dose rate: $<10\,\mathrm{Gy\,s^{-1}}$ Dose: $<10\,\mathrm{MGy}$ T range: RT to $90\,^{\circ}\mathrm{C}$		Dose rate: $10^{15}\,\mathrm{n\,cm^{-2}\,s^{-1}}$, $<10^{15}\,\mathrm{n\,cm^{-2}\,s^{-1}}$ Dose: $>\mathrm{GGy}$, $10^{20}\,\mathrm{n\,cm^{-2}}$ T range: RT to $800\,^{\circ}\mathrm{C}$

Figure 5.1: *Dose and temperature range for different harsh environments [142].*

vulnerability. Furthermore, it is imperative to remember that the substrate quality as well could affect the epitaxial layer growth, and as a consequence, it is needed to disentangle the effects of irradiations on the substrate from those on the epilayer.

In this chapter the effects of different radiations, electrons and photons from two X-rays sources, described in chapter 3, on n-type 4H-SiC epitaxial layer are studied by the non-invasive characterization techniques micro-Raman, steady-state absorption, steady-state and time resolved photoluminescence spectroscopy. Furthermore, the recovery properties of 4H-SiC under the influence of thermal treatments in air are also deepened. The basic idea of this study is to underline the 4H-SiC, without any device fabrications, vulnerabilities. This aspect is useful to understand the effects of radiations related to the structure of the material itself. The chapter starts with a brief introduction on the radiation-matter interaction processes relevant for the comprehension of defects generation.

5.1 Ionizing Radiations

The term "ionizing radiation" refers to particles and photons that have enough energy to ionize or displace atoms of a material [143, 144]. There are three main groups of ionizing radiation: charged particles (electrons, protons, alpha particles, heavy ions..), photons (gamma rays, X-rays and part of UV-rays) and neutrons. The interaction between ionizing radiation and the material depends on several factors of the incident particles such as mass, charge state and kinetic energy, and factors of the target material such as atomic mass, density, etc.. The interaction of energetic particles with matter often results in secondary effects (particles) that produce new interactions, making it hard to separate their effects. The main interaction mechanisms between the ionizing radiation and matter are now briefly listed [143, 144].

Photons are particles without charge and mass that interact with matter in three ways depending on the energy: photoelectric effect, Compton scattering and pair production. In the *photoelectric effect*t the energy of the photon is completely transferred to the material, resulting in the ejection of a free electron with kinetic energy equal to the difference between the energy of the incident phonon and the binding energy of the electron. This leads to the production of vacancies, electron-hole pairs and secondary effects. Photoelectric effect prevails at low photon energies and in target material with higher Z (atomic number). In silicon this effects is dominant for photon energies below 50 keV [143, 144]. The *Compton scattering* takes place when the photon energy is higher than the binding energy of the electron of the material. A part of the incident photon momentum and energy are transferred to an electron (that becomes free with a certain kinetic energy) and the photon is scattered with a lower energy. This is a medium-energy process that in silicon is dominant in the 50 keV-20MeV. The *pair production* consists in the generation of a proton-electron pair after the complete absorption of a high photon energy by the target material. In silicon this process dominates at photons energies higher than 20 MeV.

The interaction of charged particles with matter depends on the mass, the energy and the nature of the charged particle and also on the properties of the target material [143, 144]. When penetrating through a material, the charged particles are primarily subjected to coulomb interactions with the electrons of the target material losing gradually their kinetic energy. At low energy, the collisions are elastic and the effect of the interaction consists in the excitation or ionization of the system. At higher energy collisions can lead to the displacement of target atoms inducing a permanent damage in the structure of the target material.

The neutrons interactions with matter are relatively weaker compared to other ionizing radiations [143, 144]. In particular, this process involves elastic and inelasting scattering and transmutation (capture of the incident neutron by the target nucleus with consequent emission of another particle).

5.1.1 Effect of Ionizing Radiations on Devices

In general, the radiation effects on the devices can be distinguished into displacement damage and ionization including the generation of vacancies, interstitials and related defects. In particular, a displacement damage takes place when an impinging charged particle undergoes elastic collision with the target material and it is able to move an atom away from its lattice position. The defects induced by ionizing radiations introduce energy levels in the bandgap modifying the electrical and optical properties of the matter and so the lifetime of the carriers [99, 100, 101, 102, 103]. In fig.5.2 the ionizing radiation effects on matter are schematized. In particular it is possible to notice that charged particles can give rise to both ionization damages and displacement
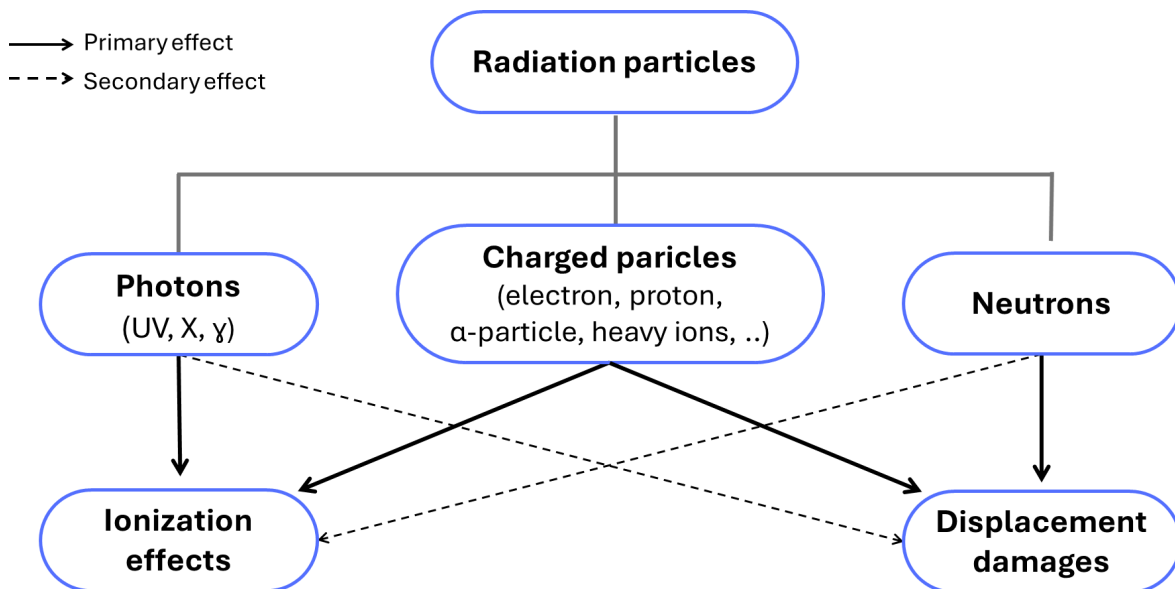
Figure 5.2: *Scheme of main effects of radiation particles.*

damages. Photons produce as primary effects (solid line in fig.5.2) ionization effects while the neutrons primary effect involves displacement damage. It is worth to note, that high energy photons may also produce displacement damage as secondary effect (dashed line in fig.5.2). Furthermore, the secondary effects of neutrons (production of secondary particles) can produce both ionization damage and displacement damage.

5.2 Preliminary Characterization

Five samples of the facet and five out of facet of both SY EPI and SK EPI wafers have been selected to be treated with electrons beam and x-rays as described in section 3.2. All the epitaxial layers have been grown by the same process. In particular, six samples per wafer (three from the facet and three out of the facet) have been irradiated with an electron beam depositing a dose in the range $1 - 100\ kGy(Si)$, two samples per wafer (one from the facet and one out of facet) have been irradiated with two different x-ray tubes depositing a dose of $16\ kGy(Si)$ and $100k\ Gy(SiO_2)$. In all cases the penetration depth of the employed radiation exceeds the thickness of the epitaxial layer.

For convenience, to evaluate the effects of the ionizing radiation a summary of the preliminary characterizations conducted on the not irradiated samples is shown in fig.5.3. The interpretations of the measurements is extensively discussed in chapter 4. In summary, from micro-Raman spectra registered on SY and SK substrate (fig.5.3a) it is evident that there are differences in doping values (evidenced by the LOPC band around 980 cm^{-1}) between the two wafers substrates and in the same wafer substrate there are differences between the facet and the rest of the wafer itself. In particular, doping is highest for SY facet, it is similar for SY and for SK facet and it is minimum for SK. On the contrary, the doping all over the epitaxial (EPI) wafers (fig.5.3b),
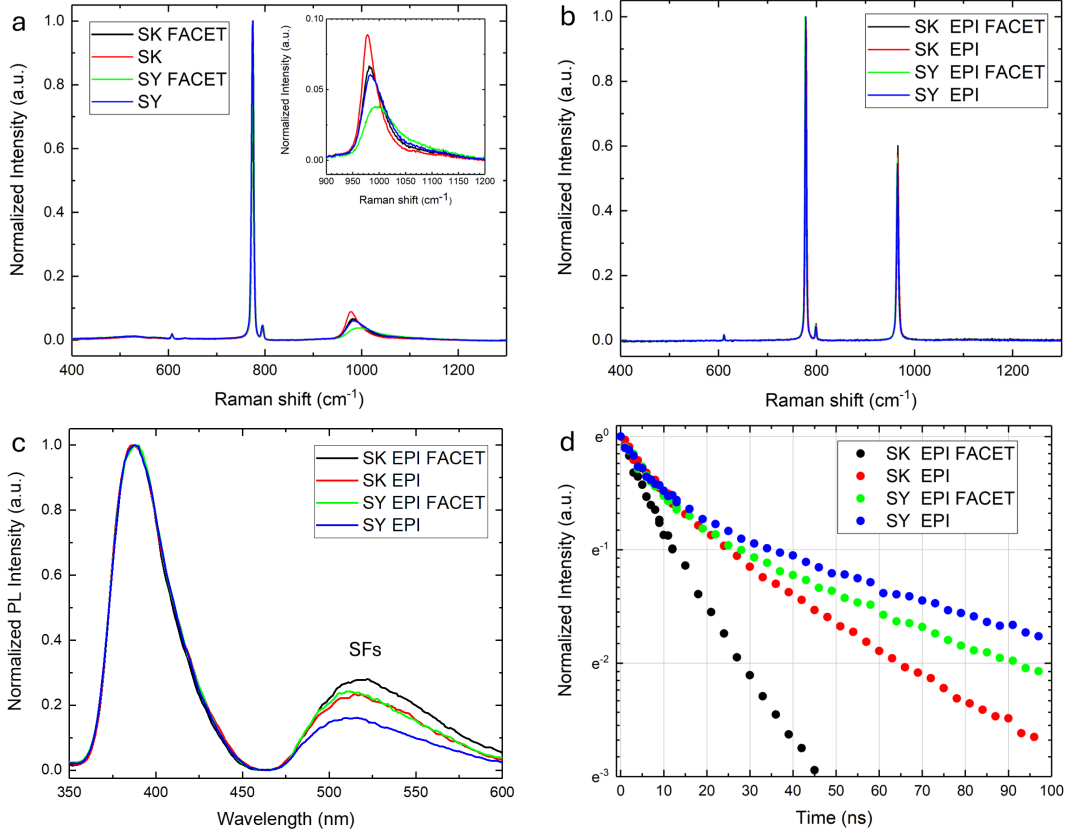
Figure 5.3: *a) Normalized micro-Raman spectra of wafer substrate. In the inset a detail of the LOPC band is reported. b) Normalized micro-Raman spectra of epitaxial wafer. c) Photoluminescence spectra with excitation wavelength of 325 nm of epitaxial wafer normalized to the intensity of the excitonic band at 390 nm. d) Normalized photoluminescence decay under excitation at 266 nm (4.66 eV) of excitonic band of the epitaxial wafers. Adapted from [145].*

facet included, is within the range of the expected concentration ($10^{16}cm^{-3}$). In the emission spectra (fig.5.3c), normalized to the intensity of the excitonic band (at about 390 nm), the intensity of the band attributed to SFs defects indicates that the amount of these defects is minimum for SY EPI, is similar for SY EPI facet and SK EPI and is maximum for SK EPI facet. Also the study of the time decay of the excitonic band (fig.5.3d) suggests that the amount of defects, connected to both the radiative and the non-radiative recombination of the exciton, has the same trend in the different samples suggested by the steady state emission spectra. As discussed in chapter 4, the lifetime of the excitonic recombination is not uniform along the epitaxial layer (fig.4.2d and fig.4.3d) because both the distribution of defects in the epilayer and the one of levels introduced by doping at the interface with the substrate are not uniform. In particular, for the irradiation experiments, samples with the following average lifetimes have been selected: SK EPI facet with $\tau = 12 \pm 3$ ns; SK EPI with $\tau = 25 \pm 3$ ns; SY EPI facet with $\tau = 28 \pm 3$ ns and SY EPI with $\tau = 35 \pm 3$ ns.
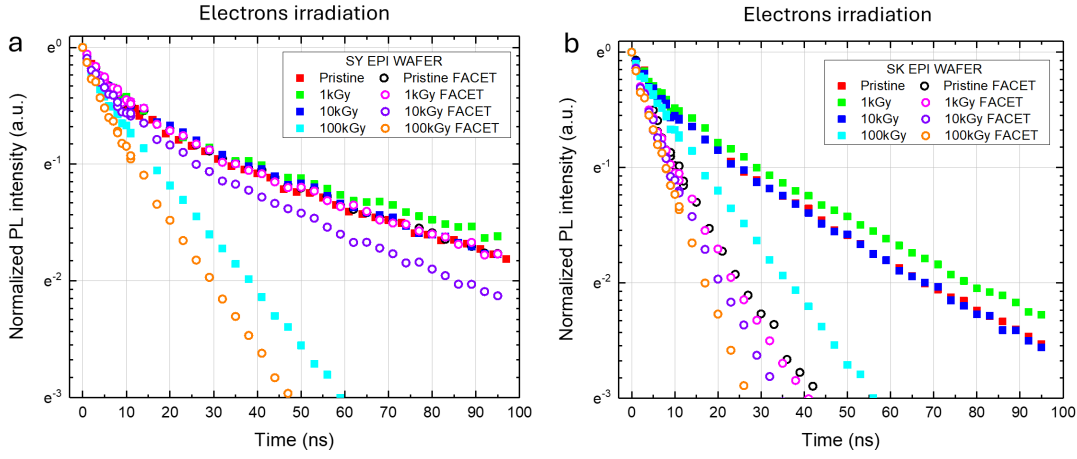
Figure 5.4: *a) Photoluminescence time decay under excitation with 266 nm wavelength (4.7 eV) of excitonic band of SY EPI (filled squares) and SY EPI facet (empty dots) after electron irradiation with different deposited doses. b) Photoluminescence time decay under excitation with 266 nm wavelength (4.7 eV) of excitonic band of SK EPI (filled squares) and SK EPI facet (empty dots) after electron irradiation with different deposited doses. Adapted from [145].*

5.2.1 Effects of Electron Irradiations

The selected samples have been exposed to electron irradiation and the doses 1 kGy, 10 kGy and 100 kGy have been accumulated on different samples. It is found that at the used doses the micro-Raman and the absorption spectra of all the electron irradiated samples are unchanged with respect to the not irradiated ones (data not shown).

In Fig.5.4a the study of the time decay of the excitonic band, before and after electron irradiation, of the SY EPI samples, represented by filled squares, and SY EPI facet samples, represented by empty dots, are reported. Analogously, in fig.5.4b the time decays of the excitonic band, before and after electron irradiation, on the samples SK EPI (filled squares) and SK EPI facet (empty dots) are shown. A clear decrease of the lifetime of the excitonic band in the sample SY EPI (20 ± 6 ns) and SK EPI (9 ± 6 ns) at the deposited dose of 100 kGy is visible. Instead, at the deposited dose of 10 kGy only in the SY EPI FACET a reduction of lifetime of 9 ± 6 ns is observed. With regard to SK EPI FACET samples, the ones with the highest amount of defects, the lifetime values remain as in pristine samples within the experimental error regardless of the deposited dose.

Since the lifetime of the excitonic band is influenced by both radiative and non-radiative decay processes, lifetime can be expressed as $\tau = 1/(k_r + k_{nr})$, where k_r is the radiative rate and k_{nr} is the non-radiative rate [93, 142]. Especially this latter is related to the presence of recombination centers [21]. The reduction of the lifetime of the excitonic band is ascribed to the formation of point defects which enhance the recombination rate of the excitons by non-radiative ways. The radiative recombination rate should remain unchanged because structural modifications of the crystalline structure
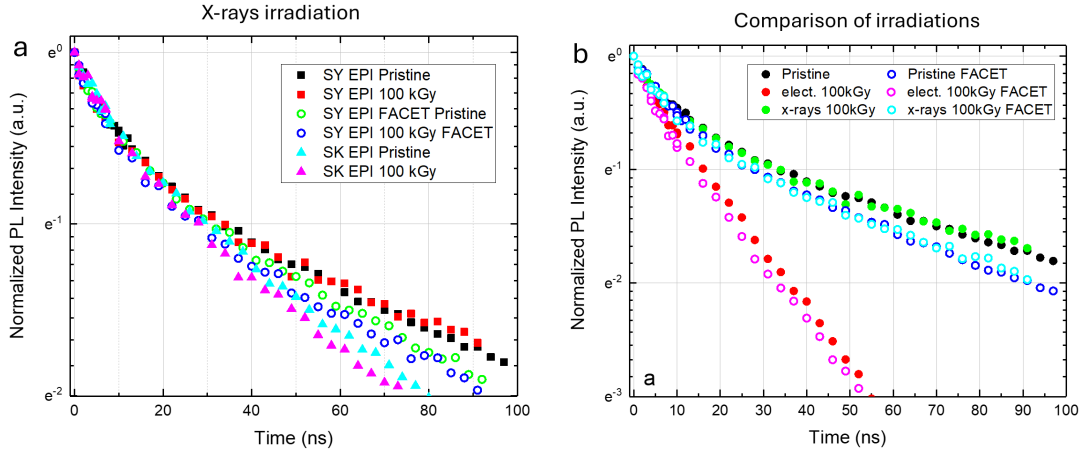
Figure 5.5: *a) Photoluminescence time decay under excitation with 266 nm wavelength (4.7 eV) of the excitonic band of SY EPI (filled squares), SY EPI facet (empty dots) and SK EPI (filled triangles) before and after x-rays irradiation at deposited dose of 100 kGy. b) Comparison of photoluminescence time decay under excitation with 266 nm wavelength (4.7 eV) of excitonic band of SY EPI (filled dots) and SY EPI facet (empty dots) samples with deposited dose of 100 kGy before and after electron and x-rays irradiation. Adapted from [145].*

have not been detected (at least by micro-Raman spectroscopy) in the explored dose range. Furthermore, the emission spectral characteristics, peak position and width, of the excitonic band of all the samples are the same for all the deposited doses and comparable to the pristine (not irradiated) samples (data not shown). This proves that the optical characteristics of 4H-SiC epitaxial layer remain unchanged. It is worth to note that the micro-Raman and absorption spectra of all the samples remain equal to the ones of the pristine samples after the electron irradiation probably because the new generated defects have too low concentration to be detected by these techniques.

5.2.2   Effects of x-rays

The characterizations conducted on the samples exposed to x-rays (from both sources) lead to similar observations of the electron irradiated samples. In particular, no differences in micro-Raman, absorption, and emission spectra before and after the exposure to x-rays were detected (spectra are not shown). The most interesting aspect is that, as depicted in fig.5.5a, even the lifetime of the excitonic band is not changed after the x-rays irradiation for all samples with the maximum deposited dose (100 kGy) (SK EPI, SY EPI, and SY EPI FACET).

To evidence the differences of the effects of x-rays and electron irradiation on the studied samples, the comparison of the decay curves of the excitonic band of the samples SY EPI (reported with filled dots) and SY EPI facet (indicated by empty dots) before and after the electron and x-rays irradiation with the maximum deposited dose (100 kGy) is reported in fig.5.5b. It is evident that x-rays do not induce any effects depositing
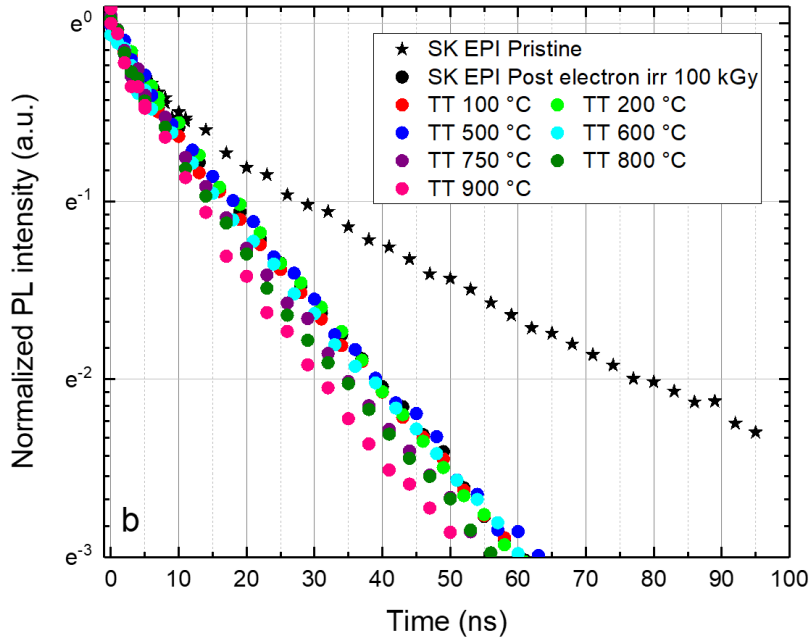
Figure 5.6: *Photoluminescence time decay under excitation with 266 nm wavelength (4.7 eV) of excitonic band of SK EPI sample with deposited dose of 100 kGy. Black stars refer to the pristine sample, black dots refers to the irradiated sample and the colored dots refer to the sample after thermal treatments at different temperatures [145].*

the same dose as electron irradiation.

Since the employed maximum dose 100 kGy is the same for electron and x-rays irridations it is guessed that the different response of the irradiated samples implies that the defects induced by electron beam belong to the group of defects of displacement damages [146, 147, 148]. Indeed, as discussed before, the electron beam is made of massive particles that have larger probability to affect C or Si atoms and displace them. In particular, the electrons used in this work have an energy of 2.5 MeV that is larger than the energy needed to displace both C and Si atoms from SiC lattice [146, 149]. By contrast the photons used in this study, having energy 28 keV and 100 keV, are not able to induce any relevant ionization effect in the explored dose range.

5.2.3 Study of the Recovery Properties of 4H-SiC

The sample SK EPI electron irradiated with the maximum deposited dose (100 kGy) has been thermally treated in air from 100 °C up to 900 °C with steps of 50 °C for 30 minutes. After each treatment, the decay time of the excitonic band has been studied to monitor the possible recovery of the lifetime meaning a reduction of the electron beam induced defects. Several studies reported that the most of defects induced by electrons are unstable and disappear or transform into other defects as a result of thermal annealing between 50-400 °C [137, 150]. The defects that survive after annealing at 900 °C are known as $Z_{1/2}$ and $EH_{6/7}$ and are related to carbon vacancies [150, 151, 152].

In fig.5.6 the study of the photoluminescence time decay of the excitonic band after

different thermal treatments at increasing temperature is reported. Also the data of the pristine SK EPI sample are reported for comparison. It is evident that the thermal treatments do not change the lifetime decay even at 900 °C suggesting that the defect induced by electron beam irradiation are related to stable carbon vacancies. A more specific identification is impossible with the methods used in this thesis.

5.3   Conclusions

In this chapter the study of 2.5 MeV electron and x-rays irradiation effects on epitaxial layers of 4H-SiC by non-invasive characterization techniques is reported. Among the utilized techniques, time-resolved photoluminescence spectroscopy is sensitive to the effects of electron irradiations that consist in the reduction of the lifetime of the excitonic recombination band. This effect is attributed to the generation of point defects that increase the exciton recombination rate by non-radiative ways. In particular, in the samples characterized by an higher amount of native defects, the reduction of lifetime is observed starting from smaller deposited dose (in agreement with the attribution of the exciton lifetime changes in epilayer due to different concentration of defects). On the x-rays irradiated samples with the same deposited dose as electron irradiated ones no effects have been detected. These observations lead to the attribution of the defects introduced by electron irradiation to defects generated by the displacement of atoms from their lattice positions (vacancies, interstitial, complex of them), known as displacement damages. Furthermore, the induced defects are stable after thermal treatments in air at 900 °C. This probably indicates that the defects generated by electron irradiation are related to stable carbon vacancies as the other kind of possible induced defects (by electron irradiation) "disappear" after annealing at lower temperature.

Chapter 6

Thermal Stability of 4H-SiC Substrates

As discuss in chapter 5, SiC is one of the most suitable wide bandgap semiconductor to realize devices which can operate at high power, high frequency and in harsh environments [70, 71, 72, 73, 132, 133, 134, 135]. In particular, in chapter 5 the focus was about the effect of ionizing radiation as electrons and x-rays on 4H-SiC epitaxial layer. Instead, in this chapter the effect of high temperature on bare substrates of 4H-SiC in inert atmosphere is explored. Studying this aspect is fundamental as the growth of epitaxial layer (the first step to manufacture a device) requires high temperature treatments [24, 98, 104]. Moreover, high-temperature environments, where SiC devices can be used, are common in several different applicative fields (space, automotive, industry, control system, etc...). Furthermore, it has been observed that treatments at temperature around 2000 °C in different atmospheres may induce the sublimation of Si from SiC lattice and then the growth of graphene layers on top of SiC [153, 154, 155]. This is a very interesting way to produce graphene but at the same time the potential vulnerability of SiC to thermal treatments (also in different conditions) is proved.

In this chapter, the thermal stability of 4H-SiC substrates in inert atmosphere in the temperature range 1600-2000 °C is discussed. In particular, the wafers surface quality has been checked by micro-Raman spectroscopy. In certain conditions, the thermal treatment induced the formation of surface defects that have been related to a graphitization process. However, the growth of a 4H-SiC epitaxial layer on top of these thermally treated defective substrates seems to be not affected so much in connection to the crystal structure of the epilayer. To further investigate the difference between epitaxial layer growth on damaged substrates (by thermal treatment) or on a high quality substrates, time-resolved photoluminescence spectroscopy measurements have been also conducted to highlight those differences related to the thermal process.
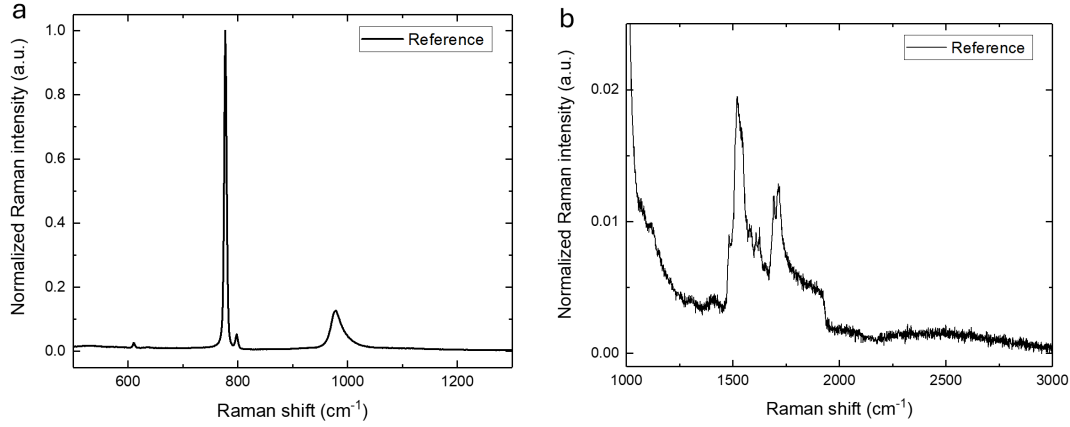
Figure 6.1: *a) Raman spectrum of the reference sample in the 500-1300 cm^{-1} range normalized with respect to the TO band at about 780 cm^{-1}. b) Normalized Raman spectrum with respect to the TO band of the reference sample in the 1000-3000 cm^{-1} range.*

6.1 Thermally Treated Substrates

The wafer substrate used for the study of the thermal stability is provided by STMicroelectronics but is from a different supplier (Cree) respect to all the others samples previously studied in this thesis. The first thermally treated 4H-SiC samples are two wafer substrates, named sample A and sample B hereafter, of 6-inch, 350 μm thickness and having the same doping. The only difference is in the extension of the facet that, as discussed in chapter 4, is characterized by higher doping compared to the rest of the wafer. In details, sample A has a circular facet of 9 cm of diameter at the center of the wafer while in sample B the facet is extended as the whole wafer surface. Both substrates have been treated with a thermal process at temperatures in the range 1600-2000 °C. The process involves a fast thermal ramp up to the treatment temperature (below 2000 °C), followed by a plateau of few seconds at the maximum temperature in Ar atmosphere and a spontaneous natural cooling of about 3 h.

In fig.6.1a is reported the micro-Raman spectrum, normalized with respect to the TO band, of a high quality 4H-SiC substrate (from the same supplier of samples A and B) that has not been thermally treated and that will be used as the reference sample. In particular, in fig.6.1b is shown the Raman spectrum of 4H-SiC in the 1000-3000 cm^{-1} range, where several peaks between 1500-1800 cm^{-1} are clearly visible. These bands are related to second-order Raman peaks from the SiC [156].

In fig.6.2a the micro-Raman spectra in the range of the LOPC band, the one related to doping, conducted along a diameter of sample A (that is thermally treated) are reported together with a graphical representation of the sample. It is evident that in correspondence with the facet (blue, green and red lines) the doping is higher with respect to the rest of the wafer. As discussed in chapter 4, this can be deduced by the higher Raman shift value and the broader width of the LOPC band of the spectra
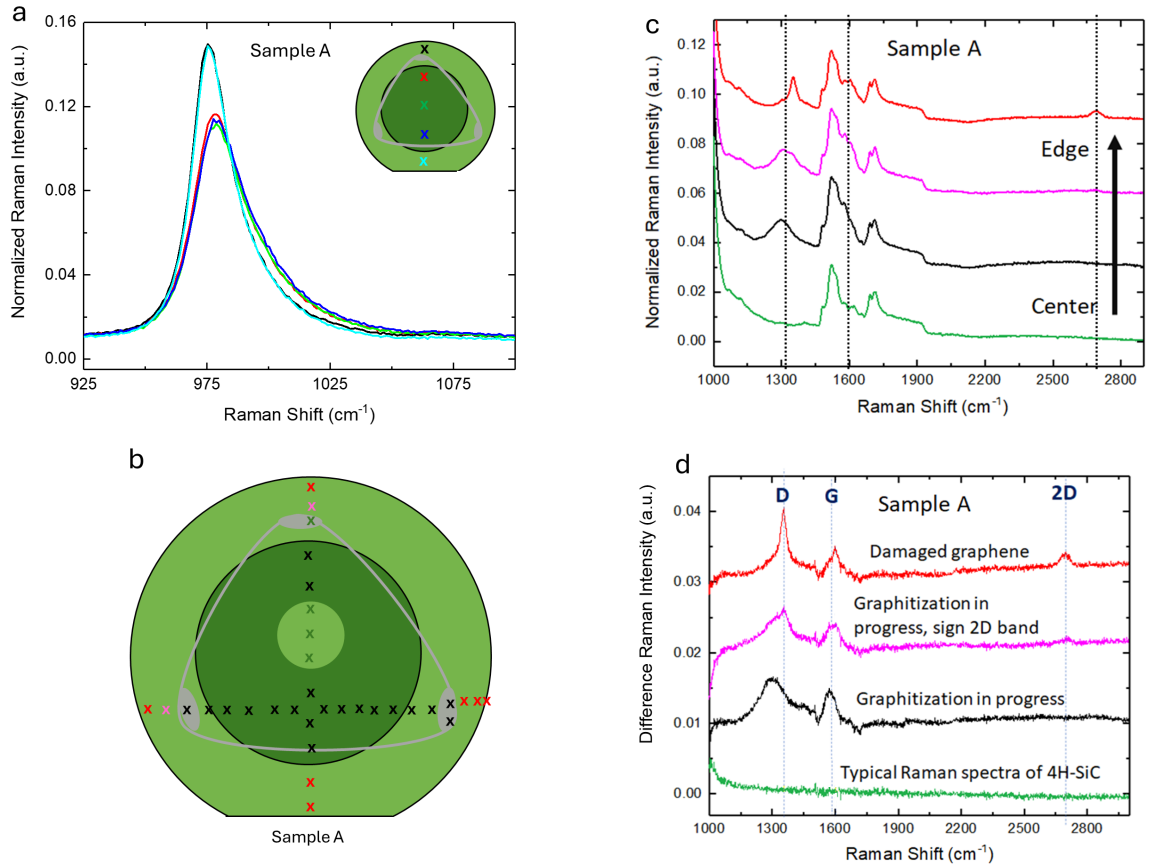
Figure 6.2: *a) Normalized Raman spectra with respect to the TO band of sample A along a diameter in the range of the LOPC band. It is also present a graphical representation of the substrate. The color of the spectra refer to the positions where they have been acquired that are marked by an x of the same color in the substrate representation. b) Graphical representation of sample A where by x are marked the positions where the Raman spectra reported in panel c) have been acquired. The colors of the x refer to the shape of the spectra reported in panel c in that point. c) Normalized Raman spectra (with respect to the TO band) of sample A in different positions after thermal treatment at 1650 °C. Dashed lines are guides for the eye to mark some reference spectral positions. d) Normalized Raman spectra of panel c) after the subtraction of the reference spectrum of 4H-SiC reported in fig.6.1. The dashed lines mark the spectral positions of the D, G and 2D Raman peaks of graphene.*
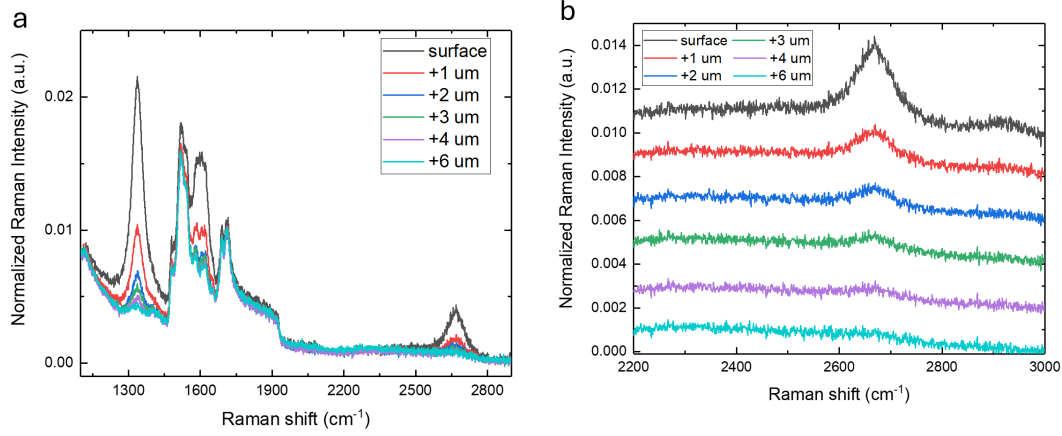
Figure 6.3: *a) Micro-Raman measurements normalized with respect to the TO band conducted on a spot of the edge of sample A at different z positions below the sample surface. b) Zoom in the 2200-3000 cm^{-1} range of the spectra in panel a). The spectra are arbitrarily vertically shifted for convenience.*

acquired on the facet [98, 109, 111, 157].

In fig.6.2b a map of the points where the Raman spectra were registered on sample A is depicted. The colors of the x refer to the shape of the spectrum, shown in fig.6.2c, in that point. In particular, in fig.6.2c the micro-Raman spectra (normalized with respect to the TO band) acquired in different radial positions, from the centre to the edges, of sample A after the thermal treatment performed at 1650 °C are reported. The colors of the spectra refer to a particular area of the wafer: green for a circular area of 3 cm of diameter centered at the center of the wafer, pink at 1-2 cm from the edges, red on the edges and black in the remaining parts of the surface. At first sight it is clear that the spectra are different implying that the surface of sample A is not homogeneous after the thermal treatment. In details, the spectra in the range 1000-3000 cm^{-1} are characterized by the typical bands of 4H-SiC together with specific shape changes and band positions (as evidenced by dashed lines) in fig.6.2c going from the centre to the edges of the wafer.

To evidence the effects of the thermal process, the spectra of fig.6.2c after the subtraction of the reference Raman spectrum of fig.6.1b are reported in fig.6.2d. Moreover, the typical spectral positions of the Raman bands D (~ 1350 cm^{-1}), G (~ 1580 cm^{-1}), and 2D (~ 2700 cm^{-1}) of graphene are indicated with dashed lines [158, 159]. The green spectrum, collected in the centre of the sample A, has no additional signal to that of 4H-SiC indicating that the corresponding part of the sample is made of high quality not modified 4H-SiC. In the black spectrum, that refers to the most widespread region of the sample, two bands around 1300 cm^{-1} and 1580 cm^{-1} are evident. At 1-2 cm from the edge, in the pink spectrum, it is possible to observe a shift of the bands toward high Raman shifts values. Furthermore, even if it is hardly visible, another band around 2700 cm^{-1} is present. In the red spectrum, in correspondence with the

edges, the band around 2700 cm^{-1} is clearly evident and the bands at 1350 cm^{-1} and 1600 cm^{-1} became narrower. A comparison with data reported in literature confirm that the red spectra match very well with the Raman spectra of low-quality or damaged graphene [153, 160, 161] whereas the other spectra resemble those of amorphous carbon [158, 160, 161]. Overall the observed features suggest that the thermal treatments have induced an inhomogeneous graphitization of the sample surface.

The z-profile (scan of the region below the sample's surface by Raman spectra) conducted in a spot of the edge of sample A (red spectrum in fig.6.2c) is reported in fig.6.3. It is found that moving beneath the surface of the sample the spectrum changes gradually and, finally, at a depth of 4 μm under the surface, the traces of graphitization completely disappear. Considering that the estimated vertical resolution of the micro-Raman setup is 2-3 μm, the effect induced by the thermal treatment is limited to the surface of the sample.

Similar considerations made for the experiment of sample A are valid for sample B. In fig.6.4a, the micro-Raman spectra in the range of the LOPC band of sample B are reported. As expected (the facet is extended as the whole wafer) the doping is quite homogeneous. It is worth to note that basing on the position and amplitude of the Raman LOPC band, the doping of sample B is the same as sample A in the facet area. In fig.6.4b a map of the positions where the Raman spectra on sample B were acquired, reported in fig.6.4c, is depicted (this time the color of the x is the same all over the sample). In particular, in fig.6.4c a micro-Raman spectrum (normalized with respect to the TO band) acquired on sample B after the thermal treatment performed at 1650 °C is reported. In this case, the effect of the treatment is homogeneous all over the wafer and, as found in sample A, this effect is visible in correspondence to the spectral range marked by the dashed lines. In fig.6.4d, to evidence the effects of thermal process, the recorded micro-Raman spectrum of fig.6.4c after the subtraction of the reference spectrum is reported. Also in this case two bands at 1300 cm^{-1} and 1580 cm^{-1} are clearly evident.

The comparison of the most widespread micro-Raman difference spectrum of sample A (in black) together with the one of sample B (in red) is reported in fig.6.5. The spectra have the same shape, furthermore the region of Sample A and Sample B compared in fig.6.5 have the same doping (facet area). For this reason it is possible to state that the effects observed is the same for both samples and that this effect seems to be related to the doping levels of the substrate.

The observed results can be explain as a graphitization process of the surface triggered by the desorption of Si from the SiC lattice. This mechanism is exploited to produce high quality graphene on 4H-SiC or in other polytypes with hexagonal symmetry working in inert atmosphere or in vacuum and starting from 1200 °C, depending on other parameters as gas pressure and growth time [80, 153, 154, 155, 158].
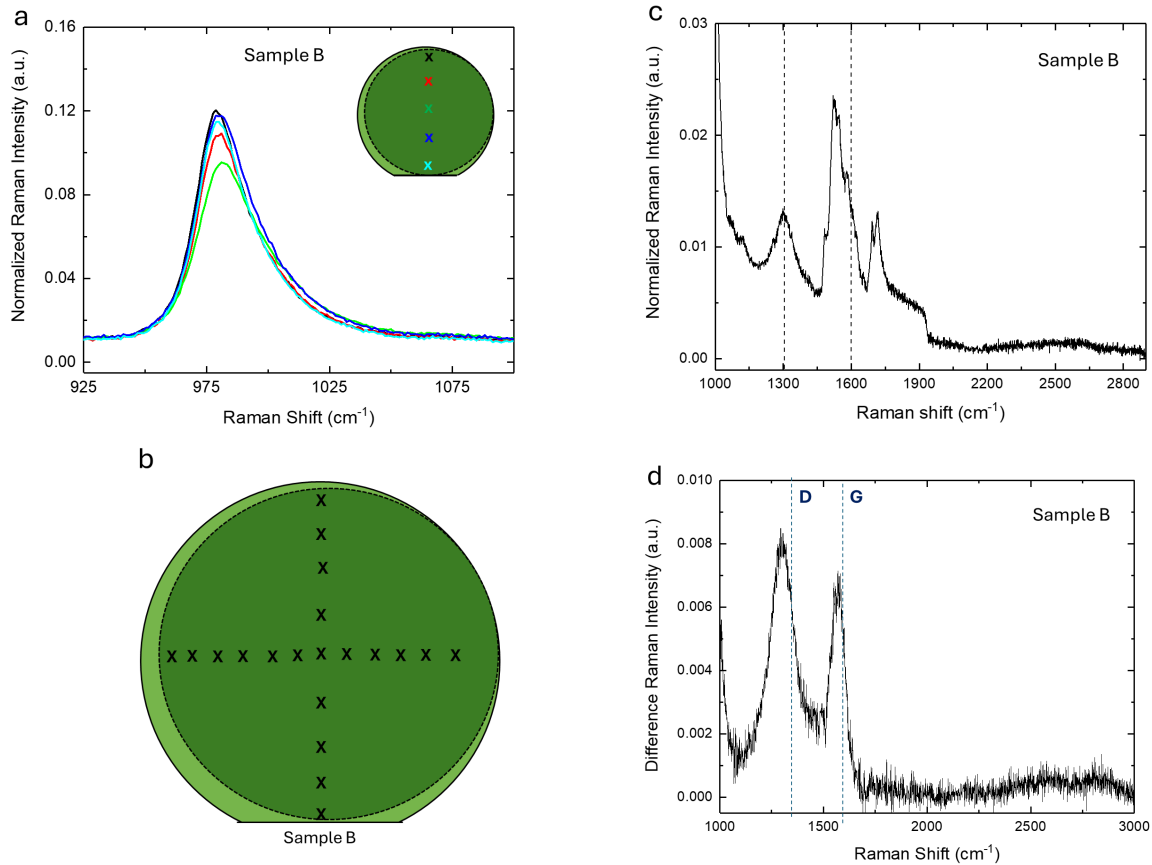
Figure 6.4: *a) Normalized Raman spectra with respect to the TO band of sample B along a diameter in the range of LOPC band. It is also present a graphical representation of the substrate. The color of the spectra refer to the positions where they have been acquired that are marked by an x of the same color in the substrate representation. b) Graphical representation of sample B, the x mark the positions where the Raman spectrum reported in panel c) was collected. c) Normalized Raman spectrum (with respect to the TO band) of sample B after thermal treatment at 1650 °C. d) Normalized Raman spectrum of fig.6.4c after the subtraction of the reference spectrum. The dashed lines D, G refer to the Raman peaks of graphene.*
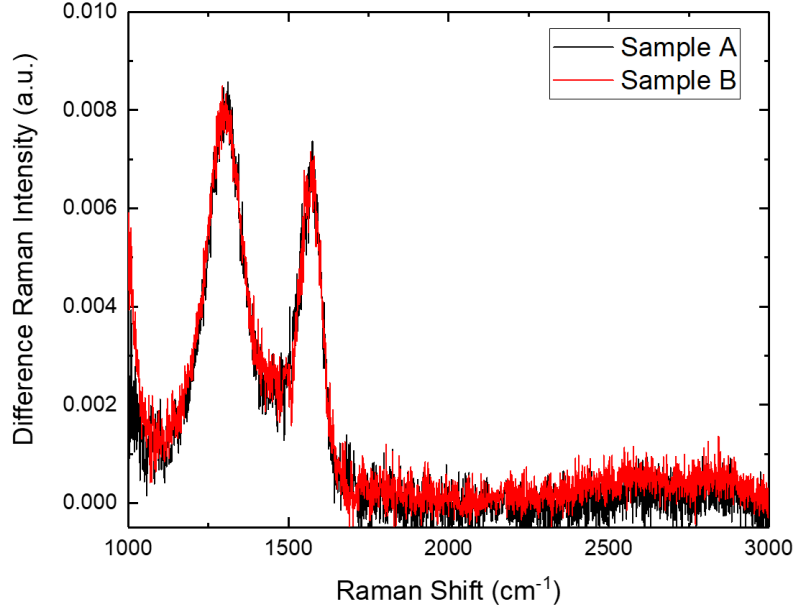
Figure 6.5: *Normalized Raman spectra (with respect to the TO band) of sample A (in black) and sample B (in red), after the subtraction of the reference spectrum of 4H-SiC, collected in wafer positions with same doping.*

6.2 Epitaxial Layer Grown on Thermally Treated Substrates

To study the impact of the graphitization effect of the thermally treated substrates on the epitaxial layer growth, an epitaxial layer of 12 μm thickness and n-type doping of 10^{16}cm^{-3} was grown on a substrate which presented the graphitization effects described in the previous section.

In fig.6.6a and fig.6.6b, the z-profile conducted on the epitaxial layer grown on the damaged substrate is reported. It is possible to notice that even at a depth of 12 μm below the surface, so at the interface between the epitaxial layer and the substrate, the effect of the graphitization in the micro-Raman spectra are not visible. To further investigate the effects of the graphitization of the substrate, time-resolved photoluminescence spectroscopy measurements have been conducted on the damaged substrate after the epitaxial layer growth. In particular, the normalized photoluminescence time decay of the excitonic band recorded in different wafer positions are reported in fig.6.6c. For comparison, in fig.6.6d, the same study conducted on an epitaxial layer grown with the same conditions on a high quality substrate is reported. The lifetime values are different, in particular they are 12 ± 2 ns in the epitaxial layer grown on the damaged substrate and 25 ± 2 ns in the epitaxial layer grown on a good substrate. This observation shows that, even if the graphitization of the substrate is not detectable by micro-Raman measurements, the defective graphitized "layer" clearly has an impact

69
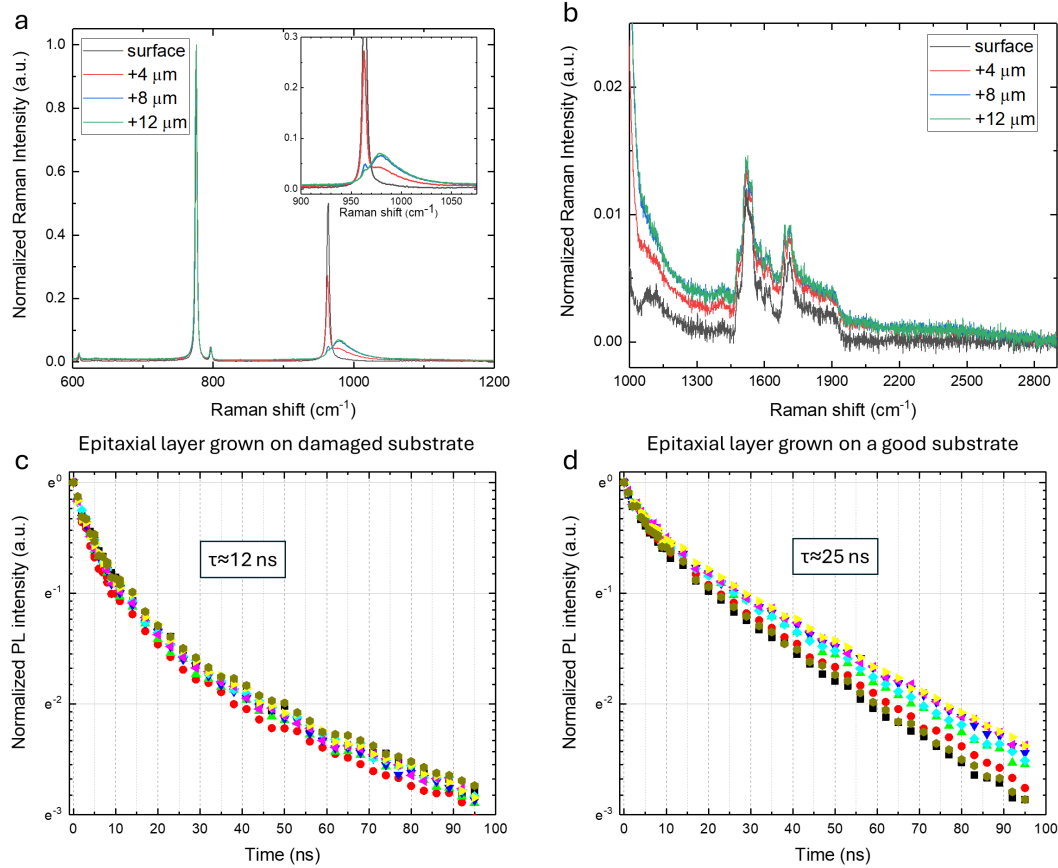
Figure 6.6: *a) Normalized micro-Raman spectra carried out on different z positions below the epitaxial layer surface grown on the damaged substrate; the inset reports a zoom of the LOPC band. b) Zoom in the 1000-2900 cm^{-1} range of spectra in panel a. c) Photoluminescence time decay under excitation with 266 nm wavelength (4.7 eV) of the excitonic band measured at different positions on the epitaxial layer grown on a damaged substrate. d) Photoluminescence time decay under excitation with 266 nm wavelength (4.7 eV) of the excitonic band measured at different positions on the epitaxial layer grown on an high quality substrate.*
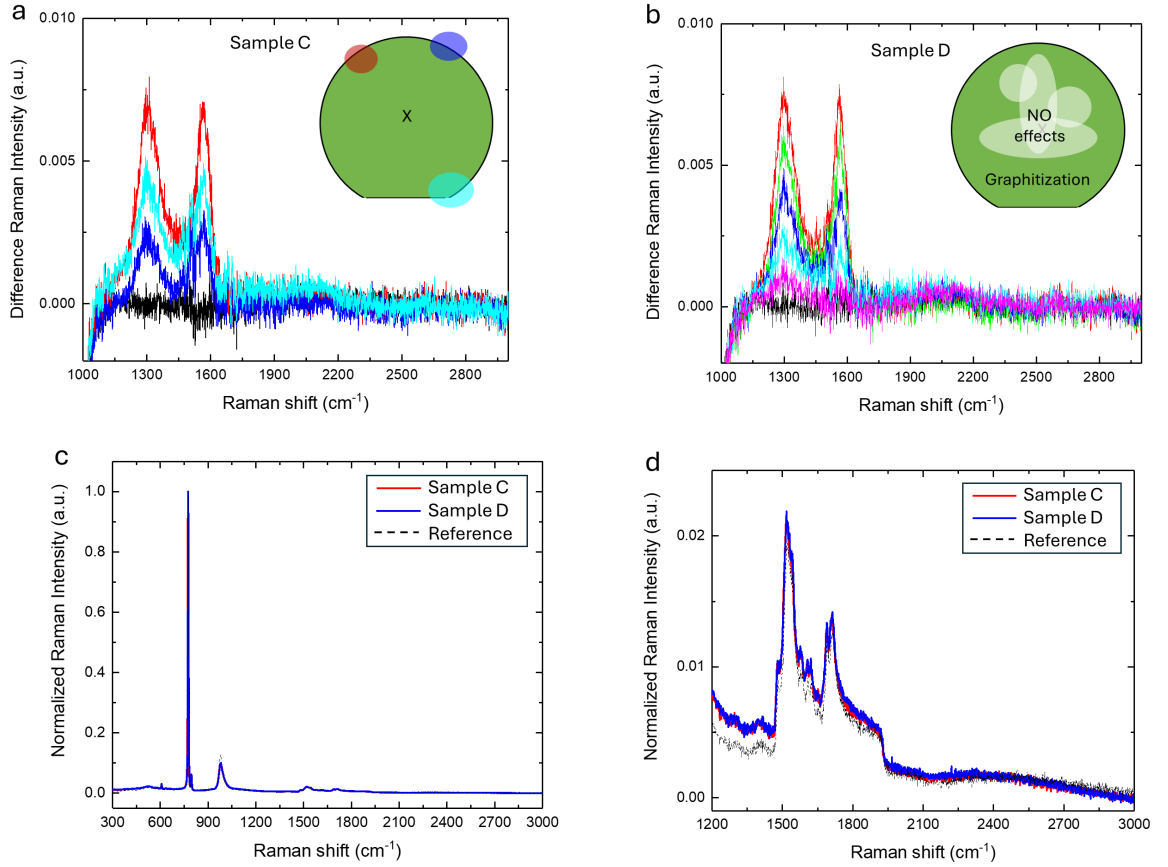
Figure 6.7: *a) Normalized micro-Raman spectra of sample C subtracted by the normalized reference spectrum; in the representation of the sample the areas of measurements are evidenced using the same color of the relative spectra. b) Normalized micro-Raman spectra of sample D subtracted by the normalized reference spectrum; in the representation of the sample the areas evidenced refer to the black line spectrum with no detected effect, the other areas give origin to the other reported sPectra. c) Normalized micro-Raman spectra of sample C and sample D after the etching. The reference micro-Raman spectrum is also reported. d) Zoom in the 1200-3000 cm^{-1} range of the spectra in panel c*

that, in particular, consists in the reduction of the lifetime of the exciton.

6.2.1 Etching

As discussed in the previous paragraph, even if the graphitization of the substrate is not detectable by micro-Raman measurements after the growth of the epitaxial layer, the defective "layer" influences the recombination of the exciton reducing its lifetime. Clearly this could affect the electrical performance of any device growth on an epitaxial layer obtained on a thermally treated substrate. For this reason it is important to understand if it is possible to remove the defectivity induced by the thermal treatment.

For this reason, two substrates, named sample C and sample D, have been thermally treated with the same process of sample A and B. In fig.6.7a and fig.6.7b the

normalized (with respect to the TO band) micro-Raman spectra after the subtraction of the reference spectrum, conducted on different parts of the samples C and sample D are reported together with a graphical representation of the sample. This time the graphitization effects of the thermal treatments are concentrated in the outer parts of both wafers.

To try to remove the graphitization, an etching in hydrogen of few minutes has been performed. The normalized micro-Raman spectra of sample C and sample D after the etching are shown in fig.6.7c and fig.6.7d. For comparison, the reference Raman spectrum is also reported. All the spectra have the same shape suggesting that the etching is able to remove the graphitization. It is worth to note that sampling of spectra has been carried out all over the surface of both samples.

To verify that no latent effects remain after removing the graphitization, should be interesting to grow an epitaxial layer on this substrate and study the decay time of the exciton band and compare the lifetime with the one of an epitaxial layer grown with the same features on a high quality substrate.

6.3 Conclusions

In this chapter, the thermal stability in inert atmosphere at temperatures in the range 1600-2000 °C of 4H-SiC substrates have been studied. Thanks to micro-Raman spectroscopy, it was possible to observe graphitization effects. In particular, amorphous carbon and traces of damaged graphene have been detected after the thermal process. Furthermore, a dependence of the graphitization effect on doping is observed. The graphitization of the substrate surface may be related to the desorption of Si from the SiC lattice. The properties of epitaxial layer grown on thermally treated substrates have been studied by micro-Raman and time-resolve photoluminescence spectroscopy. The graphitization of the substrate seems to not affect the crystal structure of the epitaxial layer grown on it but has an important influence in the recombination lifetime of the exciton, in particular shortening it. These findings evidence the potentialities of the spectroscopic techniques in evidencing electronic features of the material prior to complete the process of devices growth. Furthermore, by the combination of structural and dynamic investigation, as that carried out by time resolved photoluminescence, it is possible to somehow monitor the level of defectiveness and evaluate limits to be not overcome in view of the material application.

Chapter 7

Conclusions

In this thesis some interesting aspects about radiations and thermal resistance of 4H-SiC without any devices fabrication have been explored by using non-invasive characterization techniques. This choice enables to focus on the possible effects on the bare material, both substrates or epitaxial layers, avoiding the influence of the different steps needed to manufacture devices or the necessity to create metal contacts to perform electrical characterizations.

For these investigations, it is fundamental to identify non-invasive characterization techniques able to highlight differences among wafers and to disentangle features of the substrate from those of the epilayer. In particular, micro-Raman spectroscopy, steady state absorption, steady-state and time-resolved photoluminescence spectroscopy have been used to compare the properties of substrates and of the epilayers.

By micro-Raman measurements it has been possible to get information about the crystal structure and the doping of both substrates and epilayers. Furthermore, exploiting the z-resolution of the confocal microscope (of the micro-Raman set-up) it has been also possible to monitor the properties of substrates even after the growth of epitaxial layer on it. In particular, it has been shown that the substrate doping is not uniform along the same wafer (doping is higher on the facet region) and between wafers produced by different suppliers. Regarding the epitaxial layers, the doping is within the expected range on the whole epitaxial layers.

The comparison of the relative intensity of emission spectra (normalized to the intensity of the excitonic band) allowed to have qualitatively information about the amount of stacking faults defects in different wafers.

The monitoring of the time decay of the exciton recombination band by time-resolved photoluminescence spectroscopy turns out to be an interesting way to probe the uniformity and the quality of epitaxial layers. In particular, different lifetime values of the exciton recombination have been observed between epitaxial layers grown in the same way on substrates from different suppliers and also in the same wafer. In the former case, it has been shown that a shorter lifetime value is not directly associated

to higher doping. In the latter, it has been shown that the lifetime is shorter on the facet (where doping is higher) and, furthermore, that there is a distribution of lifetime values both in facet (having almost constant doping) and out of facet. These observations lead to the conclusion that a part of the recombination processes involve levels introduced by doping at the interface and that a part is related to the presence of point defects that are distributed not uniformly among the epitaxial layer and that enhance the exciton recombination by non-radiative ways. This finding is of large importance in the qualification of epitaxial layers in order to evaluate their electronic properties and processes before to continue in the growth of devices.

Even if these techniques give just qualitative information about doping, amount of stacking faults and (indirectly) point defects, these techniques can be used online, in the production line, to monitor these material properties during the different steps of a device growth, by comparison with a standard wafer. In particular may be very useful in the first step of the device production in which is fundamental to growth an epitaxial layer with certain thickness and doping on a degenerate doped substrate. The quality of substrates and epitaxial layers is fundamental as the features of SiC-based devices are influenced by the presence of extended defects, point defects and impurities (that can be introduced during each step of the growth).

Considering the peculiarities of SiC as the wide bandgap, the thermal conductivity, the chemical inertness, the mechanical strength and the large threshold energy for the defects formation (30-35 eV) it is clear that SiC-based devices are suitable for application in high-power and high-temperature electronics as well as for application in harsh environments (space electronics, nuclear power facilities, the management of nuclear waste, nuclear radiation detectors, UV photo-sensors, as well as X-ray and charged particle detectors). For this reason it is opportune to study the effects of the possible harsh environments starting from those produced on the bare material. For example, the presence of ionizing radiation can affect the structure, the transport properties and can lead to the formation of defects; exposure to high temperature can also stress, modify the structure and lead to the formation of defects, and it is possible to make the same observation for other factors as the presence of chemicals, wide-temperature range, mechanical vibrations, etc.., regarding the harsh environments.

In particular, in this thesis the effects of the exposure to 2.5 MeV electrons (depositing the doses 1, 10, and 100 kGy) and x-rays (depositing doses of 16 and 100 kGy) on epitaxial layer of 4H-SiC have been studied. Furthermore, also the resistance of 4H-SiC substrates to high temperature in inert atmosphere has been studied.

Among the non-invasive characterization techniques utilized, time-resolved photoluminescence spectroscopy is shown to be sensitive to the effects of electron irradiations. In details, the reduction of the lifetime of the excitonic recombination band has been observed in the electron irradiated samples. In correspondence of samples with higher presence of native defects (stacking faults, point defects and levels related to doping

at the interface between substrate and epitaxial layer), the reduction of the lifetime was observed starting from smaller deposited dose. The effect has been attributed to the generation of point defects that increase the exciton recombination rate by non-radiative ways. On the contrary, in x-rays irradiated samples, with the same deposited dose as electron, no effects have been detected. This difference between electron and x-rays irradiated samples leads to understand that the defects introduced by electron irradiation belong to the family of displacement damages which involved the physical displacement of atoms from their lattice positions generating vacancies, interstitial or complexes of these defects. Is a common experience that thermal treatments can induce a recovery (partial or total) of the properties of irradiated material, so thermal treatments in air up to 900 °C have been carried out. The effect of these treatments has been studied by monitoring the lifetime of the exciton recombination band and it has been found that the irradiation induced defects are stable up to 900 °C. This finding indicates (by comparison with literature data) that the induced defects are related to stable carbon vacancies as the other electron induced defects disappear after annealing at lower temperature.

To deepen the resistance of SiC to high temperature, the effects on substrates of high temperatures treatments during the growth of the epitaxial layer, the first step of a device growth, have been investigated. In particular, substrates of 4H-SiC have been thermally treated in inert atmosphere at temperature of 1650 °C. By micro-Raman spectroscopy the wafers surface quality has been checked. In particular, amorphous carbon and traces of damaged graphene have been detected in a layer of estimated $2\mu m$ thickness below the surface of the wafers. The effect of the thermal treatment is interpreted as a graphitization of the surface that in part is influenced by the doping. This process has been related to the desorption of Si from the SiC lattice, in fact this mechanism is reported in literature and is exploited (with different parameters) to produce high quality graphene and few layers graphene.

By micro-Raman and time-resolve photoluminescence spectroscopy, epitaxial layers grown on previously thermally treated substrates have been studied. The graphitization of the substrate seems to not affect the crystal structure of the epitaxial layer but has an important role in the recombination processes of the exciton. In fact the lifetime values in those epilayers are shorter with respect to the one in epitaxial layer grown on high quality substrates. Once again, time-resolved photoluminescence spectroscopy enables to highlight differences in epitaxial layer that in this specif case are related to the thermal process to which the substrate has been subjected.

The studies conducted in this thesis show the potentialities of the non-invasive spectroscopic techniques in characterizing the crystal structure, the doping, some of the extended defects as the stacking faults and indirectly the presence of point defects and also the electronic features of 4H-SiC prior to the device fabrication. For these reasons, these techniques can be used within the production line to check the discussed

properties during the first steps of the device manufacturing.

Further studies are needed to deeply identify the structural origin of the recombination centers responsible for the exciton decay modifications observed both for exposure to electron irradiation and for high temperature treatments. Apart from spectroscopic techniques, electrical characterizations can be also useful to get this result at least for a correlative aspect connected to charge carriers concentration and mobility estimation. Moreover, to deepen this aspect could be of interest in view of applications, in particular, for the optimization of the growth processes and devices performance.

Bibliography

[1] *Physical Properties of Silicon Carbide*, chapter 2, pages 11–38. John Wiley Sons, Ltd, 2014.

[2] U. Starke. *Atomic Structure of SiC Surfaces*, pages 281–316. Springer Berlin Heidelberg, Berlin, Heidelberg, 2004.

[3] Gary Lynn Harris. *Properties of silicon carbide.* Number 13. Iet, 1995.

[4] C. H. Park, Byoung-Ho Cheong, Keun-Ho Lee, and K. J. Chang. Structural and electronic properties of cubic, 2h, 4h, and 6h sic. *Phys. Rev. B*, 49:4485–4493, Feb 1994.

[5] W.Y. Ching, Yong-Nian Xu, Paul Rulis, and Lizhi Ouyang. The electronic structure and spectroscopic properties of 3c, 2h, 4h, 6h, 15r and 21r polymorphs of sic. *Materials Science and Engineering: A*, 422(1):147–156, 2006. NANOAM.

[6] G L Zhao and D Bagayoko. Electronic structure and charge transfer in 3c- and 4h-sic. *New Journal of Physics*, 2(1):16, jul 2000.

[7] C. Persson and U. Lindefelt. Relativistic band structure calculation of cubic and hexagonal SiC polytypes. *Journal of Applied Physics*, 82(11):5496–5508, 12 1997.

[8] S. G. Sridhara, R. P. Devaty, and W. J. Choyke. Absorption coefficient of 4H silicon carbide from 3900 to 3250 Å. *Journal of Applied Physics*, 84(5):2963–2964, 09 1998.

[9] W. J. Choyke and R. P. Devaty. *Optical Properties of SiC: 1997–2002*, pages 413–435. Springer Berlin Heidelberg, Berlin, Heidelberg, 2004.

[10] Ivan Pelant and Jan Valenta. Luminescence of excitons. In *Luminescence Spectroscopy of Semiconductors*. Oxford University Press, 02 2012.

[11] Kwan Chi Kao. 3 - optical and electro-optic processes. In Kwan Chi Kao, editor, *Dielectric Phenomena in Solids*, pages 115–212. Academic Press, San Diego, 2004.

[12] *Characterization Techniques and Defects in Silicon Carbide*, chapter 5, pages 125–187. John Wiley Sons, Ltd, 2014.

[13] J. Pernot, W. Zawadzki, S. Contreras, J. L. Robert, E. Neyret, and L. Di Cioccio. Electrical transport in n-type 4H silicon carbide. *Journal of Applied Physics*, 90(4):1869–1878, 08 2001.

[14] William J. Schaffer, Gerry Negley, Kenneth G. Irvine, and John W. Palmour. Conductivity anisotropy in epitaxial 6h and 4h sic. *MRS Proceedings*, 339:595, 1994.

[15] Dionysios Stefanakis, Xilun Chi, Takuya Maeda, Mitsuaki Kaneko, and Tsunenobu Kimoto. Experimental determination of impact ionization coefficients along ⟨1120⟩ in 4h-sic. *IEEE Transactions on Electron Devices*, 67(9):3740–3744, 2020.

[16] B Jayant Baliga. *Fundamentals of power semiconductor devices*. Springer Science & Business Media, 2010.

[17] D. Morelli, J. Heremans, C. Beetz, and W. S. Woo. Carrier concentration dependence of the thermal conductivity of silicon carbide. In *Silicon carbide and related materials, CONFERENCE SERIES- INSTITUTE OF PHYSICS*, volume 137, pages 313–315. Institute of Physics Publishing;, 1994.

[18] *Elastic Properties*, chapter 3, pages 41–72. John Wiley Sons, Ltd, 2005.

[19] H.-J. Rost, D. Schulz, and D. Siche. *High Nitrogen Doping During Bulk Growth of SiC*, pages 163–178. Springer Berlin Heidelberg, Berlin, Heidelberg, 2004.

[20] *Device Processing of Silicon Carbide*, chapter 6, pages 189–276. John Wiley Sons, Ltd, 2014.

[21] S.M. Sze and Kwok K. Ng. *Physics of Semiconductor Devices*. John Wiley Sons Inc, 2006.

[22] K Kamitani, M Grimsditch, JC Nipko, C-K Loong, M Okada, and I Kimura. The elastic constants of silicon carbide: A brillouin-scattering study of 4h and 6h sic single crystals. *Journal of applied physics*, 82(6):3152–3154, 1997.

[23] Eugene G Rochow. Gmelins handbuch der anorganischen chemie. achte völlig neu bearbeitete auflage. silicium. teil c. organische silicium-verbindungen. *Journal of the American Chemical Society*, 82(9):2405–2406, 1960.

[24] *Bulk Growth of Silicon Carbide*, chapter 3, pages 39–74. John Wiley Sons, Ltd, 2014.

[25] O. Kordina, C. Hallin, A. Ellison, A. S. Bakin, I. G. Ivanov, A. Henry, R. Yakimova, M. Touminen, A. Vehanen, and E. Janzén. High temperature chemical vapor deposition of SiC. *Applied Physics Letters*, 69(10):1456–1458, 09 1996.

[26] Masatoshi Kanaya, Jun Takahashi, Yuichiro Fujiwara, and Akihiro Moritani. Controlled sublimation growth of single crystalline 4H-SiC and 6H-SiC and identification of polytypes by x-ray diffraction. *Applied Physics Letters*, 58(1):56–58, 01 1991.

[27] *Epitaxial Growth of Silicon Carbide*, chapter 4, pages 75–124. John Wiley Sons, Ltd, 2014.

[28] Tsunenobu Kimoto. Bulk and epitaxial growth of silicon carbide. *Progress in Crystal Growth and Characterization of Materials*, 62(2):329–351, 2016. Special Issue: Recent Progress on Fundamentals and Applications of Crystal Growth; Proceedings of the 16th International Summer School on Crystal Growth (ISSCG-16).

[29] Chuan Feng Zhe. *Silicon Carbide Materials, Processing Devices , publisher = CRC Press*, chapter Epitaxial Growth of High-Quality Silicon Carbide: Fundamentals and Recent Progress. 2003.

[30] Peder Bergman, H. Lendenmann, Per Åke Nilsson, Ulf Lindefelt, and P. Skytt. Crystal defects as source of anomalous forward voltage increase of 4h-sic diodes. In *Silicon Carbide and Related Materials 2000*, volume 353 of *Materials Science Forum*, pages 299–302. Trans Tech Publications Ltd, 1 2001.

[31] Kinga Kościewicz, Wlodek Strupiński, Dominika Teklinska, Krystyna Mazur, Mateusz Tokarczyk, Grzegorz Kowalski, and Andrzej Roman Olszyna. Epitaxial growth on 4h-sic on-axis, 0.5°, 1.25°, 2°, 4°, 8° off-axis substrates – defects analysis and reduction. In *Silicon Carbide and Related Materials 2010*, volume 679 of *Materials Science Forum*, pages 95–98. Trans Tech Publications Ltd, 4 2011.

[32] S Mahajan. Defects in semiconductors and their effects on devices. *Acta materialia*, 48(1):137–149, 2000.

[33] Z. Luo, T. Chen, D. C. Sheridan, and J. D. Cressler. *4H-SiC Power-Switching Devices for Extreme-Environment Applications*, pages 375–409. Springer Berlin Heidelberg, Berlin, Heidelberg, 2004.

[34] Sokrates T. Pantelides. The role of extended defects in device degradation. *physica status solidi (a)*, 210(1):175–180, 2013.

[35] Marius Grundmann. *Physics of semiconductors*, volume 11. Springer, 2010.

[36] L Torpo, M Marlo, T E M Staab, and R M Nieminen. Comprehensive ab initio study of properties of monovacancies and antisites in 4h-sic. *Journal of Physics: Condensed Matter*, 13(28):6203, jun 2001.

[37] Osipov A.V. Kukushkin, S.A. Mechanism of formation of carbon–vacancy structures in silicon carbide during its growth by atomic substitution. *Phys. Solid State*, 60(9):1891–1896, 2018.

[38] F. Bechstedt, J. Furthmüller, U. Grossner, and C. Raffy. *Zero- and Two-Dimensional Native Defects*, pages 3–25. Springer Berlin Heidelberg, Berlin, Heidelberg, 2004.

[39] J. R. Weber, W. F. Koehl, J. B. Varley, A. Janotti, B. B. Buckley, C. G. Van de Walle, and D. D. Awschalom. Defects in SiC for quantum computing. *Journal of Applied Physics*, 109(10):102417, 05 2011.

[40] M. Bockstedte, A. Mattausch, and O. Pankratov. *Defect Migration and Annealing Mechanisms*, pages 27–55. Springer Berlin Heidelberg, Berlin, Heidelberg, 2004.

[41] T. Umeda, N. T. Son, J. Isoya, E. Janzén, T. Ohshima, N. Morishita, H. Itoh, A. Gali, and M. Bockstedte. Identification of the carbon antisite-vacancy pair in 4*h*-sic. *Phys. Rev. Lett.*, 96:145501, Apr 2006.

[42] N. T. Son, Mt. Wagner, C. G. Hemmingsson, L. Storasta, B. Magnusson, W. M. Chen, S. Greulich-Weber, J.-M. Spaeth, and E. Janzén. *Electronic Structure of Deep Defects in SiC*, pages 461–492. Springer Berlin Heidelberg, Berlin, Heidelberg, 2004.

[43] N. T. Son, P. Carlsson, J. ul Hassan, E. Janzén, T. Umeda, J. Isoya, A. Gali, M. Bockstedte, N. Morishita, T. Ohshima, and H. Itoh. Divacancy in 4h-sic. *Phys. Rev. Lett.*, 96:055501, Feb 2006.

[44] L. Torpo, T. E. M. Staab, and R. M. Nieminen. Divacancy in $3c-$ and $4h-SiC$: an extremely stable defect. *Phys. Rev. B*, 65:085202, Jan 2002.

[45] Koutarou Kawahara, Xuan Thang Trinh, Nguyen Tien Son, Erik Janzén, Jun Suda, and Tsunenobu Kimoto. Quantitative comparison between Z12 center and carbon vacancy in 4H-SiC. *Journal of Applied Physics*, 115(14):143705, 04 2014.

[46] T. Dalibor, G. Pensl, H. Matsunami, T. Kimoto, W. J. Choyke, A. Schöner, and N. Nordell. Deep defect centers in silicon carbide monitored with deep level transient spectroscopy. *physica status solidi (a)*, 162(1):199–225, 1997.

[47] C. Hemmingsson, N. T. Son, O. Kordina, J. P. Bergman, E. Janzén, J. L. Lindström, S. Savage, and N. Nordell. Deep level defects in electron-irradiated 4H SiC epitaxial layers. *Journal of Applied Physics*, 81(9):6155–6159, 05 1997.

[48] A. Zywietz, J. Furthmüller, and F. Bechstedt. Vacancies in sic: Influence of jahn-teller distortions, spin effects, and crystal structure. *Phys. Rev. B*, 59:15166–15180, Jun 1999.

[49] Michel Bockstedte, Alexander Mattausch, and Oleg Pankratov. Ab initio study of the annealing of vacancies and interstitials in cubic sic: Vacancy-interstitial recombination and aggregation of carbon interstitials. *Phys. Rev. B*, 69:235202, Jun 2004.

[50] Gan Feng, Jun Suda, and Tsunenobu Kimoto. Characterization of major in-grown stacking faults in 4h-sic epilayers. *Physica B: Condensed Matter*, 404(23):4745–4748, 2009.

[51] K Nakayama, T Hemmi, K Asano, T Miyazawa, and H Tsuchida. Observations of overlapped single shockley stacking faults in 4h-sic pin diode. *Acta Physica Polonica A*, 125(4):962–964, 2014.

[52] Matthew D. McCluskey and Anderson Janotti. Defects in Semiconductors. *Journal of Applied Physics*, 127(19):190401, 05 2020.

[53] S. Ha, P. Mieszkowski, M. Skowronski, and L.B. Rowland. Dislocation conversion in 4h silicon carbide epitaxy. *Journal of Crystal Growth*, 244(3):257–266, 2002.

[54] Noboru Ohtani, Masakazu Katsuno, Hiroshi Tsuge, Tatsuo Fujimoto, Masashi Nakabayashi, Hirokatsu Yashiro, Mitsuru Sawamura, Takashi Aigo, and Taizo Hoshino. Propagation behavior of threading dislocations during physical vapor transport growth of silicon carbide (sic) single crystals. *Journal of Crystal Growth*, 286(1):55–60, 2006.

[55] A. V. Samant M. H. Hong and P. Pirouz. Stacking fault energy of 6h-sic and 4h-sic single crystals. *Philosophical Magazine A*, 80(4):919–935, 2000.

[56] Song Bai, Günter Wagner, E. Shishkin, Wolfgang J. Choyke, Robert P. Devaty, M. Zhang, P. Pirouz, and Tsunenobu Kimoto. Spectra associated with stacking faults in 4h-sic grown in a hot-wall cvd reactor. In *Silicon Carbide and Related Materials 2001*, volume 389 of *Materials Science Forum*, pages 589–592. Trans Tech Publications Ltd, 4 2002.

[57] Gan Feng, Jun Suda, and Tsunenobu Kimoto. Characterization of stacking faults in 4h-sic epilayers by room-temperature microphotoluminescence mapping. *Applied Physics Letters*, 92(22), 2008.

[58] J. Hassan, A. Henry, I. G. Ivanov, and J. P. Bergman. In-grown stacking faults in 4H-SiC epilayers grown on off-cut substrates. *Journal of Applied Physics*, 105(12):123513, 06 2009.

[59] Daisuke Nakamura and Tsunenobu Kimoto. Transformation of hollow-core screw dislocations: transitional configuration of superscrew dislocations. *Japanese Journal of Applied Physics*, 59(9):095502, aug 2020.

[60] Junji Senzaki, Shohei Hayashi, Yoshiyuki Yonezawa, and Hajime Okumura. Challenges to realize highly reliable sic power devices: From the current status and issues of sic wafers. In *2018 IEEE International Reliability Physics Symposium (IRPS)*, pages 3B.3–1–3B.3–6, 2018.

[61] Hidekazu Tsuchida, Masahiko Ito, Isaho Kamata, and Masahiro Nagano. Formation of extended defects in 4h-sic epitaxial growth and development of a fast growth technique. *physica status solidi (b)*, 246(7):1553–1568, 2009.

[62] R. E. Stahbush and N. A. Mahadik. Defects affecting sic power device reliability. In *2018 IEEE International Reliability Physics Symposium (IRPS)*, pages 2B.4–1–2B.4–4, 2018.

[63] Muhammad Shakir, Shuoben Hou, Raheleh Hedayati, Bengt Gunnar Malm, Mikael Östling, and Carl-Mikael Zetterling. Towards silicon carbide vlsi circuits for extreme environment applications. *Electronics*, 8(5), 2019.

[64] Philip G Neudeck, David J Spry, Liangyu Chen, Norman F Prokop, and Michael J Krasowski. Demonstration of 4h-sic digital integrated circuits above 800° c. *IEEE Electron Device Letters*, 38(8):1082–1085, 2017.

[65] Philip G Neudeck, David J Spry, Liangyu Chen, Norman F Prokop, and Michael J Krasowski. Demonstration of 4h-sic digital integrated circuits above 800° c. *IEEE Electron Device Letters*, 38(8):1082–1085, 2017.

[66] Carl-Mikael Zetterling, Anders Hallén, Raheleh Hedayati, Saleh Kargarrazi, Luigia Lanni, B Gunnar Malm, Shabnam Mardani, Hans Norström, Ana Rusu, Sethu Saveda Suvanam, et al. Bipolar integrated circuits in sic for extreme environment operation. *Semiconductor Science and Technology*, 32(3):034002, 2017.

[67] C. M. Zetterling M. Östling L. Lanni, B. G. Malm. A 4h-sic bipolar technology for high-temperature integrated circuits. *Journal of Microelectronics and Electronic Packaging*, 2013.

[68] Juergen Biela, Mario Schweizer, Stefan Waffler, and Johann W. Kolar. Sic versus si—evaluation of potentials for performance improvement of inverter and dc–dc converter systems by sic power semiconductors. *IEEE Transactions on Industrial Electronics*, 58(7):2872–2882, 2011.

[69] Shinji Sato, Kohei Matsui, Yusuke Zushi, Yoshinori Murakami, and Satoshi Tanimoto. Development of high power density three-phase inverter. 2013.

[70] Sandeep K. Chaudhuri, Kelvin J. Zavalla, and Krishna C. Mandal. High resolution alpha particle detection using 4h–sic epitaxial layers: Fabrication, charac-

terization, and noise analysis. *Nuclear Instruments and Methods in Physics Research Section A: Accelerators, Spectrometers, Detectors and Associated Equipment*, 728:97–101, 2013.

[71] Francesco Moscatelli. Silicon carbide for uv, alpha, beta and x-ray detectors: Results and perspectives. *Nuclear Instruments and Methods in Physics Research Section A: Accelerators, Spectrometers, Detectors and Associated Equipment*, 583(1):157–161, 2007.

[72] Krishna C. Mandal, Peter G. Muzykov, and J. Russell Terry. Highly sensitive x-ray detectors in the low-energy range on n-type 4h-sic epitaxial layers. *Applied Physics Letters*, 101(5):051111, 2012.

[73] Tudisco S., F. La Via, Agodi C., and al. Sicilia—silicon carbide detectors for intense luminosity investigations and applications. *Sensors*, 18(7), 2018.

[74] Carmen Altana, Lucia Calcagno, Caterina Ciampi, Francesco La Via, Gaetano Lanzalone, Annamaria Muoio, Gabriele Pasquali, Domenico Pellegrino, Sebastiana Puglia, Giuseppe Rapisarda, and Salvatore Tudisco. Radiation damage by heavy ions in silicon and silicon carbide detectors. *Sensors*, 23(14), 2023.

[75] C. Ciampi, G. Pasquali, C. Altana, M. Bini, M. Boscardin, L. Calcagno, G. Casini, G.A.P. Cirrone, A. Fazzi, D. Giove, G. Gorini, L. Labate, F. La Via, G. Lanzalone, G. Litrico, A. Muoio, P. Ottanelli, G. Poggi, S.M.R. Puglia, M. Rebai, S. Ronchin, A. Santangelo, A.A. Stefanini, A. Trifirò, S. Tudisco, and M. Zimbone. Nuclear fragment identification with e-e telescopes exploiting silicon carbide detectors. *Nuclear Instruments and Methods in Physics Research Section A: Accelerators, Spectrometers, Detectors and Associated Equipment*, 925:60–69, 2019.

[76] M. Cutroneo, P. Musumeci, M. Zimbone, L. Torrisi, F. La Via, D. Margarone, A. Velyhan, J. Ullschmied, and L. Calcagno. High performance sic detectors for mev ion beams generated by intense pulsed laser plasmas. *Journal of Materials Research*, 2013.

[77] Mohammad Beygi, John T. Bentley, Christopher L. Frewin, Cary A. Kuliasha, Arash Takshi, Evans K. Bernardin, Francesco La Via, and Stephen E. Saddow. Fabrication of a monolithic implantable neural interface from cubic silicon carbide. *Micromachines*, 10(7), 2019.

[78] Xingbao Huang and Xiao Zhang. Investigating the advanced characteristics of sic based piezoresistive pressure sensors. *Materials Today Communications*, 25:101493, 2020.

[79] G. Wieczorek, B. Schellin, E. Obermeier, G. Fagnani, and L. Drera. Sic based pressure sensor for high-temperature environments. In *SENSORS, 2007 IEEE*, pages 748–751, 2007.

[80] Neeraj Mishra, John Boeckl, Nunzio Motta, and Francesca Iacopi. Graphene growth on silicon carbide: A review. *physica status solidi (a)*, 213(9):2277–2289, 2016.

[81] Filippo Giannazzo, Salvatore Ethan Panasci, Emanuela Schilirò, Antal Koos, and Béla Pécz. Integration of graphene and mos2 on silicon carbide: Materials science challenges and novel devices. *Materials Science in Semiconductor Processing*, 174:108220, 2024.

[82] II Lee, Edwin W., Lu Ma, Digbijoy N. Nath, Choong Hee Lee, Aaron Arehart, Yiying Wu, and Siddharth Rajan. Growth and electrical characterization of two-dimensional layered MoS2/SiC heterojunctions. *Applied Physics Letters*, 105(20):203504, 11 2014.

[83] Yifan Xiao, Long Min, Xinke Liu, Wenjun Liu, Usman Younis, Tonghua Peng, Xuanwu Kang, Xiaohan Wu, Shijin Ding, and David Wei Zhang. Facile integration of mos2/sic photodetector by direct chemical vapor deposition. *Nanophotonics*, 9(9):3035–3044, 2020.

[84] Pierre Gibart. Metal organic vapour phase epitaxy of gan and lateral overgrowth. *Reports on Progress in Physics*, 67(5):667, 2004.

[85] S. Majety, J. Li, W. P. Zhao, B. Huang, S. H. Wei, J. Y. Lin, and H. X. Jiang. Hexagonal boron nitride and 6H-SiC heterostructures. *Applied Physics Letters*, 102(21):213505, 05 2013.

[86] Galeckas A. Müting J. Ayedh H. M. Grossner U. Coutinho J. Frodason Y. K. Vines L. Bathen, M. E. Electrical charge state identification and control for the silicon vacancy in 4h-sic. *npj Quantum Information*, 2019.

[87] Alexander P. Demchenko. Excitonic properties of organic dye aggregates: Contribution of ukrainian science. *The Chemical Record*, 24(2):e202300290, 2024.

[88] C. Kittel. *Introduction to Solid State Physics, 7th edition*. John Wiley Sons, Inc., 1996.

[89] *The Optical Transparency of Solids*, chapter 4, pages 113–149. John Wiley Sons, Ltd, 2005.

[90] John R. Ferraro, Kazuo Nakamoto, and Chris W. Brown. Chapter 1 - basic theory. In John R. Ferraro, Kazuo Nakamoto, and Chris W. Brown, editors,

Introductory Raman Spectroscopy (Second Edition), pages 1–94. Academic Press, San Diego, second edition edition, 2003.

[91] D. A. Long. *The Raman Effect*. Wiley, first edition edition, 2002.

[92] S. Legnaioli B. Campanella, V. Palleschi. Introduction to vibrational spectroscopies. *ChemTexts 7*, 7, 2021.

[93] Joseph R. Lakowicz. *Principles of Fluorescence Spectroscopy*. Springer New York, NY, 2007.

[94] *Characteristics of Fluorescence Emission*, chapter 3, pages 34–71. John Wiley Sons, Ltd, 2001.

[95] *An Introduction to the Optical Spectroscopy of Inorganic Solids*, chapter 1, pages 1–38. John Wiley Sons, Ltd, 2005.

[96] https://ufd.kaust.edu.sa/detail/facilities/time-resolved-photoluminescence-spectroscopy available online.

[97] Angelo Armano. *Charge Transfer Processes Between Graphene and Small Moleculesor Carbon Nanoparticles*. PhD thesis, Università degli studi di Catania, Università degli studi di Palermo, 2019.

[98] J. C. Burton, L. Sun, M. Pophristic, S. J. Lukacs, F. H. Long, Z. C. Feng, and I. T. Ferguson. Spatial characterization of doped SiC wafers by Raman spectroscopy. *Journal of Applied Physics*, 84(11):6268–6273, 12 1998.

[99] A.A. Lebedev, Vitalii V. Kozlovski, Nikita B. Strokan, D.V. Davydov, Alexander M. Ivanov, Anatoly M. Strel'chuk, and Rositza Yakimova. Radiation hardness of silicon carbide. In *Silicon Carbide and Related Materials - 2002*, volume 433 of *Materials Science Forum*, pages 957–960. Trans Tech Publications Ltd, 7 2003.

[100] A. Le Donne, S. Binetti, and S. Pizzini. Electrical and optical characterization of electron-irradiated 4h-sic epitaxial layers annealed at low temperature. *Diamond and Related Materials*, 14(3):1150–1153, 2005. Proceedings of Diamond 2004, the 15th European Conference on Diamond, Diamond-Like Materials, Carbon Nanotubes, Nitrides and Silicon Carbide.

[101] Indudhar Panduranga Vali, Pramoda Kumara Shetty, M.G. Mahesha, V.G. Sathe, D.M. Phase, and R.J. Choudhary. Structural and optical studies of gamma irradiated n-doped 4h-sic. *Nuclear Instruments and Methods in Physics Research Section B: Beam Interactions with Materials and Atoms*, 440:101–106, 2019.

[102] Pavel Hazdra, Vít Záhlava, Jan Vobecký, Maxime Berthou, and Andrei Mihaila. Radiation defects produced in 4h-sic epilayers by proton and alpha-particle irradiation. In *Silicon Carbide and Related Materials 2012*, volume 740 of *Materials Science Forum*, pages 661–664. Trans Tech Publications Ltd, 3 2013.

[103] Antonio Castaldini, Anna Cavallini, Lorenzo Rigutti, Filippo Nava, Sergio Ferrero, and Fabrizio Giorgis. Deep levels by proton and electron irradiation in 4h–sic. *Journal of Applied Physics*, 98(5):053706, 2005.

[104] N. Ohtani, M. Katsuno, T. Fujimoto, and H. Yashiro. *Defect Formation and Reduction During Bulk SiC Growth*, pages 137–162. Springer Berlin Heidelberg, Berlin, Heidelberg, 2004.

[105] Fabrizio Roccaforte, Salvatore Di Franco, Filippo Giannazzo, Francesco La Via, Sebania Libertino, Vito Raineri, Mario Saggio, and Edoardo Zanetti. Silicon carbide: Defects and devices. In *Gettering and Defect Engineering in Semiconductor Technology XI*, volume 108 of *Solid State Phenomena*, pages 663–670. Trans Tech Publications Ltd, 10 2005.

[106] Lixia Zhao and Huiwang Wu. A correlation study of substrate and epitaxial wafer with 4h-n type silicon carbide. *Journal of Crystal Growth*, 507:109–112, 2019.

[107] Yingxin Cui, Juntao Li, Kun Zhou, Xinhe Zhang, and Guosheng Sun. Influence of extended defects and oval shaped facet on the minority carrier lifetime distribution in as-grown 4h-sic epilayers. *Diamond and Related Materials*, 92:25–31, 2019.

[108] Francesca Migliore, Marco Cannas, Franco Mario Gelardi, Daniele Vecchio, Andrea Brischetto, and Simonpietro Agnello. Defects in epitaxial 4h-sic revealed by exciton recombination. *Journal of Physics: Condensed Matter*, 36(18):185601, feb 2024.

[109] S. Nakashima, T. Kitamura, T. Mitani, H. Okumura, M. Katsuno, and N. Ohtani. Raman scattering study of carrier-transport and phonon properties of $4h-$SiC crystals with graded doping. *Phys. Rev. B*, 76:245208, Dec 2007.

[110] Hiroshi Harima, Shin-ichi Nakashima, and Tomoki Uemura. Raman scattering from anisotropic LO-phonon–plasmon–coupled mode in n-type 4H– and 6H–SiC. *Journal of Applied Physics*, 78(3):1996–2005, 08 1995.

[111] S. Nakashima, T. Kitamura, T. Kato, K. Kojima, R. Kosugi, H. Okumura, H. Tsuchida, and M. Ito. Determination of free carrier density in the low doping regime of 4H-SiC by Raman scattering. *Applied Physics Letters*, 93(12):121913, 09 2008.

[112] Stefan Zollner, J. G. Chen, Erika Duda, T. Wetteroth, S. R. Wilson, and James N. Hilfiker. Dielectric functions of bulk 4H and 6H SiC and spectroscopic ellipsometry studies of thin SiC films on Si. *Journal of Applied Physics*, 85(12):8353–8361, 06 1999.

[113] S.G. Sridhara, Song Bai, O. Shigiltchoff, Robert P. Devaty, and Wolfgang J. Choyke. Absorption bands associated with conduction bands and impurity states in 4h and 6h sic. In *Silicon Carbide and Related Materials - 1999*, volume 338 of *Materials Science Forum*, pages 551–554. Trans Tech Publications Ltd, 5 2000.

[114] P Ščajev and K Jarašiūnas. Application of a time-resolved four-wave mixing technique for the determination of thermal properties of 4h–sic crystals. *Journal of Physics D: Applied Physics*, 42(5):055413, feb 2009.

[115] Tsunenobu Kimoto, Satoshi Nakazawa, Koichi Hashimoto, and Hiroyuki Matsunami. Reduction of doping and trap concentrations in 4H–SiC epitaxial layers grown by chemical vapor deposition. *Applied Physics Letters*, 79(17):2761–2763, 10 2001.

[116] I. G. Ivanov, C. Hallin, A. Henry, O. Kordina, and E. Janzén. Nitrogen doping concentration as determined by photoluminescence in 4H– and 6H–SiC. *Journal of Applied Physics*, 80(6):3504–3508, 09 1996.

[117] Gan Feng, Jun Suda, and Tsunenobu Kimoto. Triple Shockley type stacking faults in 4H-SiC epilayers. *Applied Physics Letters*, 94(9):091910, 03 2009.

[118] H. Jung C. Oh D. Jang S. Hong M. Na, W. Bahng. Revisiting stacking fault identification based on the characteristic photoluminescence emission wavelengths of silicon carbide epitaxial wafers. *Materials Science in Semiconductor Processing*, 175:108247, 2024.

[119] T. Naijo K. Momose H. Osawa J. Senzaki K. Kojima T. Kato H. Okumura T. Yamashita, S. Hayashi. Characterization of stacking faults with emission wavelengths of over 500nm formed in 4h-sic epitaxial films. *Journal of Crystal Growth*, 476:99–106, 2017.

[120] Fabrizio Messina, Eleonora Vella, Marco Cannas, and Roberto Boscaino. Evidence of delocalized excitons in amorphous solids. *Phys. Rev. Lett.*, 105:116401, Sep 2010.

[121] Eleonora Vella, Fabrizio Messina, Marco Cannas, and Roberto Boscaino. Unraveling exciton dynamics in amorphous silicon dioxide: Interpretation of the optical features from 8 to 11 ev. *Phys. Rev. B*, 83:174201, May 2011.

[122] Y. Toyozawa. Dynamics and instabilities of an exciton in the phonon field and the correlated absorption-emission spectra. *Pure and Applied Chemistry*, 69(6):1171–1178, 1997.

[123] Jan Beyer, Nadine Schüler, Jürgen Erlekampf, Birgit Kallinger, Patrick Berwian, Kay Dornich, and Johannes Heitmann. Minority carrier lifetime measurements on 4h-sic epiwafers by time-resolved photoluminescence and microwave detected photoconductivity. In *Silicon Carbide and Related Materials 2018*, volume 963 of *Materials Science Forum*, pages 313–317. Trans Tech Publications Ltd, 9 2019.

[124] Takeshi Tawara, Hidekazu Tsuchida, Syunsuke Izumi, Isaho Kamata, and Kunikaza Izumi. Evaluation of free carrier lifetime and deep levels of the thick 4h-sic epilayers. In *Silicon Carbide and Related Materials 2003*, volume 457 of *Materials Science Forum*, pages 565–568. Trans Tech Publications Ltd, 6 2004.

[125] L. Palkuti, J. Prince, and A. Glista. Integrated circuit characteristics at 260°c for aircraft engine-control applications. *IEEE Transactions on Components, Hybrids, and Manufacturing Technology*, 2(4):405–412, 1979.

[126] F.S. Shoucair. Scaling, subthreshold, and leakage current matching characteristics in high-temperature (25 degrees c-250 degrees c) vlsi cmos devices. *IEEE Transactions on Components, Hybrids, and Manufacturing Technology*, 12(4):780–788, 1989.

[127] M. Citterio, J. Kierstead, S. Rescia, and V. Radeka. Radiation effects on si-jfet devices for front-end electronics. *IEEE Transactions on Nuclear Science*, 43(3):1576–1584, 1996.

[128] S. McClure, R.L. Pease, W. Will, and G. Perry. Dependence of total dose response of bipolar linear microcircuits on applied dose rate. *IEEE Transactions on Nuclear Science*, 41(6):2544–2549, 1994.

[129] M.R. Werner and W.R. Fahrner. Review on materials, microsensors, systems and devices for high-temperature and harsh-environment applications. *IEEE Transactions on Industrial Electronics*, 48(2):249–257, 2001.

[130] Artur Litvinov, Maya Etrekova, Boris Podlepetsky, Nikolay Samotaev, Konstantin Oblov, Alexey Afanasyev, and Vladimir Ilyin. Mosfe-capacitor silicon carbide-based hydrogen gas sensors. *Sensors*, 23(7), 2023.

[131] A. Lebedev, E. Kalinina, and V. Kozlovski. Radiation resistance of devices based on sic. *Journal of Surface Investigation: X-ray, Synchrotron and Neutron Techniques*, 12:364–369, 03 2018.

[132] Evgenia Kalinina. The effect of irradiation on the properties of sic and devices based on this compound. *Semiconductors*, 41:745–783, 07 2007.

[133] A Le Donne, S Binetti, M Acciarri, and S Pizzini. Electrical characterization of electron irradiated x-rays detectors based on 4h-sic epitaxial layers. *Diamond and Related Materials*, 13(3):414–418, 2004.

[134] Evgenia V. Kalinina, Alexander A. Lebedev, Vitalii V. Kozlovski, Vladimir Zabrodski, Anatoly M. Strel'chuk, and Irina P. Nikitina. Electrophysical and optical properties of 4h-sic uv detectors irradiated with electrons. In *Silicon Carbide and Related Materials 2018*, volume 963 of *Materials Science Forum*, pages 722–725. Trans Tech Publications Ltd, 9 2019.

[135] F Nava, G Bertuccio, A Cavallini, and E Vittone. Silicon carbide and its use as a radiation detector material. *Measurement Science and Technology*, 19(10):102001, aug 2008.

[136] Pavel Hazdra and Stanislav Popelka. Displacement damage and total ionisation dose effects on 4h-sic power devices. *IET Power Electronics*, 12(15):3910–3918, 2019.

[137] Pavel Hazdra and Jan Vobecký. Radiation defects created in n-type 4h-sic by electron irradiation in the energy range of 1–10 mev. *physica status solidi (a)*, 216(17):1900312, 2019.

[138] Joan Marc Rafí, Giulio Pellegrini, Philippe Godignon, Sofía Otero Ugobono, Gemma Rius, Isao Tsunoda, Masashi Yoneoka, Kenichiro Takakura, Gregor Kramberger, and Michael Moll. Electron, neutron, and proton irradiation effects on sic radiation detectors. *IEEE Transactions on Nuclear Science*, 67(12):2481–2489, 2020.

[139] Stanislav Popelka and Pavel Hazdra. Effect of electron irradiation on 1700v 4h-sic mosfet characteristics. In *Silicon Carbide and Related Materials 2015*, volume 858 of *Materials Science Forum*, pages 856–859. Trans Tech Publications Ltd, 6 2016.

[140] Jan Vobecký, Pavel Hazdra, Stanislav Popelka, and Rupendra Kumar Sharma. Impact of electron irradiation on the on-state characteristics of a 4h–sic jbs diode. *IEEE Transactions on Electron Devices*, 62(6):1964–1969, 2015.

[141] A.A. Lebedev, V.V. Kozlovski, M.E. Levinshtein, A.E. Ivanov, A.M. Strel'chuk, A.V. Zubov, and Leonid Fursin. Impact of 0.9 mev electron irradiation on main properties of high voltage vertical power 4h-sic mosfets. *Radiation Physics and Chemistry*, 177:109200, 2020.

[142] Simonpietro Agnello. *Spectroscopy for Materials Characterization*. John Wiley Sons Inc, 2021.

[143] J R Srour. Basic mechanisms of radiation effects on electronic materials, devices, and integrated circuits. technical report.

[144] R. A. B. Devine, J-P. Duraud, and Eric Dooryhee. Structure and imperfections in amorphous and crystalline silicon dioxide. 2000.

[145] F. Migliore, A. Alessi, F. Principato, S. Girard, M. Cannas, F. M. Gelardi, A. Lombardo, D. Vecchio, A. Brischetto, and S. Agnello. -rays induced displacement damage on epitaxial 4H-SiC revealed by exciton recombination. *Applied Physics Letters*, 124(4):042101, 01 2024.

[146] L. Storasta, J. P. Bergman, E. Janzén, A. Henry, and J. Lu. Deep levels created by low energy electron irradiation in 4h-sic. *Journal of Applied Physics*, 96(9):4909–4915, 2004.

[147] J.R. Srour, C.J. Marshall, and P.W. Marshall. Review of displacement damage effects in silicon devices. *IEEE Transactions on Nuclear Science*, 50(3):653–670, 2003.

[148] J. R. Srour and J. W. Palko. Displacement damage effects in irradiated semiconductor devices. *IEEE Transactions on Nuclear Science*, 60(3):1740–1766, 2013.

[149] J.W Steeds, G.A Evans, L.R Danks, S Furkert, W Voegeli, M.M Ismail, and F Carosella. Transmission electron microscope radiation damage of 4h and 6h sic studied by photoluminescence spectroscopy. *Diamond and Related Materials*, 11(12):1923–1945, 2002.

[150] Sergey A. Reshanov, Svetlana Beljakowa, Bernd Zippelius, Gerhard Pensl, Katsunori Danno, Giovanni Alfieri, Tsunenobu Kimoto, Shinobu Onoda, Takeshi Ohshima, Fei Yan, Robert P. Devaty, and Wolfgang J. Choyke. Thermal stability of defect centers in n- and p-type 4h-sic epilayers generated by irradiation with high-energy electrons. In *Silicon Carbide and Related Materials 2009*, volume 645 of *Materials Science Forum*, pages 423–426. Trans Tech Publications Ltd, 7 2010.

[151] Katsunori Danno and Tsunenobu Kimoto. Investigation of deep levels in n-type 4h-sic epilayers irradiated with low-energy electrons. *Journal of Applied Physics*, 100(11):113728, 2006.

[152] G. Alfieri, E. V. Monakhov, B. G. Svensson, and M. K. Linnarsson. Annealing behavior between room temperature and 2000°C of deep level defects in electron-

irradiated n-type 4H silicon carbide. *Journal of Applied Physics*, 98(4):043518, 08 2005.

[153] K.V. Emtsev, A. Bostwick, K. Horn, J. Jobst, G. L. Kellogg, L. Ley, J. L. McChesney, T. Ohta, S. A. Reshanov, J. Röhrl, E. Rotenberg, A. K. Schmid, D. Waldmann, H. B. Weber, and T. Seyller. Towards wafer-size graphene layers by atmospheric pressure graphitization of silicon carbide. *NATURE MATERIALs*, 8, 2009.

[154] W. A. de Heer J. Hass and E. H. Conrad. The growth and morphology of epitaxial multilayer graphene. *J. Phys.: Condens. Matter*, 20, 2008.

[155] J. L. Tedesco, G. G. Jernigan, J. C. Culbertson, J. K. Hite, Y. Yang, K. M. Daniels, R. L. Myers-Ward, C. R. Eddy, J. A. Robinson, K. A. Trumbull, M. T. Wetherington, P. M. Campbell, and D. K. Gaskill. Morphology characterization of argon-mediated epitaxial graphene on c-face sic. *Applied Physics Letters*, 96(22), May 2010. Funding Information: The authors acknowledge the Office of Naval Research and Defense Advanced Research Projects Agency Carbon Electronics for RF Applications program for funding. J.L.T. and J.K.H. acknowledge the American Society for Engineering Education for support through Naval Research Laboratory Postdoctoral Fellowships. Y.Y. and K.M.D. acknowledge support from the Naval Research Enterprise Intern Program.

[156] J. C. Burton, L. Sun, F. H. Long, Z. C. Feng, and I. T. Ferguson. First- and second-order raman scattering from semi-insulating $4h - \mathrm{SiC}$. *Phys. Rev. B*, 59:7282–7284, Mar 1999.

[157] S. Nakashima and H. Harima. Raman investigation of sic polytypes. *physica status solidi (a)*, 162(1):39–64, 1997.

[158] V. Zolyomi, J. Koltai, and J. Kurti. Resonance raman spectroscopy of graphite and graphene. *Phys. Status Solidi B*, 248(11):2435–2444, 2011.

[159] P. Klar, E. Lidorikis, A. Eckmann, I. A. Verzhbitskiy, A. C. Ferrari, and C. Casiraghi. Raman scattering efficiency of graphene. *Phys. Rev. B*, 87:205435, May 2013.

[160] D. Rouchon, L. Becerra, O. Renault, K. Kaja, D. Mariolle, and N. Chevalier. Raman spectra and imaging of graphene layers grown by sic sublimation. *AIP Conf. Proc.*, 1267:445–446, 2010.

[161] Clément Faugeras, Anouck Nerrière, Marek Potemski, Ather Mahmood, Erik Dujardin, Claire Berger, and W. Heer. Few-layer graphene on sic, pyrolitic graphene: a raman scattering study. appl phys lett 92:011914-1-011914-3. *Applied Physics Letters*, 92, 09 2007.